Physics Reports 1201 (2026) 1–56

Contents lists available at ScienceDirect

Physics Reports

journal homepage: www.elsevier.com/locate/physrep

Review article

Light confinement and frequency combs in nonlinear photonics☆,☆☆

Mustapha Tlidi [a,*], Marcel G. Clerc [b], Stefano Boccaletti [c,d,e,f]

[a] Université Libre de Bruxelles (U.L.B), CP 231, Campus Plaine, 1050 Bruxelles, Belgium
[b] Departamento de Fisica and Millennium Institute for Research in Optics. Universidad de Chile, Casilla 487-3, Santiago, Chile
[c] Sino-Europe Complexity Science Center, North University of China, Taiyuan 030051, China
[d] International Research Center of Complexity Sciences, Hangzhou International Innovation Institute, Beihang University, Hangzhou 311115, China
[e] Research Institute of Interdisciplinary Intelligent Science, Ningbo University of Technology, 315104 Ningbo, China
[f] Institute of Complex Systems, National Research Council, Sesto Fiorentino 50019, Italy

ARTICLE INFO

Article history:
Received 6 March 2026
Accepted 8 July 2026

Editor: Itamar Procaccia

Keywords:
Dissipative solitons
Nonlinear optical resonators
Optical frequency comb generation
Optical pattern formation
Spectral filtering
Raman frequency combs
Delayed feedback control
Spatiotemporal chaos

ABSTRACT

The advent of high-quality optical microresonators and integrated photonic technologies has established Kerr frequency combs as a versatile platform for both fundamental studies and practical applications in modern photonics. These combs arise from the interplay between optical nonlinearity, dispersion, coherent driving, and cavity dissipation, leading to the emergence of a rich variety of self-organized structures and nonlinear dynamical states. This review presents a comprehensive overview of dissipative solitons and frequency-comb generation in passive Kerr resonators within the framework of the Lugiato–Lefever equation and its various extensions. We show how the Lugiato–Lefever model provides a unified theoretical description of nonlinear phenomena ranging from modulation instability, Turing patterns, and front propagation to dissipative Kerr solitons, multi-soliton states, and optical frequency-comb formation. Particular attention is devoted to the fundamental mechanisms governing light confinement, nonlinear wave localization, and soliton stabilization in driven-dissipative optical cavities. We further examine the influence of additional physical effects that enrich the dynamics of Kerr resonators, including polarization coupling and vector dissipative solitons, Raman scattering and Raman–Kerr comb generation, spectral filtering, spatially inhomogeneous pumping, and delayed optical feedback.

Beyond stationary dissipative Kerr solitons, commonly known as dissipative Kerr solitons, passive optical resonators support a wide spectrum of dynamical behaviors, including breathing and drifting solitons, oscillatory localized states, front-mediated dynamics, and fully developed spatiotemporal chaos. Particular attention is devoted to the characterization of these complex regimes through the tools of nonlinear dynamics and dynamical systems theory. In this context, Lyapunov spectra and the Kaplan–Yorke dimension provide powerful indicators for identifying chaotic attractors, quantifying the dimensionality of the dynamics, and distinguishing spatiotemporal chaos from other forms of irregular behavior. Their application reveals the coexistence of chaotic states with dissipative Kerr solitons and homogeneous steady solutions, emphasizing the intricate organization of the phase space of driven-dissipative optical systems. These findings illustrate the deep connections between pattern formation, self-organization, front propagation, symmetry breaking, and high-dimensional nonlinear dynamics in

☆ This article is part of a Special issue entitled: 'Light confinement and frequency combs' published in Physics Reports.

☆☆ This document is the results of the research project funded by the National Science Foundation.

* Corresponding author.
E-mail address: mtlidi@ulb.ac.be (M. Tlidi).

https://doi.org/10.1016/j.physrep.2026.07.005

Kerr resonators. This review offers a unified framework for understanding the physical mechanisms governing Kerr frequency-comb generation and control. The rapid progress achieved in material platforms, microresonator design, and photonic integration continues to expand the accessible dynamical regimes and performance of frequency-comb sources. As a result, Kerr comb technologies are becoming increasingly important for a broad range of applications, including precision metrology, spectroscopy, coherent optical communications, microwave photonics, sensing, and emerging quantum information and quantum sensing technologies.

Contents

1. Introduction ... 2
2. Periodic and dissipative Kerr solitons ... 4
2.1. Retrospective view ... 4
2.2. Bridging the driven-damped Sine–Gordon and Lugiato–Lefever equations ... 5
3. Theoretical description of passive optical resonators ... 7
3.1. Reduction of the Maxwell–Bloch equations to the Lugiato–Lefever equation ... 7
3.2. Modeling passive optical resonators with the Ikeda map ... 7
3.3. Continuous-wave solutions, bistability, and pattern-forming instabilities ... 9
3.4. Periodic patterns and dissipative Kerr solitons in passive optical cavities ... 10
3.5. Homoclinic snaking and dissipative soliton interactions ... 12
3.6. Toward the formation of light bullets in optical resonators ... 14
4. Front dynamics and dissipative solitons in the Lugiato–Lefever equation under inhomogeneous pumping ... 15
4.1. Dissipative soliton formation under inhomogeneous pumping ... 15
4.2. Periodic and dissipative Kerr solitons under inhomogeneous injection ... 16
4.3. Formation and propagation of switching fronts in optical bistability ... 17
4.4. Experimental observation of front dynamics in a Kerr cavity with negative diffraction ... 19
4.5. Propagation fronts in passive cavities with synchronization mismatch ... 20
5. Delayed feedback control of dissipative soliton dynamics ... 23
5.1. Applications of time-delayed feedback ... 23
5.2. The Swift–Hohenberg equation with delayed feedback ... 23
5.3. Passive optical cavities with delayed feedback ... 25
6. Polarization dynamics of vector dissipative solitons ... 28
6.1. Polarization dynamics in the coupled Lugiato–Lefever equation ... 28
6.2. Coexisting vector dissipative soliton families with different polarization states and peak powers ... 30
6.3. Vector soliton families and domain walls ... 31
7. Spectral filtering effects on Kerr frequency combs ... 33
7.1. Spectral filtering in nonlinear Kerr resonators ... 33
7.2. Lugiato–Lefever model with spectral filtering ... 34
7.3. Drifting and breathing dissipative soliton combs ... 35
8. Raman-Kerr frequency combs in microresonators ... 39
8.1. Raman Kerr frequency combs in optical resonators ... 39
8.2. Mean-field equation with spectral filtering ... 40
8.3. Propagation of Kerr domain walls in the normal dispersion regime ... 40
9. Complex spatiotemporal behavior in passive resonators ... 45
9.1. Spatiotemporal chaos and turbulence-like behaviors ... 45
9.2. Spatiotemporal chaos ... 46
10. Conclusions and perspectives ... 48
CRediT authorship contribution statement ... 48
Declaration of competing interest ... 49
Acknowledgments ... 49
References ... 49

1. Introduction

Nonlinear photonics has emerged as a central field of modern optical science, enabling phenomena arising when the polarization response of a medium depends on the intensity of the electromagnetic field. Fundamental nonlinear interactions such as second-harmonic generation (SHG), four-wave mixing (FWM), and self-phase modulation (SPM) play key roles in ultrafast signal processing, frequency conversion, and coherent optical communications [1,2]. Historically, these effects required high-power lasers or long propagation distances in bulk materials. The advent of micro- and

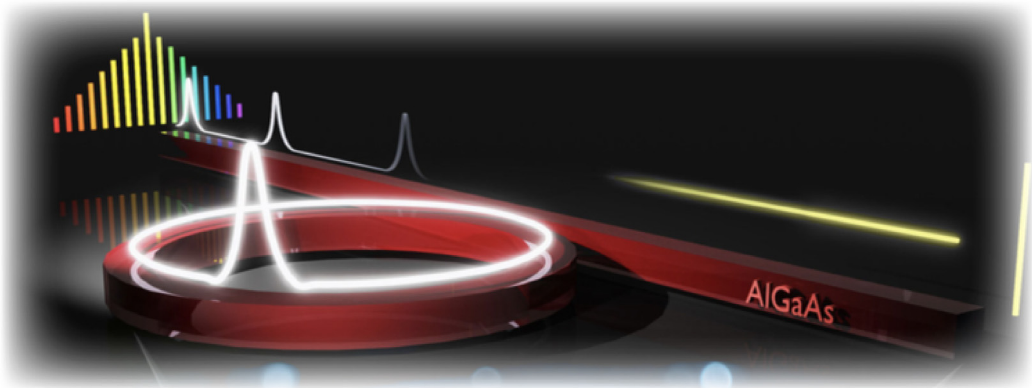

Fig. 1. Stabilization of an optical frequency comb. The repetition rate and offset frequency are measured and locked to a stable reference using feedback control, ensuring the comb remains accurate for precision applications.

nanophotonic platforms has radically changed this paradigm: strong spatial confinement dramatically enhances nonlinear interactions, making them accessible with pump powers as low as milliwatts or even microwatts.

Light confinement within engineered photonic structures, such as high-Q microresonators, photonic crystal cavities, and dispersion-engineered waveguides, extends the interaction time between light and matter while significantly increasing optical intensity [3]. Whispering gallery mode (WGM) resonators and silicon-nitride integrated waveguides, in particular, have proven highly effective in achieving low threshold powers and enabling a wide range of nonlinear effects [4,5]. These platforms have created ideal conditions for exploring rich dynamical regimes, including modulation instability, parametric oscillation, and dissipative structures. One of the most transformative outcomes of nonlinear photonics and light confinement is the development of optical frequency combs, spectral arrays of evenly spaced lines that serve as precise rulers in the frequency domain. Frequency combs have revolutionized spectroscopy, metrology, optical clocks, and high-precision measurement science. Initially generated through mode-locked lasers [6,7], frequency combs can now be produced in chip scale microresonators via Kerr nonlinearities [8]. These Kerr frequency combs, or microcombs, rely on cascaded FWM in high-Q resonators pumped by a continuous-wave laser. Their compactness, compatibility, broad spectra, and high degree of coherence offer unique advantages for integrated photonics [9].

A key physical mechanism underlying many microcombs is the formation of dissipative Kerr solitons (DKS). When a CW laser pumps a microresonator exhibiting anomalous group velocity dispersion, the balance between dispersion, Kerr nonlinearity, pump detuning, and cavity loss supports stable circulating pulses. These temporal dissipative solitons generate smooth, coherent frequency combs with repetition rates locked to the resonators' free spectral range. Their discovery marked a major step forward in the realization of stable, broadband microcombs for metrology, telecommunications, and spectroscopy [10]. Advances in dispersion engineering, thermal control, and hybrid integration have further improved bandwidth, robustness, and practical deployability [11,12]. The theoretical framework used to describe these phenomena is the Lugiato–Lefever equation (LLE), which models the spatiotemporal evolution of fields in driven Kerr cavities. The LLE has provided deep insights into dissipative solitons, chaos, modulation instability, and the transition to single soliton states [13]. Beyond classical predictions, the LLE also applies to quantum fluctuations and squeezing [14], a prediction confirmed experimentally through squeezed-light generation in Kerr microcombs [15]. These results underscore the relevance of confined nonlinear photonics to emerging areas of quantum information science. The performance of optical frequency combs depends critically on two parameters: the repetition rate (which determines the line spacing) and the carrier-envelope offset frequency (which determines the absolute comb position). Both must be stabilized, often through locking to atomic clock Refs. [16,17]. The frequency of each comb line is given by $f_{\rm rep} + f_{\rm ceo}$, and any drift in $f_{\rm rep}$ or $f_{\rm ceo}$ directly impacts comb accuracy. In resonator based combs, the repetition rate equals the cavity's free spectral range $FSR = 1/t_r$, where t_r is the round-trip time. Temporal dissipative Kerr solitons circulating in the cavity thus generate highly stable frequency combs whose spacing is tied to the resonator geometry. Temporal dissipative Kerr soliton based combs offer numerous advantages: intrinsic phase coherence, low timing jitter, and the potential for octave-spanning operation through dispersive wave emission or soliton Cherenkov radiation. These properties underpin a wide spectrum of applications ranging from precision metrology to coherent telecommunications and microwave generation [5,18–24]. Exceptional stability in optical resonators surpassing that of electronic or microwave sources, has enabled leaps in precision measurement capabilities [25]. The foundational importance of optical frequency combs was recognized by the 2005 Nobel Prize in Physics awarded to Hansch and Hall [17,26]. Among the various comb-generation platforms, Kerr microresonators have received particular attention due to their high Q-factors, large FSRs, low power requirements, and compatibility with chip-scale integration [27–30]. Wideband combs, including octave [13] and multi-octave generation [29,31], are now feasible in highly engineered resonator geometries (see Fig. 1).

The tunability of Kerr frequency combs stems from group velocity dispersion engineering via resonator shaping [32]. In anomalous-dispersion WGM resonators, the interplay between Kerr nonlinearity and material dispersion naturally yields equidistant comb lines [33]. Modern microresonators fabricated in compatible platforms can achieve quality factors up to 10^9, enabling the generation of ultrashort pulses and broadband spectra [34,35]. Their compactness, robustness, and low power consumption make them promising for industry implementations in optical communications, aerospace, spectroscopy, and precision metrology [8,36–39]. Mode-locked lasers remain an essential complementary platform for frequency-comb generation, producing bright and dark solitons in propagation regimes, including dissipative solitons and more complex bound states [7,40,41]. These systems offer high pulse energies, low noise, and broad spectral coverage, making them indispensable for a wide range of applications. To ensure long term stability, frequency combs require careful control of f_{rep} and f_{ceo}. Repetition rate stabilization is typically achieved by locking the cavity length of a laser or microresonator to a microwave reference derived from an atomic clock [26]. Offset-frequency stabilization is commonly implemented using an $f-2f$ interferometer, which compares doubled spectral components to measure and lock f_{ceo} [16]. Continuous feedback stabilization of both parameters ensures high-precision comb performance suitable for demanding metrological tasks [42].

At the heart of frequency comb generation lies the interplay between optical nonlinearity, dispersion, cavity dissipation, and external coherent driving. When light is confined within high-quality resonators, nonlinear interactions are greatly enhanced, giving rise to a wide range of self-organized structures and dynamical behaviors. These include modulation instability, Turing patterns, dissipative solitons, front propagation, oscillatory states, and spatiotemporal chaos. Understanding these phenomena is crucial both for controlling frequency-comb generation and for exploring fundamental processes of pattern formation and self-organization in driven-dissipative nonlinear systems.

A particularly successful framework for describing these phenomena is provided by the Lugiato–Lefever equation (LLE), originally introduced as a mean-field model of passive optical cavities. Over the past decades, the LLE has become the cornerstone of the theoretical description of Kerr frequency combs, enabling the understanding of a rich hierarchy of nonlinear states ranging from homogeneous steady solutions and periodic patterns to dissipative Kerr solitons and complex chaotic regimes. Its versatility has made it one of the most important models in nonlinear optics and photonics.

This review aims to provide a comprehensive and unified perspective on the interplay between light confinement, nonlinear optical interactions, and frequency-comb generation in passive resonators and integrated photonic systems. We begin by reviewing the fundamental physical mechanisms governing nonlinear optical processes and the role of optical confinement in enhancing light–matter interactions. We then discuss the various material platforms and resonator architectures that have enabled efficient frequency-comb generation, including fiber cavities, whispering-gallery-mode resonators, crystalline microresonators, silicon-based photonic devices, and emerging integrated photonic technologies.

Particular emphasis is placed on the theoretical description provided by the Lugiato–Lefever equation and its extensions. Beyond the standard Kerr cavity model, we examine the influence of several important physical effects, including polarization dynamics leading to vector dissipative solitons, Raman–Kerr frequency combs, spectral filtering, spatially inhomogeneous pumping, and delayed-feedback control. These extensions significantly enrich the dynamical landscape of passive optical resonators and provide additional mechanisms for controlling the generation, stability, motion, and interactions of dissipative Kerr solitons.

The review further highlights recent advances in dissipative soliton physics, dispersion engineering, and hybrid photonic integration, which have considerably expanded the range of accessible operating regimes and applications. These developments have enabled the realization of highly coherent and broadband Kerr frequency combs suitable for applications in sensing, spectroscopy, coherent optical communications, microwave generation, optical signal processing, and emerging quantum photonic technologies. Beyond their technological relevance, driven nonlinear optical resonators constitute an exceptional laboratory for investigating fundamental concepts of nonlinear science, including bifurcation theory, symmetry breaking, front propagation, self-organization, and chaos. A wide variety of dynamical regimes can emerge from the competition between nonlinearity, dispersion, driving, and dissipation, leading to the coexistence of homogeneous steady states, periodic patterns, breathing solitons, drifting dissipative Kerr solitons, and highly complex spatiotemporal dynamics.

Finally, we address the current challenges and future perspectives in the field, including the scaling and stabilization of frequency-comb sources, the development of novel integrated platforms, and the exploration of increasingly complex nonlinear behaviors. Particular attention is devoted to the characterization of spatiotemporal chaos through modern tools from dynamical systems theory. Using Lyapunov spectra and the Kaplan–Yorke dimension as key diagnostic measures, we discuss how high-dimensional chaotic states emerge in driven optical cavities and coexist with dissipative Kerr solitons and homogeneous solutions. These investigations provide a deeper understanding of the fundamental mechanisms governing dissipative nonlinear systems and establish a unified framework linking dissipative solitons, Kerr frequency combs, pattern formation, and spatiotemporal chaos in modern photonic resonators.

2. Periodic and dissipative Kerr solitons

2.1. Retrospective view

The study of systems far from thermodynamic equilibrium has revealed a remarkable capacity for spontaneous organization, challenging the classical view that order inevitably decays over time. In contrast to equilibrium systems, where fluctuations are damped and entropy tends to increase monotonically, non-equilibrium systems can exhibit persistent, highly organized structures sustained by continuous fluxes of matter and energy. These structures, termed *dissipative structures*, were first conceptualized by Ilya Prigogine in the context of irreversible thermodynamics [43,44]. They represent a fundamental paradigm shift, demonstrating that irreversibility can be a source of order rather than disorder.

Dissipative structures arise through nonlinear interactions and feedback mechanisms that amplify fluctuations beyond a critical threshold, leading to symmetry breaking and pattern formation. A distinctive feature of dissipative structures, in contrast to the structures of conservative systems such as crystalline or periodic solutions, is that they act as attractors: when disturbed, they have the ability to repair and rebuild themselves. This phenomenon is not confined to a single domain of physics; rather, it spans a wide range of disciplines, from fluid dynamics and chemical kinetics to optics, biology, and even ecology [45–52]. The principle underlying these structures is self-organization, whereby local interactions give rise to coherent macroscopic patterns without external design. Self-organization can manifest in space, producing stationary patterns such as convection rolls or chemical concentration waves, or in time, generating oscillatory behaviors and propagating fronts.

A seminal example of spatial self-organization is provided by Turing instability in reaction–diffusion systems [53]. Here, the interplay between diffusion and nonlinear chemical kinetics destabilizes a homogeneous state, leading to periodic structures with an intrinsic wavelength determined solely by dynamical parameters. Conversely, in thermal convection, as first reported by Bénard [54], the transition from conduction to convection in a fluid layer heated from below produces a regular array of convection cells whose size is dictated by the system's geometry, an extrinsic constraint. This phenomenon was first explained by Rayleigh using fluid dynamics theory [55]. The first experimental confirmation of dissipative structures characterized by an intrinsic wavelength was provided by Castets et al. [56] and subsequently by Ouyang and Swinney [57] through investigations of the chlorite–iodide–malonic acid (CIMA) reaction. Decades earlier, Belousov had anticipated the oscillatory dynamics of chemical systems and demonstrated the capacity of concentration waves to propagate [58,59].

In their groundbreaking work, Luigi Lugiato and René Lefever introduced a mean-field model to describe transverse pattern formation in nonlinear optical cavities [60]. They developed a model—later known as the Lugiato–Lefever Equation (LLE), which is a damped, driven, and detuned adaptation of the well known nonlinear Schrödinger equation commonly used in nonlinear fiber optics. Their goal was to study how spatiotemporal patterns emerge in a dissipative, diffractive, and nonlinear Kerr cavity driven by a continuous laser pump. To achieve this goal, they developed a model-later known as the Lugiato–Lefever Equation (LLE) which is a damped, driven, and detuned adaptation of the well-known nonlinear Schrödinger equation commonly used in nonlinear fiber optics. Later, the LLE model has been successfully applied to dispersive optical ring cavities [61], left-handed materials [62], whispering gallery mode cavities [63], and integrated ring resonators [64,65]. The LLE model has been derived in early reports to describe the plasma driven by a radio frequency field [66,67] and the condensate in the presence of an applied ac field [68]. Earlier studies on transverse patterns focused on bistable systems illuminated by a Gaussian beam [69,70]. The originality of the Lugiato–Lefever equation (LLE) lies in its prediction of transverse electric field structures that appear without requiring a switching process or an inhomogeneous input beam. Most importantly, Lugiato and Lefever demonstrated that the symmetry breaking mechanism behind spontaneous transverse pattern formation is fundamentally analogous to the classical Turing instability [43,53]. A key feature of the self-organized structures arising from that instability is that their wavelength is intrinsic to the system's dynamics. In other words, the wavelength of these dissipative structures depends solely on the system's parameters, rather than on its size or boundary conditions. It has served as the fundamental framework for studying broadband microresonator based optical frequency combs [28], first experimentally demonstrated in [8]. Over the past 30 years, the LLE has evolved into a widely used model for exploring the dynamical properties of laser fields confined within nonlinear optical resonators.

Beyond these classical cases, recent decades have witnessed growing interest in dissipative Kerr solitons (DKS), a distinct class of dissipative patterns that coexist with a homogeneous background and exhibit remarkable stability under non-equilibrium conditions [71–75]. Dissipative structures are the dissipative counterpart of the solitons in dissipative systems. In other words, they are localized solutions characterized by a precise position and an attractive nature. Unlike extended periodic patterns, LSs are spatially confined and often arise through subcritical bifurcations, or front pinning.

2.2. Bridging the driven-damped Sine–Gordon and Lugiato–Lefever equations

An oscillator is characterized by its natural frequency. When driven at or near this frequency, it responds most strongly, producing large oscillations. This happens because the energy added by the external force matches the energy lost through damping, creating a balance. This phenomenon is called resonance, and it is efficient because the system absorbs energy without waste [76]. Resonance is a fundamental concept in physics and engineering that enables the control and manipulation of oscillators. Resonance has been studied since Galileo's work on pendulums [77]. When an oscillator is subjected to a force close to its natural frequency, nonlinear effects can occur, leading to asymmetric amplitude responses, bistability, and even chaotic behavior at high force levels.

To establish a rigorous correspondence between the optical resonator described by the Lugiato–Lefever equation and a mechanical system composed of a forced and damped chain of pendula shown in Fig. 2, we adopt the continuum limit as

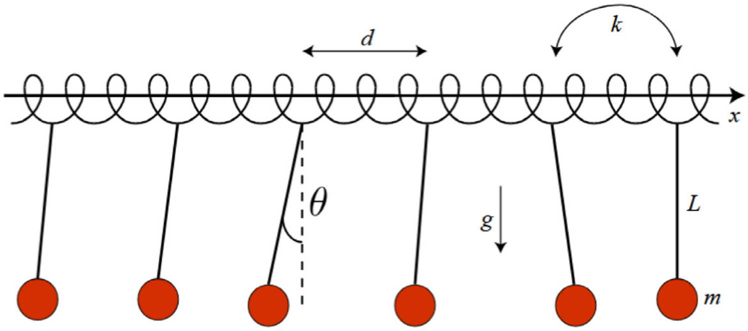

Fig. 2. Schematic representation of a chain of coupled pendulums by springs, where L, m, d, and K are the natural length, mass of the pendulums, distance between two consecutive pendulums, and the elastic constant of coupling.

the modeling framework. This approach enables the transition from a discrete array of coupled pendula to a continuous medium, thereby facilitating the analytical treatment of collective dynamics and wave propagation phenomena. By considering this limit, the mechanical system can be the following partial differential equation [78]

$$\ddot{\theta}(z,t) = -\omega_0^2 \sin\theta - \mu\dot{\theta} + k\partial_{zz}\theta + \gamma\sin(\omega t), \tag{1}$$

Here, $\theta(z,t)$ denotes the angular displacement of a pendulum with respect to the vertical axis at spatial coordinate z and time t. The parameter ω_0 represents the natural frequency of the pendulum, while μ, k, γ, and ω correspond to the damping coefficient, the elastic coupling constant, the amplitude, and the frequency of the external forcing, respectively. For analytical convenience, the external forcing is assumed to be harmonic. When there are no outside forces or friction ($\gamma = \mu = 0$), the system behaves like the well-known *sine–Gordon model*, which is completely reversible in time, like watching a movie forward or backward without any difference. Picture a row of pendulums connected together (Fig. 2).

If we introduce friction, the pendulums eventually stop and settle in a straight vertical position ($\theta(z,t) = 0$), which becomes the only stable state. Now, if we start applying an external push, the pendulums begin to swing back and forth at the rhythm of that push. How big these swings get depends on how close the push's frequency is to the pendulum's natural swinging rhythm $\nu = \omega - \omega_0$. If the timing matches perfectly, the swings grow large, just like pushing a playground swing at the right moment. For example, when soldiers march across a bridge in step, their synchronized rhythm can match the bridge's natural frequency, causing dangerous vibrations. That is why soldiers are ordered to break step when crossing bridges, to avoid resonance that could lead to collapse.

To analyze the dynamics of the driven damped sine–Gordon equation, we consider the quasi-reversible limit, which is essentially the time-reversal limit perturbed by small energy injection and dissipation. In this regime, the model reduces to a perturbed sine–Gordon equation with parameters scaled as $\nu \sim \mu \sim \varepsilon$ and $\gamma \sim \varepsilon^{3/2}$, where $\varepsilon \ll 1$ is a small parameter [79].

Using the ansatz:

$$\theta = \frac{2\varepsilon}{3\omega_0} F(x,\tau) e^{i\omega t} + \frac{\varepsilon^{3/2}}{6\omega_0} F^3 e^{i3\omega t} + \text{c.c.} + \text{h.o.t.} \tag{2}$$

where $F(x,\tau)$ is a slowly varying envelope and $\tau = \varepsilon t$, $x = \sqrt{2\varepsilon\omega_0/z}$.

We substitute into the original equation and collect terms by order in $\varepsilon^{1/2}$. At leading order, the envelope A satisfies the Lugiato–Lefever equation. We substitute into the original equation and collect terms by order in ε. At leading order, the envelope A satisfies the Lugiato–Lefever equation. At order $\varepsilon^{3/2}$, we obtain the envelope equation is given by [79,80]:

$$\partial_\tau F = -(\tilde{\mu} + i\nu)F - i|F|^2 F - \frac{i}{k}\partial_x^2 F - \tilde{\gamma}. \tag{3}$$

The term $\tilde{\mu}$ represents linear damping and accounts for energy dissipation within the system. The parameter ν denotes the frequency detuning and introduces a phase shift with respect to the cavity resonance. The nonlinear term $i|F|^2F$ corresponds to the Kerr nonlinearity, describing self-phase modulation whereby the phase of the field depends on its intensity. The term $i\partial_x^2$ represents spatial or temporal coupling through diffraction or dispersion, respectively, and governs the spreading of the field envelope. Finally, the external driving term $\tilde{-}\gamma$ supplies energy to the system, compensating for the losses induced by damping.

The Eq. (3) has been derived first to describe plasma driven by radio frequency under an applied AC field [66,67]. In the conservative AC field limit, where $\gamma \to 0$ and $\tilde{\mu} \to 0$ admit analytical solutions because, in this limit, the model is integrable [47,81–84].

3. Theoretical description of passive optical resonators

3.1. Reduction of the Maxwell–Bloch equations to the Lugiato–Lefever equation

The Maxwell–Bloch equations describe the interaction between an electromagnetic field and a two-level atomic medium under semiclassical assumptions: the electric field is treated classically, while the matter is described quantum mechanically. In this framework, the medium is modeled as an ensemble of atoms with two discrete quantum states, and the field–matter interaction are simplified through standard approximations, namely the slowly varying envelope approximation and the mean-field approximation [85,86]. Under these approximation, the delayed Maxwell–Bloch equations are

$$\frac{\partial E}{\partial \tilde{t}} = \gamma_c[-(1+i\Delta)E - 2CP + E_i + ia\nabla^2 E] \tag{4}$$

$$\frac{\partial P}{\partial \tilde{t}} = \gamma_\perp[-(1+i\delta + ED)] \tag{5}$$

$$\frac{\partial D}{\partial \tilde{t}} = \gamma_\parallel\left[1 - D - \frac{E^*P + EP^*}{2}\right] \tag{6}$$

where E is the cavity field with decay rate γ_c, E_i is the injected signal which is real and positive, P and D are the atomic polarization and population difference with decay rates $\gamma_\parallel$ and $\gamma_\perp$, respectively. $\Delta = (\omega_c - \omega_e)/\gamma_c$ and $\delta = (\omega_a - \omega_e)/\gamma_\perp$, where ω_c, ω_a and ω_e are the cavity, atomic, and external field frequencies, respectively. The cooperativity parameter is denoted by C. $\tilde{\eta}$ is the delay amplitude. The transverse Laplacian, which describes diffraction in the paraxial approximation, is given by $\nabla^2 = \partial^2_{\tilde{x}\tilde{x}} + \partial^2_{\tilde{y}\tilde{y}}$. a is the diffraction coefficient.

The Maxwell–Bloch equations are essential for understanding and managing the interaction between light and matter in resonant optical systems. They have enabled the development of lasers, the study of nonlinear phenomena like solitons, pattern formation, and the oscillatory and chaotic behaviors of light, and have contributed to progress in quantum and photonic technologies [87–89].

The Maxwell–Bloch equation are formed by five real partial differential equation. In order to simplify the analysis, we consider the good cavity limit ($\gamma_c \ll \gamma_\perp, \gamma_\parallel$), the material variables P and D are adiabatically eliminated, and the resulting equation is the delayed LL model

$$\partial_{\tilde{t}} E = E_i - (1+i\theta)E - \frac{2C(1-i\delta)}{1+\delta^2+|E|^2}E + ia\nabla^2 E, \tag{7}$$

We now turn to the regime of large atomic detuning, commonly referred to as the pure dispersion limit. In this case, it is appropriate to expand and approximate the nonlinear term in the Lugiato–Lefever equation Eq. (7), we get

$$\partial_t E = E_i - (1+i\Delta)E + i\nabla^2_\perp E + i|E|^2 E, \tag{8}$$

This equation is valid in the regime of relatively low optical power. In this operating range where microresonators generate frequency combs, the dynamics can be described either by the Lugiato–Lefever equation (LLE) [60] or by coupled-mode equations [33]. As we will show in the next section, the applicability of the LLE is restricted to small detuning and to weak linear and nonlinear contributions. Moreover, in this regime, the characteristic nonlinear length is much larger than the cavity length

3.2. Modeling passive optical resonators with the Ikeda map

The Nonlinear Schrödinger Equation (NLSE) is a fundamental equation in nonlinear optics and wave physics. It describes how the envelope of a slowly varying electric field evolves in a nonlinear medium, such as a Kerr medium, where the refractive index depends on the light intensity. In its simplest form for one-dimensional propagation, the NLSE is [86,90,91]:

$$\partial_z E = \frac{i}{2k}\left(\partial_x^2 + \partial_y^2\right)E - \frac{i\beta_2}{2}\partial_t^2 E - k'\partial_t E + i\frac{kn_2}{n}|E|^2 E. \tag{9}$$

$E = (x, y, t, z)$ is slowly varying envelope. The nonlinear refractive index is $n_2 = 3n\chi^{(3)}/2$ with n being the linear refractive index, and $\chi^{(3)}$ is the diffraction coefficient is inversely proportional to the modulus of the wavenumber in the cavity material, $k = \omega_0 nl/c = 2\pi n/\lambda_0$, where ω_0 is the injected field frequency, λ_0 is the vacuum wavelength, n is the linear refractive index, and c is the speed of light.

When a light pulse propagates through a medium, it travels at the group velocity v_g, which is generally less than the speed of light in vacuum. If we describe the pulse using the laboratory time t, the pulse appears to move along the propagation axis z, making the analysis more complicated because the envelope changes position as well as shape. To simplify this, we switch to a moving reference frame that travels with the pulse. This is done by introducing the retarded time variable. The retarded time τ is defined as:

$$\tau = t - \frac{z}{v_g} \quad \text{or equivalently} \quad \tau = t - k'z, \tag{10}$$

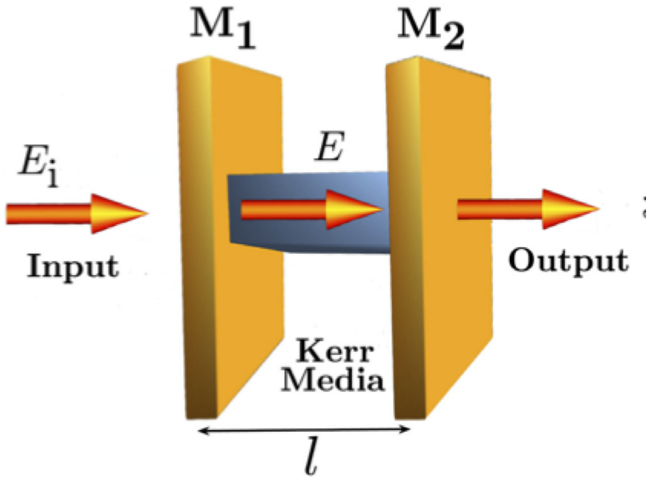

Fig. 3. Schematic setup of an optical cavity filled with a Kerr medium. The cavity is driven by an external field E_i. The mirrors M_1 and M_2 are identical, with reflection and transmission coefficients denoted by ρ and θ, respectively.
Source: Reproduced with permission from Ref. [91] @Copyright(2022) by Optica Publishing Group (Optica).

where $k' = \partial k/\partial\omega$ is the group velocity. The pulse center is stationary in τ. Eq. (9) becomes:

$$\partial_z E = \frac{ik}{2}\nabla_\perp^2 E - \frac{i\beta_2}{2}\partial_\tau^2 E + i\gamma|E|^2 E, \tag{11}$$

where $\nabla_\perp^2 = \partial_{xx}+\partial_{yy}$ is the transverse Laplacian acting in the plane (x, y) perpendicular to the optical axis z. This diffraction term becomes important in broad-area devices, where the optical field can spread significantly in the transverse plane. The second-order chromatic dispersion is denoted by β_2. Dispersion governs the temporal evolution of optical pulses and is responsible for pulse broadening or compression during propagation. The nonlinear coefficient $\gamma = 2\pi n_2/\lambda_0$, with n_2 the Kerr nonlinear index, is associated with self-phase modulation (SPM), a nonlinear propagation effect arising from the Kerr effect, in which the refractive index depends on the optical intensity. Using scaling:

$$(x, y) \to \frac{(x, y)}{\sqrt{k}}, \quad \tau \to \frac{\tau}{\sqrt{|\beta_2|}}, \quad E = \left(\frac{n}{kn_2}\right)^{1/2} F. \tag{12}$$

We obtain the dimensionless NLSE:

$$\partial_z F = \frac{i}{2}\left(\nabla_\perp^2 \pm \partial_\tau^2\right) F + i|F|^2 F. \tag{13}$$

This equation governs the evolution of the electric field envelope in Kerr media, and predicts phenomena such as soliton formation and beam collapse.

The optical cavity is driven by a coherent plane wave, which enters through one of the mirrors. At the input mirror, the injected field combines coherently with the intracavity field, resulting in a superposition that governs the cavity dynamics (see Fig. 3). This interaction is described by the boundary condition:

$$F_{p+1}(0, x, y, z) = \rho F_p(l, x, y, z)\, e^{i\phi_0} + \theta F_i, \tag{14}$$

where $F_{p+1}(0, x, y, z)$ is the intracavity field envelope at the input after the $(p+1)$th round trip. The cavity length is denoted by l. The reflection and transmission coefficients of the mirrors are respectively and the injected field amplitude is F_i. The relation Eq. (14) describes how the intracavity field evolves from one round trip to the next. The phase shift ϕ_0 accounts for the linear phase accumulated over a single round trip.

The nonlinear Schrödinger Eq. (13), associated with the boundary conditions of the cavity Eq. (14), defines an infinite-dimensional discrete map describing the evolution of the intracavity field from one round trip to the next. Within the mean-field framework, which assumes a high-finesse cavity and a large Fresnel number, this discrete mapping can be reduced to a single partial differential equation known as the Lugiato–Lefever equation. Depending on the physical context, the Lugiato–Lefever equation has been formulated in its spatial form [60], temporal form [61], and spatiotemporal form [92].

In what follows, we reduce the infinite discrete map described by the nonlinear Schrödinger equation, supplemented by the cavity boundary conditions in Eq. (14), to a partial differential equation in which time is treated as a continuous variable. Because the round-trip time t_r is typically very short, the intracavity field changes only slightly from one round trip to another. In Kerr optical cavities, the field dynamics naturally separate into two distinct temporal scales. The fast time, often called the retarded time, describes the temporal structure of the optical field within a single round trip and captures the shape of the circulating pulse. The slow time t represents the gradual evolution of the intracavity field over many round trips, accounting for processes such as nonlinear interactions, dispersion, and cavity losses. To perform this reduction, it is necessary to introduce the continuous the continuous time when converting the discrete map index p by a continuous time t for the modeling of the field envelope evolution at the input of the cavity $z = 0$. This can be realized by defining the continuous variable $F(t, x, y, \tau)$ and its derivative $\partial_t F(t, x, y, \tau)$

$$F(t = pt_r, \mathbf{r}) = F^p(z = 0, \mathbf{r}) \text{ and} \tag{15}$$

$$t_r \partial_t F(t = pt_r, \mathbf{r}) = F^{p+1}(z = 0, \mathbf{r}) - F^p(z = 0, \mathbf{r}). \tag{16}$$

where the vector $\mathbf{r} = (x, y, \tau)$ represents the spatial coordinates (x, y) together with the fast-time coordinate τ.

When the cavity has a high finesse, its resonances are narrow, and the injected field couples efficiently to the cavity only when the system operates close to resonance. In the high-finesse limit, the transmission coefficient is much less than unity, i.e., $\rho \approx 1 - \theta^2/2$. As a result, a non-zero intracavity field is sustained only in the vicinity of resonance, where the round-trip phase shift. Under these conditions, both the linear cavity detuning $\delta_0 = 2\pi m - \phi_0$, with m an integer, and the nonlinear phase shift $l|F|^2$ must be much smaller than unity. We further assume that the cavity length is much shorter than the characteristic dispersion and diffraction lengths of the intracavity field. Under these approximations, the cavity boundary condition Eq. (14) reduces to

$$F^{p+1}(0, \mathbf{r}) = \theta F_i + \left(1 - \frac{\theta^2}{2} - i\phi_0\right) F^p(l, \mathbf{r}) \tag{17}$$

Averaging the nonlinear Schrodinger equation Eq. (13) over one cavity length, combining Eq. (17), using Eqs. (16), and assuming θ, δ_0, $l|F|^2$, and l are small, yields the generalized Lugiato–Lefever equation,

$$\partial_t F = \sqrt{\theta} F_i - (\kappa + i\delta_0 - i\gamma l |F|^2) F + il\left(\nabla_\perp^2 + \frac{\beta_2}{2}\partial_\tau^2\right) F. \tag{18}$$

We introduce the following scaling:

$$(x, y) \to \sqrt{\frac{l}{2q\kappa}}(x, y), \quad (t, \tau) \to (\kappa t, \sqrt{\kappa}\tau), \quad F_i \to \sqrt{\frac{\kappa}{\gamma\theta l}} E_i, \quad F \to \sqrt{\frac{\kappa}{\gamma l}} E. \tag{19}$$

Under these changes, the generalized LLE Eq. (18) becomes dimensionless [92–94]:

$$\partial_t E = E_i - (1 + i\Delta)E + id(\nabla_\perp^2 + \partial_\tau^2)E + i|E|^2 E, \tag{20}$$

where $\Delta = \delta_0/\kappa$ denotes the cavity detuning, while $d = \pm 1$ specifies the dispersion or diffraction regime under consideration.

3.3. Continuous-wave solutions, bistability, and pattern-forming instabilities

The homogeneous steady-state (continuous-wave) solutions of Eq. (20) are

$$E_i^2 = |E_s|^2 \left(1 + (\Delta - |E_s|^2)^2\right). \tag{21}$$

For $\Delta < \sqrt{3}$ ($\Delta > \sqrt{3}$) the transmitted intensity as a function of the input intensity E_i^2 is monostable (bistable). A second-order critical point occurs where the output–input characteristic curve exhibits an infinite slope. The critical detuning at the onset of optical bistability is $\Delta = \Delta_c = \sqrt{3}$. At this critical point, the coordinates of the intracavity and injected fields are as follows:

$$E_c = \frac{3E_{ic}}{4} - i\frac{\sqrt{3}E_{ic}}{4} \quad \text{with} \quad E_{ic}^2 = 2\sqrt{2}/3^{\frac{3}{4}} \tag{22}$$

In optical systems and nonlinear cavities, a Turing bifurcation or dissipative modulational instability marks the transition from a homogeneous light distribution to spatially periodic or localized intensity patterns. The homogeneous steady state undergoes a Turing bifurcation at:

$$|E_m| = 1 \text{ and } E_{im}^2 = 1 + (1 - \Delta)^2 \tag{23}$$

Above the threshold for dissipative modulational instability, a finite band of Fourier modes ω becomes unstable, defined by $\omega_-^2 < \omega^2 < \omega_+^2$, where

$$d\omega_\pm^2 = 2|E_s|^2 - \Delta \pm \sqrt{|E_s|^2 - 1} \tag{24}$$

The dependence of $\omega_\pm^2$ on the intracavity field intensity is shown in Fig. 5. For $|E_m| < 1$, all temporal modes are damped, and the homogeneous steady state remains stable. When $|E_m| > 1$, a band of unstable modes emerges, indicating the onset of modulational instability. These unstable modes promote the growth of small perturbations, driving the intracavity field away from the homogeneous steady state and leading to the formation of a stationary spatially periodic pattern that

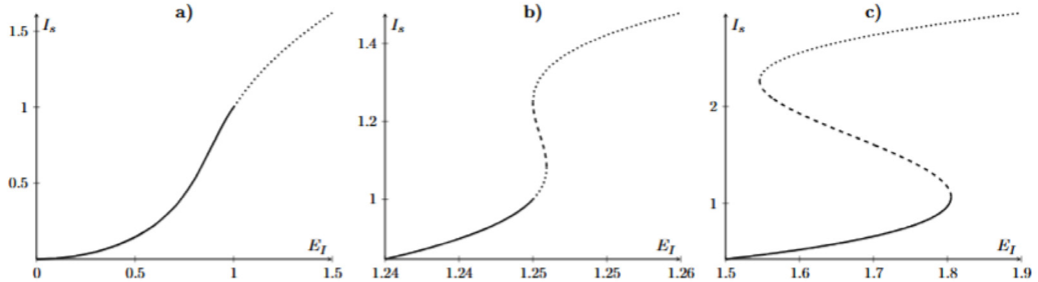

Fig. 4. The homogeneous states as a function of the injected field amplitude. (a) $\Delta = 1$ (b) $\Delta = 1.75$ (c) $\Delta = 2.5$. Solid lines represent stable solutions, dashed lines, unstable ones.
Source: Reproduced with authorization from [95].

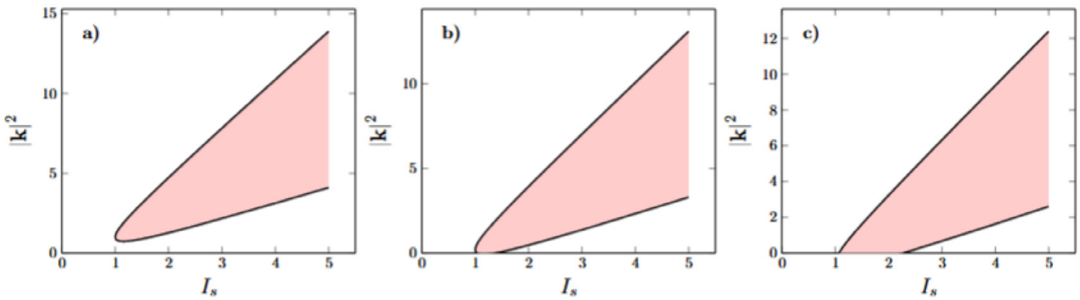

Fig. 5. Marginal stability curves delimiting unstable domains with respect to the modulational unstability for values of the frequency detuning. (a) $\Delta = 1$ (b) $\Delta = 1.75$ (c) $\Delta = 2.5$. The shaded region indicates the parameter region where the homogeneous steady states become modulationally unstable.
Source: Reprinted with permission from [95].

extends throughout the cavity. The homogeneous steady state becomes unstable through a modulational instability when $\omega_- = \omega_+$. The corresponding instability threshold is given by

$$|E_m| = 1 \text{ and } E_{im}^2 = 1 + (1 - \Delta)^2 \tag{25}$$

The critical frequency in the temporal regime or the critical wavenumber in the spatial regime is

$$d\omega_c^2 = 2 - \Delta \tag{26}$$

The outcomes of the linear stability analysis can be divided into two distinct cases:

- The anomalous dispersion or positive diffraction (i.e., $d = 1$), the dissipative modulational instability can arise even within the monostable regime $\Delta < \sqrt{3}$ as shown in Fig. 4(a). Under these conditions, instability occurs when $E_i > E_{im}$. For $\sqrt{3} < \Delta < 2$, a portion of the lower continuous-wave (CW) solution becomes unstable due to modulational instability (MI), specifically within the range $1 < |E_s|^2 < |E_l|^2$ with $|E_l|^2 = [2\Delta - (\Delta^2 - 3)^{1/2}]/3$ represents the lower turning point associated with the bistable response curve. The intermediate CW solution remains unstable even in the absence of chromatic dispersion, while the upper CW solution is unstable for all input injection values satisfying $E_i > E_{im}$. The high-intensity regime, including the upper homogeneous solutions, is always unstable with respect to dissipative modulational instability as shown in Fig. 4(b). For $\Delta > \sqrt{3}$, the lower branch remains completely stable, while the upper branch is always unstable with respect to pattern-forming instability as shown in Fig. 4(c). The marginal stability curves corresponding to the three cases are plotted in Fig. 5.
- In the case of normal dispersion or negative diffraction (i.e., $d = -1$), modulational instability does not affect the monostable regime. Conversely, within the bistable regime and for $\Delta > 2$, a small portion of the lower CW solutions becomes modulationally unstable, specifically in the range $1 < |E_s|^2 < |E_l|^2$. The upper homogeneous solution, however, remains always stable with respect to dissipative modulational instability.

3.4. Periodic patterns and dissipative Kerr solitons in passive optical cavities

In the previous subsection, we addressed the linear regime by determining the threshold for modulation instability (MI) as a function of the injected beam amplitude and frequency detuning, along with identifying the critical wavelength at which this instability emerges. To extend the analysis beyond the critical point associated with MI, a weakly nonlinear approach offers essential insights into the development of nonlinear solution branches. This methodology, originally introduced in seminal works for one-, two-, and three-dimensional configurations, reveals that the bifurcation is supercritical for $\Delta < \Delta_{sub} = \frac{41}{30} \approx 1.36$ and subcritical for $\Delta > \Delta_{sub}$. Since dissipative Kerr solitons arise only in regions where a stable homogeneous state coexists with stable patterned solutions, our focus will be on the subcritical regime. It is noteworthy that the distinction between supercritical and subcritical bifurcations does not coincide with the earlier classification into monostable and bistable regimes; LSs can occur in both cases. The investigation of LSs has sparked new interest recently, since a direct link between LSs of the temporal LLE and Kerr frequency combs (KCs) has been established; It consists of a sequence of equidistant peaks spanning over a broad frequency band. Typically frequency combs are generated deploying mode-locked lasers. Generating KCs in microresonators is a cost-effective alternative to mode-locked lasers. It is therefore of high interest to investigate the possibilities of KC generation in the LLE.

In the following, we examine the formation of LSs in the LLE. Specifically, the relevant parameter region is given by $\Delta = \Delta_{sub} < 41/30$. Thus, the threshold for LS appearance corresponds to $\Delta < \Delta_{sub}$. Regions where $\Delta < \Delta_{sub}$ can be excluded as candidates for LS generation, since in this regime the periodic solution bifurcates supercritically from the homogeneous state, preventing their coexistence. For this purpose, we will use the parameters chosen in the paper [96]. The first theoretical prediction of localized structures was realized in the monostable regime $\Delta = 1.7$ and $E_i = 1.2$. The bifurcation structure of LSs in this regime using the pde2path numerical continuation algorithms from the MATLAB package [97]. As localized states with different numbers of peaks exhibit comparable intensity, visualizing cluster properties is more effective when using the averaged norm will be used as a measure defined as: $L_1 = \int d\xi \; \left|\mathrm{Re}(E - \bar{E})\right|$, where ξ denotes any of the coordinates (x, y, τ) and $\bar{E}$ denotes the mean value of the electric field averaged over the domain. This definition is adopted since the real part of the LS exhibits more pronounced damped tail oscillations than the imaginary part, enabling a clearer distinction between solution branches.

As a function of the injected field amplitude, the L_1-norm exhibits two snaking branches with even and odd numbers of peaks, as shown in Figs. 6, 7. The origin of the snaking type of bifurcation stems from the coexistence of a homogeneous solution and a periodic solution; in this case, the periodic solution is generated by the modulational instability. The stationary solutions associated with the localized solutions is characterized by the homogeneous solutions being hyperbolic fixed points and the periodic solutions being unstable periodic orbits. The manifolds connecting these unstable solutions exhibit heteroclinic entanglement, which is responsible for the emergence of a family of localized solutions organized by the homoclinic snaked bifurcation diagram [98,99].

The presence of two snaking bifurcation diagrams Figs. 6, 7 results from the coexistence of two out-of-phase periodic solutions; this structure is known as *ladders bifurcations* [100]. Alternatively, this snaked bifurcation diagram can be understood as the result of interactions between fronts that connect a homogeneous state to a periodic one [101]. Experimental observation of the snaked bifurcation diagram performed in an optical system [102]. In Fig. 7, the emergence of a single LS (green line), which bifurcates from the first periodic branch (red line) with an odd number of peaks, is depicted. As L_1 increases, each turning, or saddle–node point, where the slope becomes infinite corresponds to the emergence of an additional pair of peaks in the localized pattern. Due to finite size effects, not all wavenumbers or frequencies can be realized in the system. In particular, the Eckhaus instability as a secondary instability of spatially periodic solutions that restricts the range of wavenumbers for which these patterns are stable [103,104]. In an infinite domain, both the periodic branch (plotted in red) and the LS branch (green) bifurcate at the same threshold associated with modulational instability. The single LS then becomes stable in a saddle–node. The solution profile of the single LS is shown in the bottom right of Fig. 6, along with the solution profiles of all the upper branches. The single LS then loses stability in another saddle-node, gaining two additional peaks before stabilizing again as a three-peak solution. This sequence of folds continues until the peaks fill the entire domain, at which point the LS branch reconnects with the first stable periodic branch as shown in the homoclinic snaking Fig. 7. Periodic and dissipative Kerr solitons characterized by odd and even numbers of peaks exhibit multistable behavior [96,106,107]. The existence of dissipative Kerr solitons has been experimentally verified in the temporal regime with a fiber-filled macroscopic resonator [108], and in the spatial regime using liquid crystals acting as a Kerr medium [109]. In the pinning region where the competition between a homogeneous state and a periodic pattern. Within this parameter interval, the fronts connecting the dissipative Kerr soliton to the homogeneous background are pinned, meaning they do not drift [101,106,110]. As a result, localized states neither expand to fill the domain nor collapse, but instead persist with a fixed spatial or temporal extent. The back and forth oscillatory behavior within the pinning region is shown in the bifurcation diagram of Figs. 6, 7, is known as homoclinic snaking (see the overviews on this topic in [98,99,111]). This phenomenon has been thoroughly studied in the LLE [112–114].

Finally, we again employ numerical continuation algorithms implemented in the program pde2path. Rather than using a single continuation parameter with all others fixed, we treat Δ as the primary continuation parameter while allowing the injected field amplitude to vary freely so as to satisfy an additional condition characterizing either a saddle–node or an Hopf bifurcation threshold. This approach enables the tracking of both and Andronov–Hopf bifurcation threshold that delimit the stability of localized states in parameter space. The results are shown in Fig. 8. The blue curve indicates the left saddle–node, which bounds the stability of the single-LS solution, while the green curve marks the location of the right saddle–node. The onset of the first Andronov–Hopf bifurcation is indicated by the red curve. Together, these curves delineate the full parameter region in which stable single LSs exist, shown as the gray-shaded area in Fig. 8.

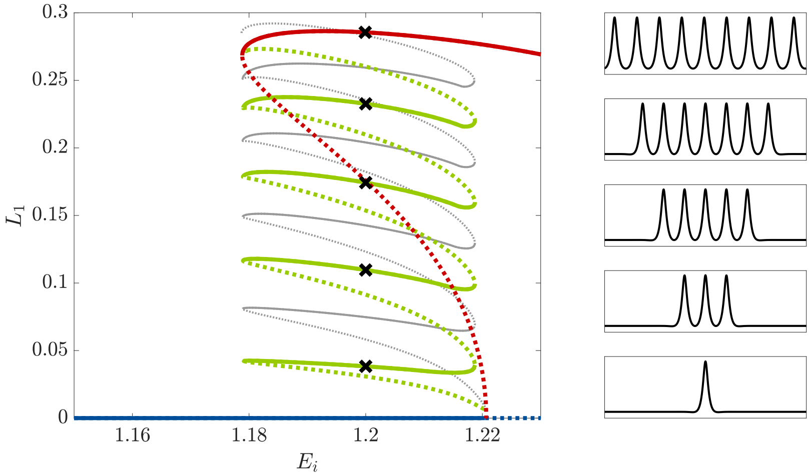

Fig. 6. Bifurcation diagram of Eq. (20) in one dimensional setting obtained in the monostable regime with $\Delta = 1.7$. This diagram showing a snaking curves corresponding to localized patterns with odd numbers of peaks. Solid (dotted) curves indicate stable (unstable) localized solutions. A single DKS branch emerges from the modulational instability at $E_i = E_{im}$ and, through a sequence of saddle–node points, successively gains peak pairs before reconnecting with the periodic branch. The red curve represents periodic structures that fill the entire domain. Thin gray lines denote the even dissipative branch of solutions.
Source: Reproduced with permission from Ref. [105] @Copyright(2022) by Springer.

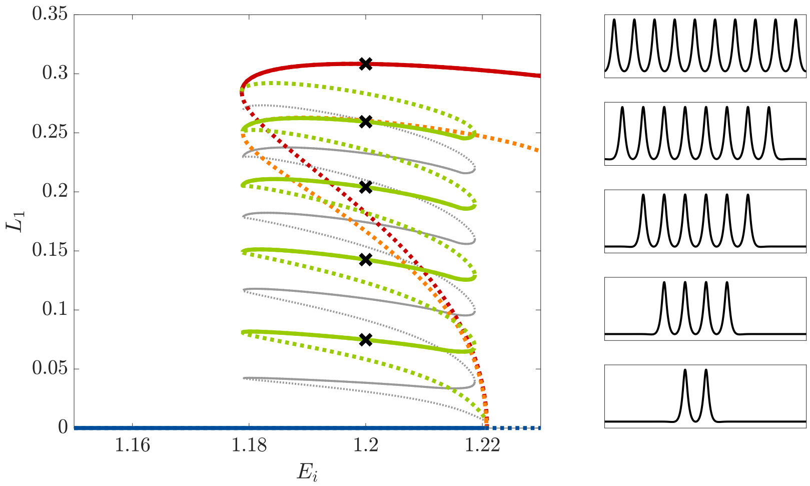

Fig. 7. Bifurcation diagram of Eq. (20) in one dimensional setting showing a Dissipative soliton branch of solutions with an even number of peaks. Same parameter as in Fig. 6.
Source: Reproduced with permission from Ref. [105] @Copyright(2022) by Springer.

3.5. Homoclinic snaking and dissipative soliton interactions

The homoclinic snaking branches displayed in the bifurcation diagram correspond to families of localized bound dissipative Kerr solitons (DKSs) composed of two or more peaks shown in Figs. 6, 7. The existence of these multi-peak states is a direct consequence of the oscillatory nature of the soliton tails. In the parameter regime where the tails decay exponentially while exhibiting spatial oscillations, neighboring solitons can interact over finite distances through the overlap of their tails. This tail-mediated interaction produces an effective force whose sign alternates with the separation distance, leading to successive attractive and repulsive interaction regions [115,116]. As a result, a discrete set of equilibrium distances emerges, corresponding to stationary bound states of DKSs [115,116]. Stable equilibria allow the formation of robust soliton pairs, clusters, and extended localized patterns, whereas unstable equilibria delimit the transitions between neighboring bound configurations.

The organization of these bound states is reflected in the snaking bifurcation structure. Each turn of the snaking branch corresponds to the addition of one or several peaks to the localized state, while preserving the locking mechanism imposed by the oscillatory tails. Consequently, homoclinic snaking can be viewed as the bifurcation-theoretic signature

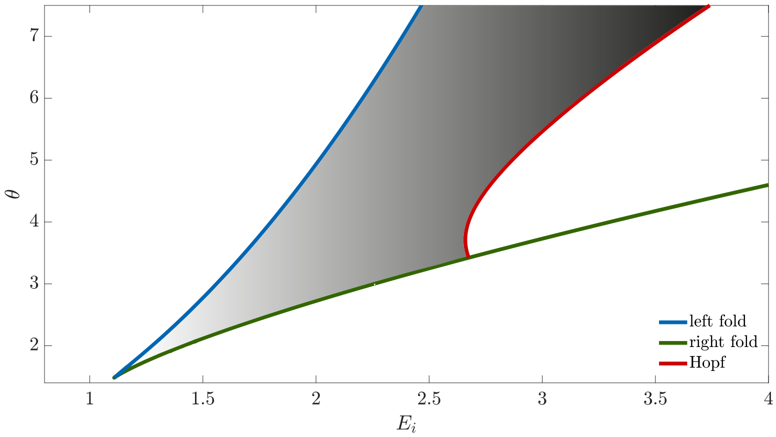

Fig. 8. Stable single-peak localized solution of the Lugiato–Lefever equation Eq. (27) in the plane of frequency detuning and injected field amplitude. The blue (green) curve marks the left (right) saddle–node point, delimiting the existence range of a localized state, as obtained from numerical saddle–node point continuation using pde2path. The red curve marks the Andronov–Hopf bifurcation, while the gray-shaded region indicates the parameter region where a single peak is stable.
Source: Reproduced with permission from Ref. [105] @Copyright(2022) by Springer.

of tail-mediated soliton interactions. The succession of saddle–node bifurcations along the snaking branch generates a hierarchy of localized states with increasing spatial extent and peak number. In this picture, the snaking diagram encodes the sequence of admissible equilibrium separations between neighboring solitons and therefore provides a global representation of the underlying interaction mechanism. From an analytical viewpoint, the interaction between weakly overlapping DKSs can be described by an effective interaction potential derived from the asymptotic expression of the soliton tails. The resulting potential exhibits oscillatory minima and maxima as a function of the inter-soliton distance, in agreement with the alternation between attractive and repulsive interactions. For exponentially damped oscillatory tails, the interaction potential can be expressed in terms of modified Bessel functions, yielding explicit predictions for the equilibrium separations and their stability properties [116]. The close correspondence between the extrema of this interaction potential and the turning points of the snaking branches demonstrates that bounded DKSs and homoclinic snaking originate from the same physical mechanism: the oscillatory tail-induced locking of dissipative Kerr structures. The interaction of well-separated dissipative Kerr solitons (DKSs) has been investigated in the presence of higher-order dispersion effects [117,118] as well as for breathing solitons [119]. More recently, interactions between dissipative solitons mediated by delayed feedback have also been reported [120].

A significant advance in the understanding of multipeak dissipative Kerr solitons (DKSs) was achieved through the investigation of the nascent optical bistability regime, where the dynamics of the system can be accurately described by the variational Swift–Hohenberg equation. Within this asymptotic framework, the concept of relative stability of multipeak localized structures can be rigorously analyzed, providing valuable insight into the organization and selection of bound DKS states. Unlike linear stability, which determines whether a given state can withstand small perturbations, relative stability enables the comparison of different coexisting localized states and identifies those that are energetically or dynamically preferred. The analysis revealed that, in one-dimensional systems, a special parameter value known as the spatial Maxwell point plays a central role in the stability hierarchy of localized structures. At this point, all multipeak states, regardless of the number of constituent peaks, possess the same stability properties and can therefore coexist on an equal footing. Moving away from the Maxwell point breaks this degeneracy: above the Maxwell point, localized states containing a larger number of peaks become progressively more stable than their smaller counterparts, whereas below it the opposite tendency is observed and states with fewer peaks are preferentially selected. This result establishes a direct relationship between the system parameters and the preferred size of localized structures [121].

The notion of relative stability also provides a natural interpretation of the homoclinic snaking structure observed in bifurcation diagrams. Along the snaking branch, localized solutions with different numbers of peaks coexist over a finite parameter range, and their relative stability determines which configurations are most likely to emerge in experiments or numerical simulations. As system parameters are varied, transitions between states with different peak numbers can occur, leading to the growth of localized patterns through the nucleation or annihilation of individual peaks. Consequently, the Maxwell point acts as an organizing center that governs the competition between localized states of different spatial extent and determines the direction of front propagation between homogeneous and patterned regions.

In two-dimensional systems, the situation becomes richer owing to the existence of multiple geometrical arrangements of peaks in the localized pattern. Rather than a single Maxwell point, one finds a family of Maxwell points [121,122]. The relative stability analysis is restricted to regime close to the critical point associated with bistability, where the spatiotemporal dynamics is described by a variational equation. The existence of a Lyapunov functional in this specific regime provides a powerful perspective for understanding the formation, persistence, and selection of multipeak dissipative Kerr soliton (DKS) states. In particular, it explains how localized structures self-organize into stable clusters and why certain bound states.

In two-dimensional systems, the situation becomes considerably richer due to the existence of multiple geometrical arrangements of localized peaks. Instead of a single Maxwell point, one finds a set of Maxwell points associated with different spatial organizations, such as compact clusters [121,122]. This generalized Maxwell framework provides a powerful theoretical perspective for interpreting the formation, persistence, and selection of multipeak DKS states. In particular, it offers a unified description of how localized structures self-organize into stable clusters and explains why specific bound states are preferentially observed in experiments, while others remain only weakly stable or entirely inaccessible. Thus, the concept of relative stability complements the analysis of soliton interactions and homoclinic snaking by establishing a global criterion for the selection and robustness of multipeak dissipative Kerr soliton states.

3.6. Toward the formation of light bullets in optical resonators

Light bullets, also referred to as spatiotemporal solitons [123–125], belong to the class of three-dimensional dissipative Kerr solitons. They were initially predicted in Kerr media by accounting for the combined effects of diffraction, chromatic dispersion, nonlinearity, external pumping, and dissipation. The theoretical description of this problem leads to a three-dimensional generalization of the Lugiato–Lefever equation [92–94].

We have highlighted the existence of three-dimensional dissipative Kerr solitons, characterized by simultaneous confinement of light in both space and time. These structures, known as light bullets, circulate inside the optical cavity at the group velocity of the electric field. This work has been extended to a variety of systems involving optical frequency-conversion processes, including optical parametric oscillators and second-harmonic generation [126–128]. In addition, light bullets have been predicted in wide-aperture lasers with saturable absorbers [129–131], in models governed by the complex cubic-quintic Ginzburg–Landau equation [132–135], and in non mean-field descriptions of nonlinear resonators incorporating saturable absorbers [136,137].

In free propagation, light bullets are intrinsically unstable as a result of beam collapse. In conservative systems, they are nonetheless referred to as light bullets because their stabilization can be achieved through a balance between self-focusing nonlinearity, two-dimensional diffraction, and dispersion [138]. Using a multiscale analysis, Leblond derived a three-dimensional model describing the propagation of short optical pulses in quadratic media [139]. The validity of this model, including the effects of walk-off, phase mismatch, and anisotropy, was also examined. In contrast, in dissipative systems such as driven nonlinear resonators, an additional balance between dissipation and external pumping enables the stabilization of light bullets [91,140,141]. An example of such light bullet solutions of the three-dimensional LLE An example of such light bullet solutions of the three-dimensional LLE are shown in Fig. 9(a–f). These structures correspond to stationary solutions of the three-dimensional LLE Eq. (20). They are traveling solutions that appear stationary in the reference frame moving at the group velocity of light within the cavity. The number and spatial arrangement of light bullets in the Euclidean space (x, y, τ) are determined by the seeded initial condition.

Since the amplitudes of light bullets with different numbers of peaks are very similar, it is convenient to represent the dimensionless L_2 norm as a function of the strength of the injected field amplitude, which provides a clear means of distinguishing these solutions defined as $\mathcal{N} = \int |E - E_s|^2 dx\, dy\, d\tau$. The 3D bifurcation diagram in Fig. 9(g) indicates that the emergence of light bullets falls within the well-known category of homoclinic snaking bifurcations. The 3D bifurcation diagram in Fig. 9(g) indicates that the emergence of light bullets falls within the well known category of homoclinic snaking bifurcations. Fig. 9(h,i) displays the transverse cross-section of a single light bullet, revealing its damped, oscillatory tail, which is a characteristic feature of dissipative solitons that establishes a non zero background. Finally, under a radial approximation, the Laplace operator can be reduced to $\nabla_\perp^2 + \partial^2/\partial\tau^2 = \partial^2/\partial r^2 + (2/r)\partial/\partial r$ where $r = (x^2 + y^2 + \tau^2)^{1/2}$. The single-light-bullet solution is shown alongside the profile obtained from direct numerical simulations of the three-dimensional LLE Eq. (20), and the two exhibit very good agreement as shown in Fig. 9(h).

We suggest using chalcogenide glass, which is characterized by a very strong Kerr effect. Chalcogenide glasses are particularly attractive for nonlinear optical applications owing to their exceptionally large Kerr response. Their physical parameters are among the most favorable of any dielectric platform; in particular, the nonlinear refractive index coefficient n_2 can reach values as high as $n_2 \approx 2.3 \times 10^{-17}$ m^2/W. This results in a nonlinearity coefficient of $\gamma \approx 0.144$ W^{-1} km^{-1} for an effective (illuminated) area of $A_{\rm eff} = 25 \times 10^4$ µm^2. The length of the cavity is $l = 1000$ µm and the reflectivity of the mirrors $1 - \theta = 0.95$, so that the optical losses are determined by the mirror transmission as the intrinsic material absorption loss can be as small as 40 dB/km. The wavelength $\lambda_0 = 4$ µm is chosen close to the zero dispersion wavelength. The choice of these physical parameters are from [142,143]. The response to an excitation by an optical injection $E_{\rm i}$, which is the amplitude of the driving field incident on the cavity input mirror M_1 with an intensity transmission coefficient θ, is $P_{\rm in} = |E_{\rm i}|^2$, which is the driving power. The intracavity power is $P = |E|^2$. These two powers are linked through the homogeneous steady states $P_{\rm in} = P[1 + (\delta - P)^2]$. With the above mentioned realistic physical parameters and the dimensionless parameters for which the light bullet exists $E_{\rm i} = 1.21$ and $\delta = 1.7$, the intensity of the injected field should be of the order of 10 MW/cm^2. This is reasonable since it is well below the damage threshold of chalcogenides, which can be as high as 1 GW/cm^2. In these settings, we expect that the spatial width in (x, y) plane will be ≈270 µm and the temporal width of the LB will be ≈0.08 ps for a value of $\beta_2 \approx 20$ ps^2/km and about 1 ps for a value of $\beta_2 \approx 3000$ ps^2/km.

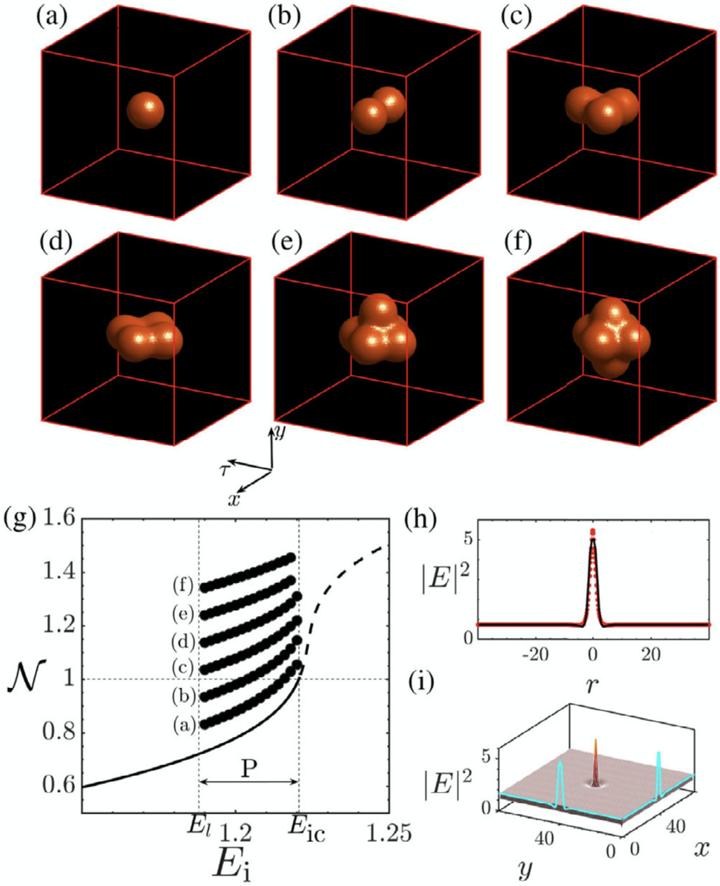

Fig. 9. Three-dimensional isosurfaces of dissipative light bullets and their clustered configurations in a Kerr resonator, displaying up to six localized peaks. (g) Three-dimensional bifurcation diagram for $\Delta = 1.7$. (h) Profile obtained with spherical symmetry approximation (red dotted curve) and the corresponding one-dimensional cross section (black solid curve). (i) Transverse cross-section of a single light bullet. Parameters: $\Delta = 1.7$, $d = 1$, and $E_i = 1.21$.
Source: Reproduced with permission from Ref. [140] @Copyright(2021) by the American Physical Society.

4. Front dynamics and dissipative solitons in the Lugiato–Lefever equation under inhomogeneous pumping

4.1. Dissipative soliton formation under inhomogeneous pumping

The Lugiato–Lefever equation (LLE), in its classical formulation, admits dissipative Kerr solitons over a broad parameter range. In this work, we extend the analysis to the case of inhomogeneous injection. Conventional LLE models assume a spatially uniform injected field, typically represented as a plane wave with constant amplitude in both the spatial and temporal domains. However, the introduction of spatial inhomogeneities warrants investigation for two key reasons. First, minor deviations from uniformity or misalignment of any optical element are unavoidable in experimental configurations and inherently break the translational symmetry assumed in theoretical treatments. This symmetry breaking can significantly influence the formation, stability, and dynamics of LSs. Second, controlled inhomogeneities may offer a practical mechanism for tailoring system properties. Given that the injected beam is comparatively easy to manipulate, this approach could provide a versatile tool for influencing pattern formation and dissipative Kerr solitons in nonlinear optical systems. The generic dimensionless focusing mean-field LLE with inhomogeneous injection reads

$$\frac{\partial E}{\partial t} = E_{in}(\xi) - (1 + i\Delta)E + i|E|^2E + id\frac{\partial^2 E}{\partial \xi^2}. \tag{27}$$

The intracavity field envelope is represented as $E = E(t, \xi)$, where Δ denotes the detuning parameter. For temporal dissipative Kerr solitons in a ring cavity, ξ corresponds to the fast time in a reference frame moving at the group velocity of light within the cavity, while t represents the slow time, proportional to the cavity round-trip duration. In the original LLE formulation for spatial pattern formation, ξ denotes the transverse spatial coordinate of the cavity, and t is the temporal variable. In this context, the negative dispersion coefficient indicates that the system operates in the direct dispersion regime. Likewise, in the spatial domain, the negative coefficient of the second derivative indicates that the system operates in the negative diffraction regime. The proposed model has been formulated for a cavity filled with left-handed material, where negative diffraction leads to wavefronts propagating in the opposite direction compared to conventional diffraction, thereby reversing the typical beam spreading behavior [62]. For clarity and consistency, we designate the inhomogeneity in both scenarios as spatial inhomogeneity. The inhomogeneous injected beam is defined as $E_{in}(\xi)$:

$$E_{\text{in}}(\xi) = E_i + A\,\exp(-\xi^2/B), \tag{28}$$

where E_i is the homogeneous value of the injection, A and $\sqrt{B}$ correspond to the amplitude and the width of the Gaussian beam, respectively.

4.2. Periodic and dissipative Kerr solitons under inhomogeneous injection

Localized structures, such as temporal dissipative Kerr solitons (DKS), are fundamental building blocks in nonlinear optical systems. They arise from the interplay between nonlinearity, cavity feedback, and dispersive or diffractive effects, enabling stable, self-organized states in driven dissipative environments. Inhomogeneities, whether in the driving field, cavity parameters, or material properties introduce additional complexity and control opportunities. Phase or amplitude variations in the pump can pin LSs at specific positions, while imperfections or engineered defects act as trapping sites, influencing stability and dynamics. Combined with chromatic dispersion or spatial diffraction, these inhomogeneities govern bifurcation scenarios, excitability, and pattern formation. Understanding these mechanisms is crucial for applications such as Kerr frequency comb generation, optical storage, and photonic information processing, where precise control of LSs determines system performance.

The original Lugiato–Lefever equation (LLE) assumes a homogeneous driving field, constant in space and time as in previous section. This section extends the analysis to inhomogeneous injection, which is important for two reasons. First, small spatial inhomogeneities are unavoidable in experiments and break translational symmetry, significantly influencing the formation, position, and dynamics of LSs. Second, deliberately introducing controlled inhomogeneities can be advantageous, as the injected beam is relatively easy to manipulate. This approach provides a practical mechanism for tuning system properties and implementing robust control strategies for LSs in nonlinear cavities.

Although the LLE has been extensively studied for decades, the impact of inhomogeneous injection has received far less attention and has only recently emerged as a significant focus in nonlinear optics research. Hendry and colleagues [144] looked at what happens when the usual constant input in the LLE is replaced by a Gaussian-shaped input. They found that dissipative Kerr solitons do not always settle at the highest or lowest points of the input. Instead, they move toward certain preferred values. Another study by Cole et al. [145] shows that changing the input by adding a phase pattern can help create a single DKS more reliably. This works by preventing the system from switching between different numbers of LSs, which often happens in the LLE. Similarly, one can achieve localized states by considering a spatially modulated forcing in the modulation instability region, generating chaotic localized states [146].

Next, we explore what happens when a small inhomogeneity is added to the injected field in a regime where the system is just below the threshold for modulational instability. More precisely, we chose the parameter such that the nonlinear cavity operates in the subcritical modulational instability regime where $\Delta = \Delta_{sub} > \frac{41}{30}$. In addition, we restrict our analysis to the monostable regime where the input–output characteristic is a single-valued function, i.e., $\Delta < \Delta_C = \sqrt{3}$. By using numerical path continuation techniques provided by the Matlab package pde2path [97], the bifurcation diagram associated with dissipative solitons of the LLE with inhomogeneities Eq. (27) is constructed. The results are shown in Fig. 10 where we plot the L_1-norm as a function of the plotted against E_i for different localized state solutions. The L_1-norm is defined as $L_1 = \int d\xi\,|\text{Re}(E - \overline{E})|$, with $\overline{E}$ is the spatial average of the electric field. The blue curve represents the odd branch of classical homoclinic snaking for homogeneous injection ($A = 0$). The homogeneous solution (L_1) loses stability at the Turing point, where both periodic and single-peak LS solutions bifurcate subcritically. The even branch, which starts as a bound state of LSs, is omitted for clarity.

A quasi-homogeneous solution, characterized by $E_{in}(0) = E_i + A$, corresponds to a nearly homogeneous state with a slight peak at the inhomogeneity position. An example is shown in the inset of Fig. 10 as a gray line. The black line represents a localized state with a single peak at the same location. As the injected field amplitude increases, the quasi-homogeneous solution (gray line) becomes unstable, and the system transitions to a stable single-peak localized state (black line). The left saddle–node in the bifurcation diagram shifts toward smaller injection values due to the added inhomogeneity, significantly enlarging the stability region for a single LS, as illustrated by the green curve. Interestingly, the right saddle–node remains almost unchanged, suggesting that LS formation depends on peak injection, while the stability limit is governed by injection at the localized states' edges. This shift creates a parameter range where only the single LS is stable, eliminating multistability with other solutions. The single-peak solution stabilizes at a saddle–node and then adds peaks through successive saddle–nodes until the domain is filled. From an experimental perspective, this greatly simplifies Kerr-comb generation by making single LS states easier to achieve and reducing unwanted transitions. Adding additional peaks increases frequency-comb modulation, with modulation depth growing as the number of peaks rises, as confirmed numerically for homogeneous injection in [114]. This scenario corresponds to the blue curve in Fig. 10. Note that stability is lost, and the system transitions to a single-peak dissipative Kerr soliton, which then becomes stable.

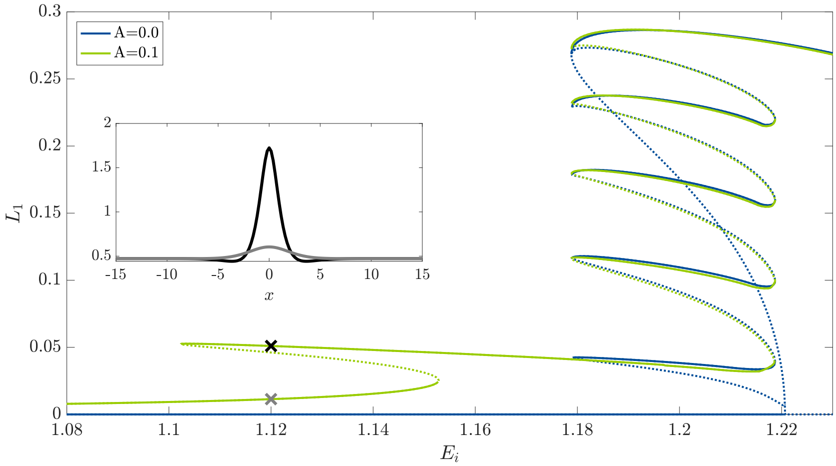

Fig. 10. Snaking bifurcation diagram associated with dissipative Kerr solitons formation under inhomogeneous pumping. L_1-norm of dissipative Kerr solitons as a function of the uniform intensity of the forcing E_i. Continuous and dashed curves account for stable and unstable solutions, respectively. The blue and green curves correspond to the dissipative Kerr soliton, with homogeneous and inhomogeneous forcing, respectively. dissipative Kerr soliton are centered on the inhomogeneity. The inset shows dissipative Kerr solitons, with the respective parameters indicated by the symbols *x*. *Source:* Reproduced with permission from Ref. [147] @Copyright(2019) by the American Physical Society.

The left saddle–node in the bifurcation diagram shifts to smaller injection values due to the added inhomogeneity, greatly expanding the stability region for a single LS. Surprisingly, the right saddle–node remains almost unchanged, indicating that LS formation depends on peak injection, while stability limits relate to injection at the LS edges. This shift creates a parameter range where only the single LS is stable, eliminating multistability with other solutions. Experimentally, this simplifies Kerr-comb generation by making single LS solutions easier to target and reducing unwanted transitions.

Practically, this means that slightly inhomogeneous injection can greatly expand the stability range for single dissipative Kerr soliton (DKS). Moreover, the upper branches of the snaking diagram are barely affected, creating a parameter region where only single DKSs are stable, reducing multistability and simplifying experimental control. The solution centered on the inhomogeneity (blue line, right inset) remains stable for positive values of A, while the solutions fixed on either side of the inhomogeneity (green line, left inset) are stable for $A < 0$ as shown in Fig. 11. These two types of solutions exchange their stability through a transcritical bifurcation at $A = 0$. The centered solution persists, albeit in an unstable state, within a narrow range of $A > 0$ before undergoing a collapse. When the injected field is spatially periodic, interesting work shows that instabilities can generate multispot patterns, rogue waves, breathers, and stable dissipative Kerr solitons [148].

4.3. Formation and propagation of switching fronts in optical bistability

To provide an analytical understanding of front propagation between two stable states, we reduce our analysis to the onset of optical bistability. For this purpose, we introduce a small parameter that measures the distance from the critical point $\epsilon \ll 1$ and we express the cavity detuning in the form $\Delta = \Delta_c(1+\epsilon^2\sigma)$, where σ is a quantity of order one. Then, we decompose the envelope of the electric field into its real and imaginary parts: $E = x_1 + ix_2$ and we introduce a new space and time scales as (ξ, t) $\left(\epsilon^2 t/\sigma, 3^{\frac{1}{4}}\epsilon\xi/(|d|\sqrt{\sigma})\right)$.

Let $(X_1, X_2, Y_{in}) = (x_1, x_2, E_{in}) - (3/4, \sqrt{3}/4, 1)E^c_{in}$ with $E^c_{in} = 2\sqrt{2}/3^{\frac{3}{4}}$ be the deviations of the real, the imaginary cavity field and of the injected field with respect to the values of these quantities at the critical point. Our aim is to seek solutions of Eq. (27) in the neighborhood of the critical point associated with the optical bistability. To this end, we expand the cavity field and the injected field as $(X_1, X_2, Y_{in}) = \epsilon[(u_0, v_0, y_0)+\epsilon(u_1, v_1, y_1)+\epsilon^2(u_2, v_2, y_2)+\cdots]$. Inserting these expansions into the LLE model and using the above scalings, we then obtain a hierarchy of linear problems for the unknown functions. At the first order in ϵ, we find, $Y_0 = 0$ and $u_0 = -w_0$. At the second, we have $Y_1 = 3\sigma/4$. Finally, at the third order, the solvability condition yields

$$\frac{\partial u}{\partial t} = \eta + u - u^3 + \frac{\partial^2 u}{\partial x^2}, \tag{29}$$

where $u(x, t) = \sqrt{3/2\sigma}u_0$ is a scalar field that accounts for the real part of the envelope E and $\eta = 4y_2\sigma/3$ controls the relative stability between the equilibria. Note that y_2 is proportional to the pumping E_{in}. Hence, if the pumping is

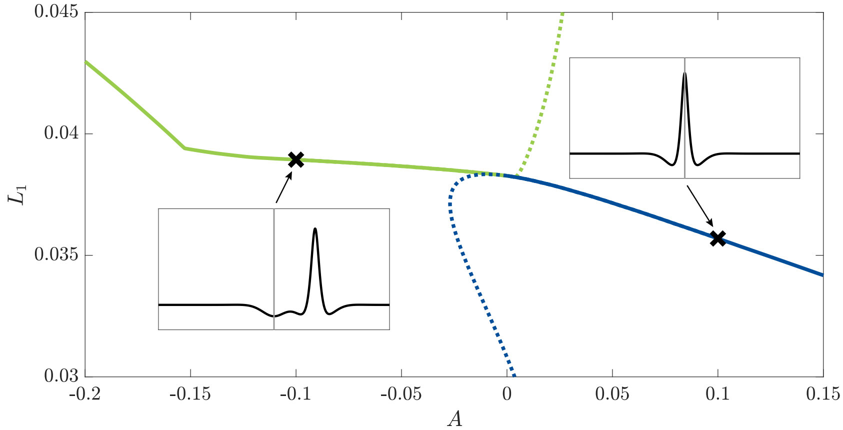

Fig. 11. Magnified view of the bifurcation diagram of dissipative Kerr solitons under inhomogeneous pumping. L_1-norm of dissipative Kerr solitons as a function of the amplitude of the Gaussian *A*. Continuous and dashed curves account for stable and unstable solutions, respectively. The blue and green curves correspond to the dissipative Kerr solitons, with homogeneous and inhomogeneous forcing, respectively. Dissipative Kerr solitons are centered on the inhomogeneity. The inset shows dissipative Kerr solitons, with the respective parameters indicated by the symbols *x*.
Source: Reproduced with permission from Ref. [147] @Copyright(2019) by the American Physical Society.

inhomogeneous, then the parameter η is also inhomogeneous. For a Gaussian pumping, we consider

$$\eta(x) \equiv \tilde{\eta} + \eta_0 e^{-(x/w)^2}, \tag{30}$$

where η_0 accounts for the strength of the spatial pumping beam and w is the width of the Gaussian. For $\eta(x) = 0$, both states are symmetric corresponding to the Maxwell point, where a front between these states is motionless.

To perform analytical developments, we first approximate the Gaussian forcing by a parabola (first-order development close to the center of the optical pumping where the stress is maximum), that is

$$\eta(x) \approx -\tilde{\eta} + \eta_0 \left(1 - (x/w)^2\right). \tag{31}$$

Close to the Maxwell point [149], one can consider the following ansatz for the front solution $u(x,t) = \tanh\left[(x - x_0(t))/\sqrt{2}\right] + W$, where x_0 stands for the front position. This position is promoted to a function of time to account for the effects of inhomogeneity and asymmetry among states. W accounts for small corrections. To get the front dynamic, we introduce the above ansatz for u in Eq. (29), linearizing in W and imposing the solvability condition, we obtain

$$\dot{x}_0 = \frac{-3\sqrt{2}}{2}\left[-\tilde{\eta} + \eta_0\left(1 - \left(\frac{x_0}{w}\right)^2 - \left(\frac{\pi}{\sqrt{6}w}\right)^2\right)\right], \tag{32}$$

that leads to the following trajectory of the front

$$x_0(t) = \pm a \tanh\left(b(t - t_0)\right), \tag{33}$$

with a, b and t_0 are coefficients depending on η_0, $\tilde{\eta}$ and w. The equilibrium position of the front $x_{0\infty}$ can be inferred from expression Eq. (33)) for large time t as

$$x_{0\infty} = \pm w\sqrt{1 - \tilde{\eta}/\eta_0}. \tag{34}$$

This equilibrium positions could be obtained directly from Eq. (29), assuming $\eta(x_{0\infty}) = 0$ which is the condition for motionless front (Maxwell point). Extending this last property to the initial Gaussian forcing, we get

$$x_{0\infty} = \pm w\sqrt{ln\left(\frac{\eta_0}{\tilde{\eta}}\right)}. \tag{35}$$

Numerical simulations of the extended bistable model Eq. (29), are carried out employing a parabolic spatial injection in order to validate the analytical predictions Eq. (31). At the initial stage, the dynamics reveal front propagation, analogous to the scenario observed with a plane wave. The results are shown in Fig. 12. The spatiotemporal evolution of the front, illustrating how its position changes over time under the influence of a parabolic forcing profile (cf. Fig. 12(a). The transverse intensity profile of the front at $t = 4000$, highlighting its shape and localization as shown in Fig. 12(b). The relative front position, providing insight into the dynamics of front displacement, is shown in Fig. 12(c). The Fig. 12(d) displays the front velocity as a function of time. In all plots, blue diamonds correspond to numerical simulation results, while red curves represent analytical predictions, demonstrating strong agreement between theory and computation. The

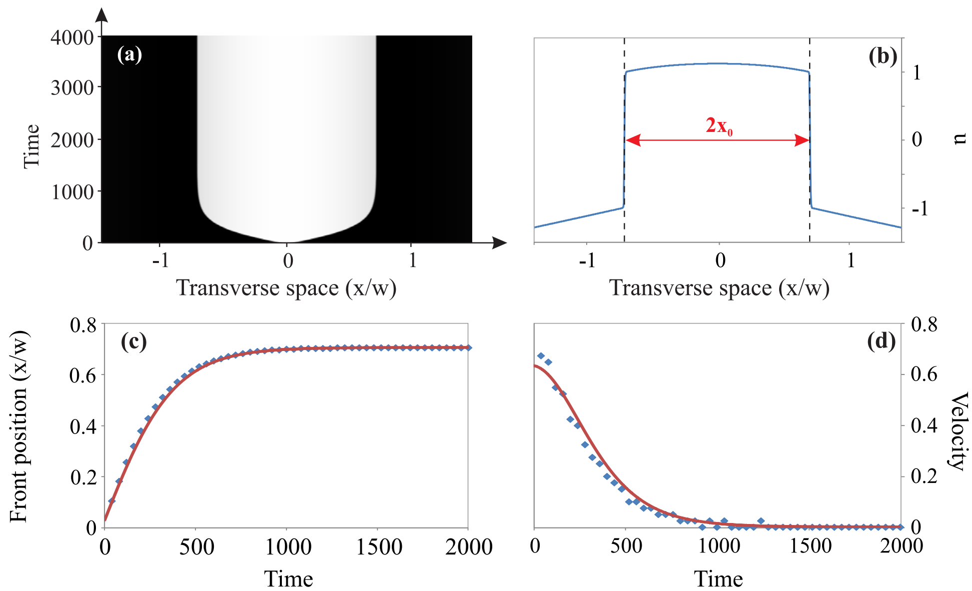

Fig. 12. Numerical study of front pinning with parabolic forcing of the extended bistable system Eq. (29). (a) Spatio-temporal diagram; (b) Transverse profile of the front at $t = 4000$. (c) Relative position of the front $x_0(t)$ (for $x > 0$); (d) Front velocity. The blue diamonds represent the numerical points, and the red curves represent the analytical predictions. Parameters are $\eta_0 = 0.6$, $\tilde{\eta} = 0.3$, $w = 350$.
Source: Reproduced with permission from Ref. [150] @Copyright(2014) by the American Physical Society.

hyperbolic tangent always allows the frontal trajectory to be reproduced. The best-fit results, based on expression Eq. (33), are depicted by the dashed curves.

4.4. Experimental observation of front dynamics in a Kerr cavity with negative diffraction

Experiments used a 50 μm Kerr liquid crystal layer inside a Fabry–Perot resonator with an intracavity 4f lens system enabling tunable optical path length. This configuration allows continuous control of diffraction from positive to negative, effectively creating an equivalent left-handed Kerr material in the visible range. Numerous systems are known to operate in the negative diffraction regime. Through periodic modulation of the refractive index, the sign of the diffraction coefficient can be inverted [151], as demonstrated in atomic Bose–Einstein condensates [152] and dissipative nonlinear photonic crystal resonators [153–160]. Other examples of negative diffraction systems include near self-imaging resonators [161] and, more recently, left-handed materials [62,162,163]. Additionally, the zero-diffraction regime has also been explored in [164].

The experimental setup consists of two plane mirrors, $M_{1,2}$, with an intracavity 4f lens arrangement (L_1 and L_2, see Fig. 13), which images the real mirror M_2 onto its virtual counterpart M_2'. Consequently, the equivalent optical cavity was bounded by M_1 and M_2 (see Fig. 13), with an optical length ddd that could be tuned from positive to negative values (positive in Fig. 13). For negative optical path lengths ($d < 0$), a beam propagating along this path experiences negative diffraction. Combined with the positive Kerr index, the setup is equivalent to a Kerr cavity with positive optical distance but a negative Kerr index. This intracavity lens arrangement enables the realization of an equivalent left-handed Kerr material in the visible range and allows continuous tuning of diffraction from positive to negative.

The cavity is pumped by a single-mode, frequency-doubled Nd^{3+}:YVO_4 laser ($\lambda_0 = 532$ nm), with the beam shaped using two cylindrical telescopes. The resulting beam dimensions ($\sim 200 \times 2800\,\mu m^2$) create a cylindrical transverse profile, ensuring that only one spot can form along one axis, effectively rendering the system one-dimensional. The forward-propagating beam is monitored at the output of mirror M_2. In addition to the cavity length d, two experimental control parameters are readily accessible: the maximum input intensity I_0 of the incident laser and the cavity detuning, adjusted via the linear phase shift ϕ over one round trip.

The dynamical regimes strongly depend on the value of ϕ. To ensure stability, the optical cavity length is actively controlled using a weak probe beam orthogonally polarized to the main beam. The cavity incorporates a Kerr focusing nonlinearity, is adjusted to operate within the bistable regime ($\phi < 0$), where the two states correspond to distinct average orientations of nematic liquid crystal molecules, and light exhibits negative diffraction ($d < 0$). This setup can switch between two stable states, each associated with different orientations of liquid-crystal molecules. The main factor we adjust is the amount of light entering the cavity. At low power, the light coming out of the cavity looks almost the

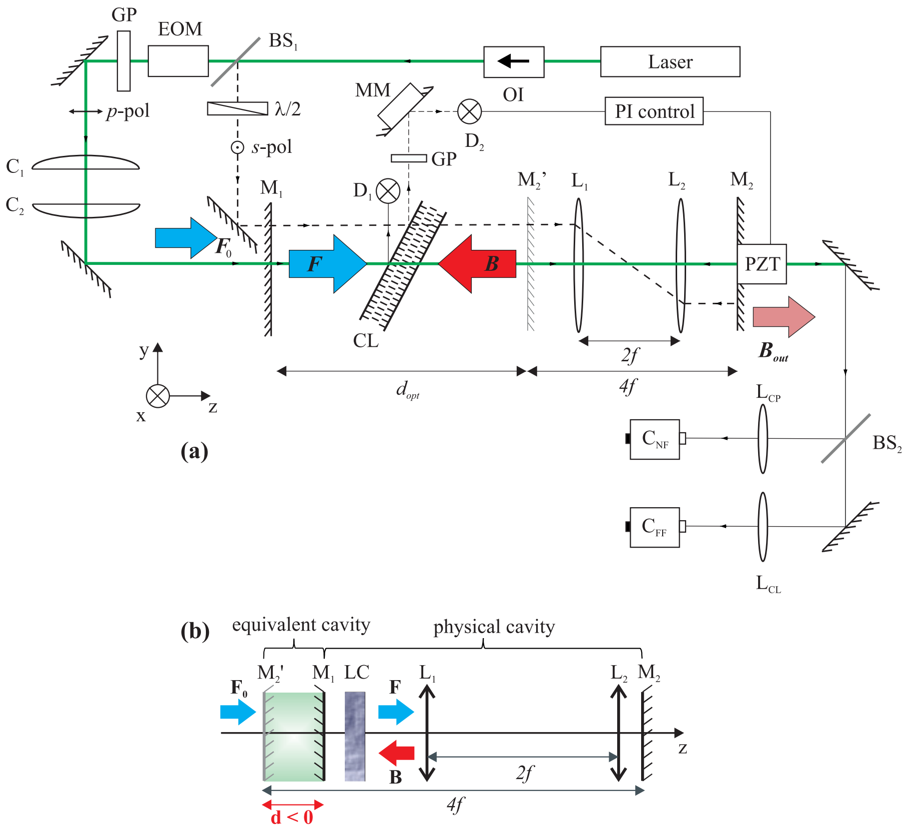

Fig. 13. Inhomogeneous Kerr cavity exhibiting negative diffraction: (a) Experimental setup; (b) Diagram of the physical cavity and its equivalent configuration with negative optical length.
Source: Reproduced with permission from Ref. [150] @Copyright(2014) by the American Physical Society.

same as the input beam with a Gaussian transverse shape as shown in Fig. 14(a,c). When we suddenly increase the power, the center of the light pattern becomes much brighter and spreads outward before stopping [see Fig. 14(a,c)]. Eventually, the pattern stabilizes into a localized "spot" of light. This localized state settles at positions about 17% of the beam width from the center, where the light is only slightly dimmer than at the center. This shows that two different patterns can exist side by side. Random fluctuations cause the boundaries to appear and move toward each other, then stop.

Fig. 15 presents the experimental and numerical time evolutions of the front position of the LLE Eq. (27). The results demonstrate that Eq. (33) accurately captures the front dynamics. Consequently, spatial forcing influences front propagation by inducing oscillatory movements and ultimately stabilizing the front at an asymptotic position, following a hyperbolic tangent trajectory.

4.5. Propagation fronts in passive cavities with synchronization mismatch

The system is a passive fiber ring resonator synchronously driven by a train of pump pulses. Synchronization mismatch ($\Delta \neq 0$) produces a convective term in the reduced intracavity model, effectively advecting localized perturbations (or switching fronts) along the fast-time coordinate. Chromatic dispersion appears as a second-order operator that spreads filters the field in time. In this context, convection refers to the effect of a temporal drift or mismatch between the circulating pulse and the pump pulse inside the cavity. Mathematically, it appears as a term proportional to $\Delta T \partial_\tau E$ in the governing equation, representing a first-order derivative that shifts the pulse in time. Physically, it means the pulse moves relative to the pump envelope, which can destabilize steady-state solutions.

Experimentally, the schematic setup employing synchronous synchronization mismatch, which increases the peak power over the continuous-wave-driving regime, is depicted in Fig. 16. Synchronously pumped by a mode-locked Nd:YAG laser delivering 180 ps (FWHM) pulses at 1064 nm with an 82 MHz repetition rate. Precise cavity length control was achieved using a mechanical fiber stretcher, enabling synchronization tuning with a resolution of ±50 fs. During bistability measurements, the input power was held constant while cavity detuning (Δ) was varied by applying a triangular signal to a piezoelectric stretcher. Fig. 17 presents hysteresis loops for different synchronization mismatches. Increasing synchronization mismatch (convection) reduces the parameter window for bistability and may fully inhibit switching front

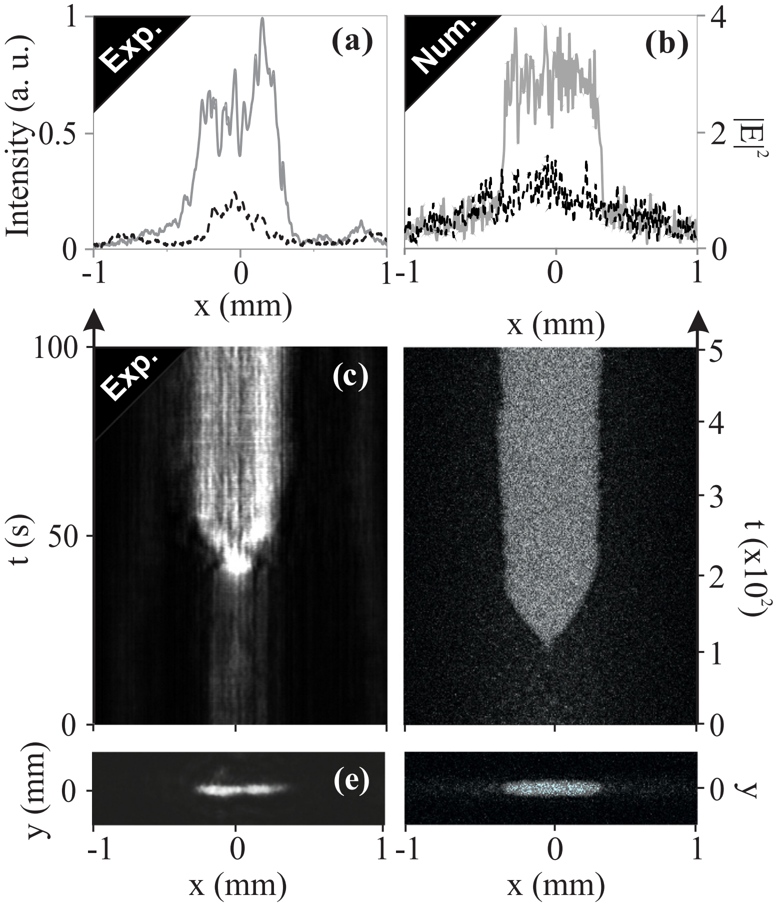

Fig. 14. Front propagation in the negative diffractive inhomogeneous Kerr cavity. (a) and (b) Transverse cross-section of the initial (final) average dissipative Kerr soliton shown by the dashed black (solid gray) line. (c) and (d) Spatiotemporal response to a step function of the input intensity from the lower to the upper branch of the bistable cycle. (e) and (f) Experimental and numerical cross-section of the localized state. The light region accounts for the high intensity of the light. (a), (c), and (e) Experiments with $I_0 = 433$ W/cm2, d $= -5$ mm, $\phi = -0.6$ rad, $w_x = 1400$ μm, $w_y = 100$ μm, $R_1 = 81.8\%$, and $R_2 = 81.4\%$. (b) and (d) Numerical simulation of the LL model with $E_0 = 1.9$, 3.0, $\alpha = 0.001$, $w_x = 1400$ μm, $w_y = 100$ μm, and $\epsilon = 0.4$.
Source: Reproduced with permission from Ref. [150] @Copyright(2014) by the American Physical Society.

formation unless dispersion is present and sufficiently strong. Conversely, with adequate dispersion, they recover robust bistability and clear evidence of switching waves that mediate transitions between the two states. These observations match their analytical predictions based on the front dynamics described by the extended bistable model Eq. (29) described in Section 4.3 [165,166].

An extension mean-field model to include small synchronization mismatches and the impact on optical bistability is addressed. The analysis revealed that chromatic dispersion is essential for bistability, a conclusion supported by numerical simulations and experimental observations [165,166]. These findings were interpreted through switching-wave dynamics, for which a simple model in the form of the extended bistable equation. The generality of our partial differential equation and its reduction to a bistable model form highlight the universality of the underlying mechanisms. The interplay between synchronization mismatch (convection) and inhomogeneities can trigger oscillations and excitability of temporal solitons [167,168]. It is now well established that introducing phase or amplitude inhomogeneities into the cavity injected field enables dissipative Kerr solitons to be reliably pinned at specific temporal [144,145,169–174] or spatial positions [175–178]. Using driving fields with phase or amplitude inhomogeneities offers significant benefits over continuous-wave pumping for temporal Kerr dissipative solitons. These include robust soliton trapping at specific positions, enhanced control of soliton dynamics, and improved system performance through optimized locking ranges and reduced timing jitter. A passive photonic-crystal cavity driven by a spatially modulated pump exhibits bistability, modulational instability, and stable Bragg localized structures within the conduction band, providing an early demonstration of truly stationary intraband dissipative states [179]. Pulsed or modulated driving also enables access to higher peak powers, facilitating broader frequency comb bandwidths and expanding soliton-based applications. Furthermore, combining phase

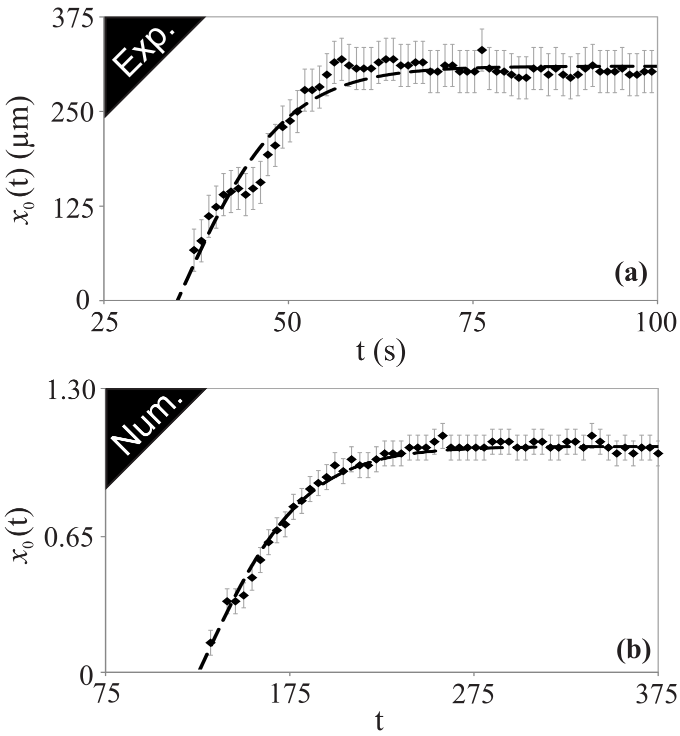

Fig. 15. Temporal evolution of the front position $x_0(t)$ corresponding to the spatiotemporal diagrams of Fig. 14. (a) Experiment and (b) numerical simulations of the LLE Eq. (27) using the same parameters considered in Fig. 14. Diamonds represent the location values extracted from the smoothed spatiotemporal diagrams. Dashed curves are the best fit using expression (5). The experimental fit parameters are a = 308 μm, b = 0.069, and t_0 = 35.2 s; The numerical fit parameters are a = 306 μm, b = 0.017, and t_0 = 107.7.
Source: Reproduced with permission from Ref. [150] @Copyright(2019) by the American Physical Society.

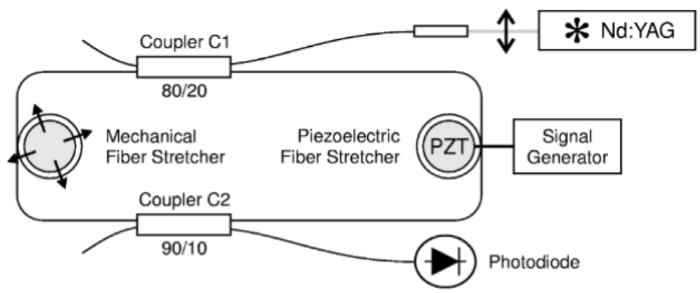

Fig. 16. Schematic setup of a passive fiber ring resonator synchronously pumped by a train of optical pulses.
Source: Reproduced with permission from Ref. [165] @Copyright(1999) by the American Physical Society.

and amplitude inhomogeneities provides additional flexibility for tailoring cavity behavior, paving the way for advanced control schemes and next-generation optical systems.

A another stabilization mechanism for dissipative Kerr solitons formation in passive optical cavities has been proposed [180–182]. This mechanism arises from the interaction of fronts mediated by strong nonlocal coupling. Crucially, the character of the front interaction depends sensitively on the form of the influence function defining the nonlocal coupling. For weak nonlocal coupling, the asymptotic behavior of isolated front solutions exhibits either a purely exponential decay or damped oscillations. In the case of exponential decay, the interaction between fronts is always attractive and decreases exponentially with their spatial separation. As a consequence, any bound states formed through such an interaction remain unstable. Conversely, when the front tails display damped oscillations, the interaction alternates between attraction and repulsion, while its amplitude still decays exponentially with the front separation. This oscillatory nature permits the formation of stable bound states of fronts. This section illustrates a previously unexplored competition between convection and diffusion, diffraction, or dispersion-like transport processes, offering insights relevant to nonlinear optics and other fields of physics.

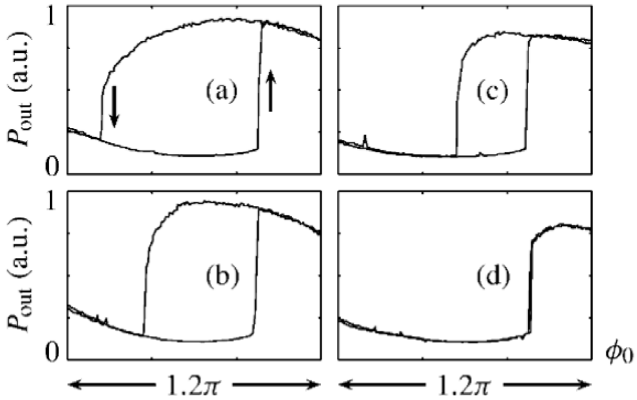

Fig. 17. Hysteresis loops illustrating bistable behavior for (a) perfect synchronization and for synchronization mismatches of (b) 150 fs, (c) 300 fs, and (d) 600 fs. The mean input power is maintained at 2.8 W.
Source: Reproduced with permission from Ref. [165] @Copyright(1999) by the American Physical Society.

5. Delayed feedback control of dissipative soliton dynamics

5.1. Applications of time-delayed feedback

Optical feedback occurs when part of a laser's output is routed through an external cavity or fiber loop and reinjected after a controlled propagation time. The delayed light accumulates a phase shift and interacts with the intracavity field, altering the gain, phase, and stability. Even a small feedback can significantly alter the dynamics of the laser, leading to coherence collapse, low-frequency fluctuations, self-pulses, or chaotic regimes. Beyond studies of laser stability, optical delay systems serve as powerful analog processors in reservoir computing, generate ultra low noise microwave signals in optoelectronic oscillators, and enable secure communications based on chaos (see overviews on this issue [183–189]). The underlying physics is captured by delay differential equations, which exhibit high-dimensional dynamics, multistability, and complex bifurcations [190–195]. Recent advances in integrated photonics now allow precise control of delay lines and feedback strength, enabling the creation of compact, tunable devices that exploit delay-induced effects for modern photonic applications [196,197].

Several theoretical studies have looked at dissipative solitons in semiconductor based devices that experience standard delayed optical feedback. These studies focus on VCSELs that can form CSs either through optical injection [198–201] or by using a built in saturable absorber [202–205]. Typically, optical feedback is modeled as a single round trip of light in an external cavity formed by the VCSEL's output mirror and a distant mirror [206]. Following this idea, we added a feedback term to the mean field model that describes how a broad area cavity semiconductor evolves in space and time [207]. In the absence of delay feedback, experimental evidence of dissipative solitons-known as cavity solitons, has been reported in earlier work in two spatial dimensions [208,209], in the temporal domain [210], and in spatio-temporal [211]. A VCSEL with an external cavity generates temporal vectorial dissipative, solitons localized polarization pulses with constant total intensity [205]. These solitons coexist independently, form bound states, and behave as polarization kinks described by a reduced delay equation model.

5.2. The Swift–Hohenberg equation with delayed feedback

The system under investigation consists of a Fabry–Perot cavity containing two-level atoms without population inversion, driven by a coherent external beam. Delayed optical feedback is implemented via an external mirror placed at a distance L from the right facet of the Fabry–Perot resonator (Fig. 18). The corresponding delay time, $\tau = 2L/c$, represents the round-trip propagation in the external cavity, where c is the speed of light. The delay feedback strength is controlled using an attenuator, which is denoted by $\eta = R(1 - R_F^2)/(TR_F)$, with R is the reflectivity of the external mirror, the Fabry–Perot round trip time T, and R_F denotes the facet reflectivity of the laser cavity. The feedback phase $\phi = \omega_e\tilde{\tau}$, where ω_e is the frequency of the injected signal. To model the delayed feedback, we employ the Lang–Kobayashi (LK, [206]) formalism, which assumes a single longitudinal mode operation and a sufficiently attenuated reflected field that can be represented by a single delay term. Originally, LK introduced two delay differential equations for a single-mode semiconductor laser subject to optical feedback. Numerical simulations have validated the LK model against experimental observations, including mode hopping and chaotic dynamics, for both short and long external cavities [212]. Even in configurations where LK assumptions are violated, such as multimode operation or ultra-short external cavities, the model remains a fundamental reference for extended approaches [213]. A comprehensive treatment of this topic, relying on the LK approximation, has been published [190].

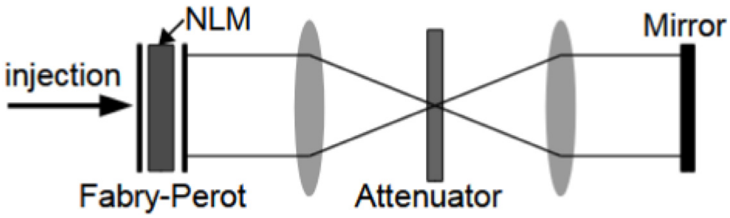

Fig. 18. Schematic setup of a Fabry–Perot cavity with delayed optical feedback and driven by a coherent external injected beam. The nonlinear medium (NLM) consists of two-level atoms. To control the feedback strength, we use an attenuator, and to compensate for the diffraction in the external cavity, we used two lenses.
Source: Reproduced with permission from Ref. [214] @Copyright(2009) by the American Physical Society.

We employ a Pyragas type control scheme in which the delayed feedback is proportional to the difference between the current system state $E(x, y, t)$ and its delayed state $E(x, y, t-\tau)$. More precisely, the delay feedback term is introduced by adding to the first Maxwell–Bloch equation (Eq. (6)) the contribution $\eta \exp(i\phi)[E(x, y, t-\tau) - E(x, y, t)]$. Owing to the specific structure of this type of control scheme, the stationary solutions $E_s(x, y)$ of the delay free system, i.e., $\eta = 0$ remain stationary solutions of the full time delayed system. This invariance arises because the feedback term identically vanishes when the system persists in the same stationary state over a time interval τ. As a result, the formation and propagation of switching fronts in optical bistability introduced in the previous section continue to represent stationary solutions under delayed feedback. Nevertheless, the introduction of time-delayed feedback can substantially modify the stability properties of these LSs.

Starting from the Maxwell–Bloch equations (Eq. (6)) supplemented with time-delay feedback, we perform a multiple space–time expansion in the vicinity of the critical point associated with bistability [215,216]. This procedure yields a reduced scalar model, which takes the form of a delayed Swift–Hohenberg equation (DSHE) incorporating delayed feedback [214,217]:

$$\frac{\partial u}{\partial t} = s + cu - u^3 + a_1\nabla^2 u + a_2\nabla^4 u + \eta[u(x, y, t-\tau) - u(x, y, t)] \tag{36}$$

Stable stationary dissipative Kerr solitons ($\partial u/\partial t = 0$ and $\nabla^2 u = 0$) correspond to homoclinic solutions of Eq. (36). In the absence of delayed feedback, such localized structures exist in the subcritical regime where both the homogeneous state and a branch of spatially periodic solutions are linearly stable [106,107]. However, when the delay term $\eta[u(x, y, t-\tau) - u(x, y, t)]$ is introduced, the Eq. (36) no longer possesses a gradient structure. A typical manifestation of this nonvariational effect is illustrated in Fig. 19. In our case, the external cavity is self imaging, meaning that diffraction between the Kerr medium and the feedback mirror is compensated [199].

The delayed feedback does not modify the homogeneous steady state solutions of the DSHE Eq. (36): $s = u_s(u_s^2 - c)$. For $c < 0$ ($c > 0$) the transmitted intensity as a function of the input intensity Y^2 is monostable (bistable). Localized solutions of the Swift–Hohenberg equation are radially symmetric stationary $u = u_0(\mathbf{r})$, $\mathbf{r} = (\ x \quad y\ )^T$ of the SHE, *i.e.*, it satisfies Eq. with $\eta = 0$ with the cylindrical approximation $\nabla^2 = \partial_{rr}^2 + (1/r)\partial_r$, and boundary conditions are $\partial_r u_0|_{r=0} = \partial_{rrr} u_0|_{r=0} = 0$, and $\lim_{x\to+\infty} u_0 = u_s$. The solution of the linear problem is

$$u_0 = u_s + \Re(A\exp(i\psi))K_0[\sqrt{-\zeta_1 + i\zeta_2}\, r] \tag{37}$$

with $\zeta_1 = k_c$ and $\zeta_2 = \sqrt{3(3u_s - c - 3\Delta^2)}$. The Bessel function K_0 describes the decaying oscillations at large distances from the center of a single LS. The radially symmetric LS is calculated by the shooting method which consist of integrating Eq. (13) with $u_0(r)|_{r=r_0} = B_1$, $\partial_{rr} u_0|_{r=r_0} = B_2$, and $\partial_r u_0|_{r=r_0} = \partial_{rrr} u_0|_{r=r_0} = 0$. Then we solve Eq. (13) with $\partial_r u_0|_{r=0}$ from $r = r_1$ to $r = 100$ for the initial condition of Eq. (37). The parameters A, $B_{1,2}$, C and ψ are determined numerically by matching the solution at $r = r_1$.

Linear stability of this solution can be analyzed by substituting $u = u_0(\mathbf{r}) + \delta X(\mathbf{r})e^{\lambda t + i\omega t}$ into Eq. (36) and collecting the linear in δX terms:

$$L\Psi = \left[\lambda + i\omega - \eta(e^{-\lambda\tau - i\omega\tau} - 1)\right]\Psi, \textit{with} \tag{38}$$

$$L = c - 3u_0^2 + a_1\nabla^2 + a_2\nabla^4 \tag{39}$$

where the linear operator describes the stability of the solution X_0. Any eigenfunction Ψ_μ of the operator L solves Eq. (39) which then leads to

$$\mu = \lambda + i\omega - \eta(e^{-\lambda\tau - i\omega\tau} - 1), \tag{40}$$

Unlike the case without feedback, where the eigenvalues λ come from a polynomial, the inclusion of OF leads to a transcendental characteristic equation containing a delay term $\exp\lambda\tau$, which generally prevents analytical solutions. The parameter μ is the eigenvalue of L corresponding to the eigenfunction Ψ_μ ($L\Psi_\mu = \mu\Psi_\mu$). The solution will be thus stable

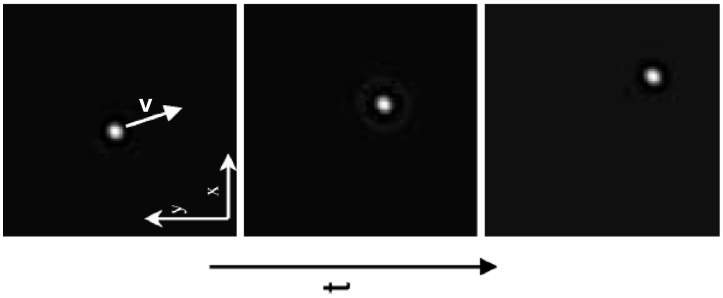

Fig. 19. Moving bright dissipative localized structure under the effect of delayed feedback. $s = 0.25$, $c = 1$, $a_1 = -1.6$, $a_2 = -4/3$, $\eta\tau = -0.98$. These parameter values correspond, e.g., to the reflectivity of the external mirror $r = 0.03$. The cavity length $l = 100$ μm and the external cavity length $L > 3$ cm [212]. Light amplitude maxima are plain white. The integration mesh is 96×96 and the time step is 0.0025.
Source: Reproduced with permission from Ref. [214] @Copyright(2009) by the American Physical Society.

for $\eta \neq 0$ when $\lambda(\mu) < 0$. Bifurcation point corresponds to $\lambda(\mu)$ vanishing at some μ. In the absence of delayed feedback, i.e., $\eta = 0$, we have $\mu \leq 0$.

Due to the translational symmetry operator L has two zero eigenvalues corresponding to the translational neutral (often called Goldstone) modes given by the two components of the vector $(\begin{array}{cc}\Psi_{01} & \Psi_{02}\end{array})^T = \nabla u_0$: they satisfy $L\Psi_{01,02} = 0$. From Eq. (40)) we see clearly that when the feedback strength $|\eta|$ is increased, localized solution $X = u_0(\mathbf{r})$ of Eq. (40) becomes instable at $\eta = -1/\tau$ and this corresponds to $\mu = 0$, $\omega = 0$. At this bifurcation point, the eigenvalue $\lambda + i\omega = 0$ becomes four-fold degenerate with the geometrical multiplicity 2. The corresponding eigenfunctions are the neutral modes Ψ_{01} and Ψ_{02}. At the bifurcation point, each of these two neutral modes corresponds to a 2×2 Jordan block. In what follows, we compute analytically the velocity of a single peak dissipative Kerr solitons near the bifurcation point $\eta\tau = -1$. We assume that near that point, the velocity $v = |\mathbf{v}|$ is small and the single localizes peak preserves its form during the motion. Let $u(\mathbf{r}, t) = u_0(\mathbf{r} - \mathbf{v}t) = u_0(\boldsymbol{\zeta})$. Taylor expansion near $v = 0$ gives

$$u(\mathbf{r} - \mathbf{v}\tau) = u_0 + v\tau u_1 + (v\tau)^2 u_2/2 + (v\tau)^3 u_3/6 + (v\tau)^4 u_4/24 + O(v^5) \tag{41}$$

with $u_0 = u_0(\boldsymbol{\zeta})$, $u_p(\boldsymbol{\zeta}) = (\mathbf{v} \cdot \nabla u_{p-1}(\boldsymbol{\zeta}))/v$, $p = 1, 2, 3, 4$. multiplying both sides by u_1, and integrating from $-\infty$ to $+\infty$, and using

$$\int_{-\infty}^{+\infty} u_1(a_1\nabla^2 u_0 + a_2\nabla^4 u_p)d\boldsymbol{\zeta} = 0 for p = 0, 2, 4 \tag{42}$$

which follows from the symmetry property $u_p(-\boldsymbol{\zeta}) = (-1)^p u_p(\boldsymbol{\zeta})$. we obtain;

$$(1 + \eta\tau)\int_{-\infty}^{+\infty} u_1^2 d\boldsymbol{\zeta} = \frac{\eta v^2\tau^3}{6}\int_{-\infty}^{+\infty} u_1 u_3 d\boldsymbol{\zeta} + O(v^5). \tag{43}$$

In addition, using integration by parts, the integral $\int_{-\infty}^{+\infty} u_1 u_3 d\boldsymbol{\zeta}$ in the right hand side of Eq. (43) can be replaced by $-\int_{-\infty}^{+\infty} u_2^2 d\boldsymbol{\zeta}$. From Eq. (43) we see that when approaching the bifurcation point $v \to 0$, we should have $1 + \eta\tau = O(v^2)$. Due to the rotational symmetry of the delayed Swift–Hohenberg equation, the direction of the localized peak velocity $\mathbf{v}$ is arbitrary. Therefore, the instability leading to the emergence of a moving single localized peak solution can be referred to as a circle pitchfork bifurcation [218]. Let us now consider a small deviation from the bifurcation point, *i.e.*, $\eta = -\tau^{-1} - \epsilon$, with $\epsilon \ll 1$. Substituting this relation into Eq. (43) and neglecting second order terms ϵ^2, we obtain

$$v = \pm Q\sqrt{\frac{6\epsilon}{\tau}} \tag{44}$$

The constant Q has been evaluated numerically. For $\Delta = -0.45$, and $\eta\tau = -1.025$ ($\epsilon = 0.025$), we have $Q \approx 1.33$. To compare with a direct 2D numerical simulations, we first calculate the speed given by Eq. (44) and that of the single 2D dissipative soliton obtained by a direct numerical simulation. This is displayed in Fig. 20. We can see that near the bifurcation point $\eta\tau = -1$ the agreement is very good, while far from this point the numerical velocity becomes smaller than that obtained by numerical simulations. Next, we compare the threshold associated with the motion of the dissipative soliton. Analytically we have $\eta_{th} = -1/\tau$ numerically we obtain $\eta_{num} = -0.98/\tau$. We also see a good agreement between the two thresholds.

5.3. Passive optical cavities with delayed feedback

We have shown in the previous section that the delayed optical feedback strongly modifies the input–output response of the system, with its impact governed by the feedback strength and for a fixed phase. Delayed feedback controls

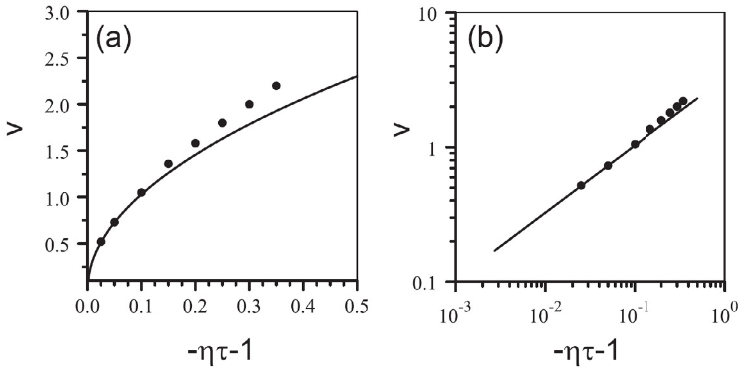

Fig. 20. Velocity of a moving dissipative Kerr solitons as a function of the delayed feedback strength. The solid curve represents the analytically predicted velocity, while the circles denote velocities obtained from numerical simulations. The parameters used are identical to those in Fig. 19. *Source:* Reproduced with permission from Ref. [214] @Copyright(2009) by the American Physical Society.

(DFC) rely on the use of the difference between the system variables at a given moment and their values at a given moment in the past. They have the property that the steady states of the unperturbed problem are solutions to the delayed feedback problem. We have used the simplest delay feedback for a single variable u, provided by the control force $\eta[u(x, y, t-\tau) - u(x, y, t)]$, where η and τ represent the feedback strength and the time delay, respectively. Previous analytical and numerical investigations of the two-dimensional Swift–Hohenberg equation have shown that stable dissipative Kerr solitons can acquire mobility when the condition $\eta\tau < -1$ is satisfied [214,217]. Indeed, this instability corresponds to a spontaneous breakdown of spatial symmetry in a non-variational system. The primary aim of this article is to demonstrate that the transition occurring at $\eta\tau = -1$ corresponds to a bifurcation.

In what follows we investigate the effect of the delayed phase ϕ also controls the width of the modulation instability domain, which can be tuned by small adjustments of the external cavity length on the order of one wavelength. Moreover, delay optical feedback may induce a traveling wave instability, characterized by a pair of complex conjugate eigenvalues with zero real part at a finite wavenumber or frequency. For this purpose we consider the simplest feedback control $\eta \exp(i\phi)E(x, y, t-\tau)$. We incorporate optical feedback into the LLE model Eq. (8) by introducing a self-imaging external cavity together with a single round trip delay term [219]

$$\frac{\partial E}{\partial t} = i\nabla_\perp^2 E - (1 + i\theta)E + i|E|^2 E + E_i + \eta e^{i\phi} E(t-\tau). \tag{45}$$

The inclusion of delayed optical control may also induce a drift bifurcation of the LS, similar to that reported in the case of Swift–Hohenberg equation [214] and the semiconductor based resonators [199,200]. Such a feedback induced LS drift is illustrated in Fig. 21 for the case of $\theta = 2$, $E_i = 1.3$, and delay feedback with a fixed phase $\phi = \pi$ and different strengths $\eta = 0.11$, 0.12, and 0.15. The CS is launched at $t = 0$ and starts moving after a certain delay, which decreases as the feedback strength is increased, see also [199]. Furthermore, the CS moves faster as η is increased. In order to estimate the threshold of the CS drift bifurcation we proceed in a similar way as in [200,201]. Slightly above this threshold, we consider a CS moving uniformly with a small velocity $v = |\mathbf{v}|$ and expand the electric field amplitude in power series of v around $E = E_0(\mathbf{r})$. E_0 is the stationary dissipative Kerr soliton, $\boldsymbol{\xi} = \mathbf{r} - v\,\mathbf{e}\,t$, $\mathbf{r} = (x, y)$, and $\mathbf{e}$ is the unit vector in the direction of the soliton motion. Substituting this expansion into Eq. (45) and collecting the first order terms in small parameter v we obtain

$$L\begin{pmatrix} \mathrm{Re}E_1 \\ \mathrm{Im}E_1 \end{pmatrix} = \begin{pmatrix} \mathrm{Re}[w_{01}(1 + \eta\tau e^{i\varphi})] \\ \mathrm{Im}[w_{01}(1 + \eta\tau e^{i\phi})] \end{pmatrix} \tag{46}$$

with $w_{01} = \mathbf{e}\cdot\nabla E_0$. The linear operator L is given by

$$L = \begin{pmatrix} 1 + 2A_0B_0 & \nabla_{eff}^2 + 2B_0^2 \\ -\nabla_{eff}^2 - 2A_0^2 & 1 - 2A_0B_0 \end{pmatrix},$$

where $A_0 = \mathrm{Re}E_0$, $B_0 = \mathrm{Im}E_0$ and $\nabla_{eff}^2 = \nabla^2 - \theta + |E_0|^2$. By applying the solvability condition to the right-hand side of Eq. (46), we obtain the drift instability threshold

$$\eta\tau = -\frac{X_1 + Y_2}{\cos\phi(X_1 + Y_2) + \sin\phi(Y_1 - X_2)} \tag{47}$$

with $X_{1,2} = \langle\psi_{1,2}^\dagger, \nabla\mathrm{Re}E_0\rangle$ and $Y_{1,2} = \langle\psi_{1,2}^\dagger, \nabla\mathrm{Im}E_0\rangle$. Here, the eigenfunction $\psi^\dagger = \left(\psi_1^\dagger, \psi_2^\dagger\right)^T$ is the solution of the homogeneous adjoint problem $L^\dagger\psi^\dagger = 0$ and the scalar product $\langle , \rangle$ is defined as $\langle U, V\rangle = \int_{-\infty}^{+\infty} UV\,d\mathbf{r}$. For a feedback

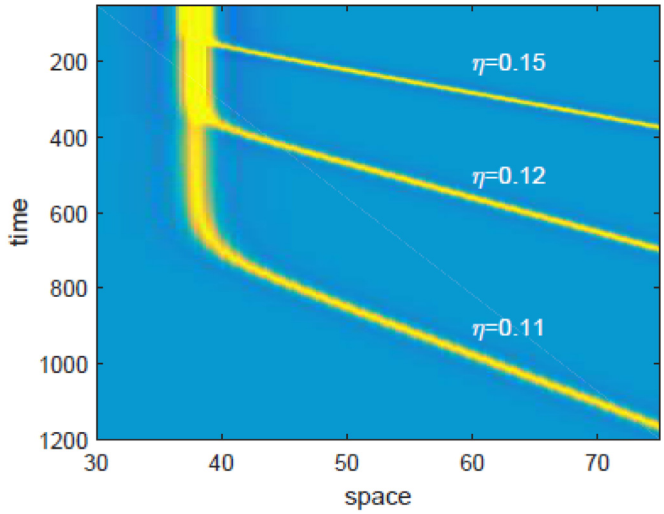

Fig. 21. Moving dissipative Kerr soliton as a function of the delayed feedback strength. The color bar is such that the maximum and minimum are associated with yellow and light blue, respectively.
Source: Reproduced with permission from Ref. [219] @Copyright(2016) by the American Physical Society.

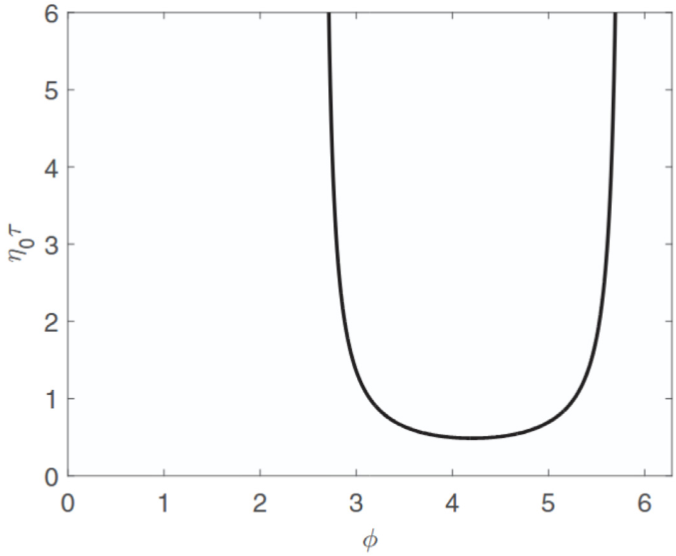

Fig. 22. Moving dissipative Kerr soliton as a function of the delayed feedback strength.
Source: Reprinted with permission from [219]. Reproduced with permission from Ref. [219] @Copyright(2016) by the American Physical Society.

phase of $\phi = \pi$, we recover from (47) the threshold condition obtained earlier for the drift instability of dissipative solitons in the Swift–Hohenberg equation with delayed feedback, $\eta_0\tau = 1$ [214]. In Fig. 22 we plot the threshold values of the product of the feedback strength and delay time $\eta_0\tau$ at onset of CS drift instability as a function of feedback phase ϕ. As previously observed for the VCSEL model in [200,201] the drift instability is only possible in certain windows of the feedback phase.

For relatively low input intensities, it has been demonstrated that the introduction of time delay feedback can give rise to markedly more complex dynamical behavior, including spatio-temporal chaos and the emergence of rogue wave like extreme events. Such phenomena have been reported both in the generic Lugiato–Lefever model [220,221] and in broad area semiconductor laser systems [91,220,222].

6. Polarization dynamics of vector dissipative solitons

6.1. Polarization dynamics in the coupled Lugiato–Lefever equation

The dynamics of dissipative structures in Kerr resonators is generally described by the Lugiato–Lefever (LLE) mean-field model. In this section, the model is extended to include polarization degrees of freedom, leading to a generalized vector LLE. This framework enables the study of vector dissipative Kerr solitons with distinct polarization states and intensities in macro- and microresonators. Stokes parameters are introduced to characterize their polarization properties. We analyze two types of dynamical regimes, corresponding to the anomalous dispersion case and the normal dispersion case.

In free propagation, that is, in the absence of an optical resonator, it has been shown that additional forms of modulational instability may arise. These instabilities can lead to a variety of symmetry breaking phenomena and give rise to a broad range of vectorial nonlinear structures, including domain wall vector solitons, rotating bound states of vector solitons [223], dark-bright vector solitons [224], and vector flat-top solitons [225].

In the anomalous dispersion regime, following reference [2], bright LS resulting from the formation of modulational instability patterns are examined. The added degrees of polarization freedom allow the coexistence of several distinct solutions in the same cavity. In the normal dispersion regime, based on references [226,227], dark LS created by front locking mechanisms are studied in conditions far from modulation instability. At higher mismatches, polarization effects induce tristability among continuous wave solutions, resulting in strong multistability of dissipative Kerr solitons with distinct polarization states. In all cases, intracavity LS exhibits elliptical polarization, even though the cavity is driven by a linearly polarized field.

This analysis applies equally to large fiber cavities and small scale resonators, as long as they contain a birefringent medium whose slow and fast axes are aligned with the x and y directions. The model explicitly includes polarization effects, while neglecting diffraction so that the system's behavior is driven only by the interaction between Kerr nonlinearity and chromatic dispersion along the longitudinal direction. Brillouin and Raman scattering are not considered. Significant attention has been devoted to understanding the polarization behavior of bright dissipative soliton frequency combs, with advances achieved through both theoretical work [228–231] and experimental studies [232,233]. Vector dissipative solitons are commonly divided into two main categories: polarization locked vector solitons and group velocity locked vector solitons. The polarization locked type was first predicted theoretically in [234] and later observed experimentally in [224], mainly in dispersion managed fiber laser resonators. Beyond these well known classes, other forms also exist such as polarization precessing vector solitons, which have been demonstrated in spatial domain experiments [235,236].

This system is described by propagation equations consisting of two coupled nonlinear Schrödinger equations supplemented with the appropriate boundary conditions. The mathematical formulation leads to infinite dimensional maps, which can be reduced to a set of coupled Lugiato–Lefever equations by applying the mean-field approximation both in macroscopic resonators [237] and in microresonators [238]. The resulting dimensionless coupled LLE model is given by [228]

$$\begin{aligned}\partial_t E_{x,y} &= E_{i_x,i_y} + i\left(|E_{x,y}|^2 + b|E_{y,x}|^2\right)E_{x,y}\\ &\quad - \left(1 + i\theta_{x,y} \mp \Delta\beta_1\partial_\tau - i\beta_2\partial_{\tau\tau}\right)E_{x,y},\end{aligned} \tag{48}$$

where The E_x and E_y denote the slowly varying envelopes of the intracavity field associated with the two orthogonal polarization components. In what follows, we consider a linearly polarized injected field with identical amplitudes in both polarization directions, such that $E_{i_x} = E_{i_y} = E_i$. The parameter b represents the cross phase modulation (XPM) coefficient coupling the two components, while θ_x and θ_y denote their respective frequency detunings. The term $\Delta\beta_1$ accounts for the group velocity mismatch arising from first-order dispersion, whereas the second-order dispersion coefficient β_2 is assumed to be identical for both polarizations. In this study, we focus on a macroscopic fiber ring resonator, which permits adopting the standard value $b = 2/3$ for silica fibers [1] and enables the group velocity mismatch to be neglected by setting $b = 2/3$ [1], in line with earlier experimental and theoretical work [233,239,240]. Since $b < 1$, the cavity operates outside the regime in which polarization domain walls may form [232]. Other vector solitons have been demonstrated theoretically and experimentally that dissipative Faraday instability can be realized in a Raman fiber laser, leading to high repetition rate pulse trains and establishing a new dissipative mechanism for mode-locking [241,242].

Recent work has experimentally demonstrated that Kerr dissipative solitons in a polarization symmetric optical ring resonator can undergo spontaneous symmetry breaking, giving rise to coexisting vectorial solitons with asymmetric polarization states [243]. The authors further showed that controlled perturbations enable deterministic switching between these symmetry breaking dissipative soliton states, providing new insight into multimode nonlinear resonators [243]. Other vector resonance multimode solitons and instabilities have been reported in [244].

The continuous wave (CW) solutions of the coupled LLE (48) satisfy:

$$I_{i_x,i_y} = \left[1 + \left(\theta_{x,y} - I_{x,y} - bI_{y,x}\right)^2\right] I_{x,y}, \tag{49}$$

The quantities $I_{i_x,i_y} = E^2_{i_x,i_y}$ and $I_{x,y} = |E_{x,y}|^2$ denote, respectively, the injected intensities and the intracavity intensities associated with the two polarization components. The steady state solutions of Eqs. (49) can exhibit a rich multistable structure: depending on the system parameters, the response curve may display the familiar bistable S-shaped form

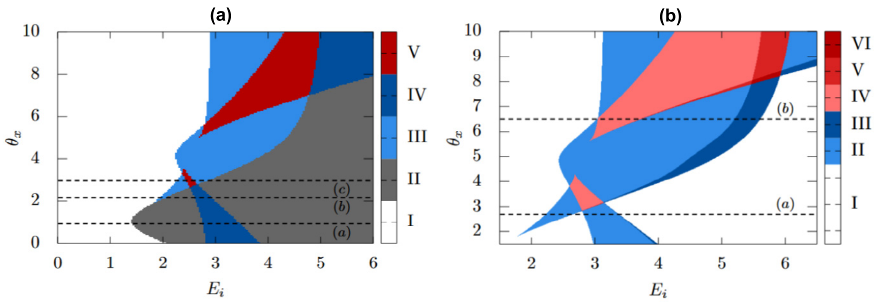

Fig. 23. Equilibria diagram in parameter space and stability of the homogeneous steady states. (a) Anomalous dispersion regime: $\beta_2 = 1 > 0$ with a fixed detuning $\theta_y = 5$. (b) Normal dispersion regime: $\beta_2 = -1 < 0$ with fixed $\theta_y = 4.3$. Each panel displays the stability domains of the homogeneous steady state solutions in the (E_I, θ_x) parameter plane. Color-coded regions indicate the number and nature of the coexisting steady states, distinguishing stable homogeneous branches from modulationally unstable ones. The diagrams provide a global overview of how dispersion, detuning, and polarization coupling shape the monostable, bistable, and tristable regimes accessible to the cavity. The black region denotes parameter values for which the system supports a single stable homogeneous steady state (HSS). In contrast, the blue (dark-gray) region identifies a domain where the HSS is modulationally unstable (MI-unstable). The green (light-gray) area corresponds to a regime in which a stable homogeneous branch coexists with an MI-unstable branch. The red (gray) region marks the coexistence of two distinct MI-unstable states. Finally, the white region delineates parameter values where one stable homogeneous solution coexists with two separate MI-unstable branches. Taken together, this stability map provides a global view of the dynamical behavior supported by the cavity, revealing extensive domains of bistability and multistability arising from the interplay between polarization dynamics, detuning, and external driving.
Source: Reproduced with permission from Ref. [226] @Copyright(2021) by the American Physical Society (APS).

known from the scalar Lugiato–Lefever model, or it may even develop a tri-stable behavior arising from the interplay of birefringence, cross phase modulation, dissipation and detuning. As in the scalar case, these homogeneous steady states may lose stability through modulational instability (MI), thereby providing access to the formation of patterned or localized structures. To characterize these regimes, a linear stability analysis of the continuous wave (CW) solutions is performed by perturbing the steady state with fluctuations of the form $\exp(i\omega\tau + \lambda t)$, where ω is the temporal frequency of the perturbation and λ the associated growth rate. This procedure enables identification of the parameter regions in which the homogeneous state becomes unstable with respect to finite frequency perturbations.

A global summary of the results of this stability analysis is presented in the (E_I, θ_x) parameter plane shown in Fig. 23. These diagrams delineate the various dynamical regimes supported by the cavity and highlight the boundaries between stable homogeneous operation, MI-induced instabilities, and regions of coexistence where multiple steady or unstable branches overlap. In the analysis that follows, we distinguish between two fundamental operating regimes determined by the sign of the group velocity dispersion: the anomalous dispersion regime, illustrated in Fig. 23(a), and the normal-(or direct-) dispersion regime, shown in Fig. 23(b) (see Fig. 23).

The parameter plane can be partitioned into several distinct dynamical regions, each characterized by the number and stability of the homogeneous steady states supported by the system: Region I corresponds to monostability, where only a single stable homogeneous steady state exists. Region II corresponds to bistability between two stable steady states, indicating the coexistence of two physically accessible homogeneous branches. Region III denotes bistability between one stable steady state and one modulationally unstable state. In this regime, the system supports a stable homogeneous solution alongside a second branch that is unstable to finite frequency perturbations. Region IV corresponds to tristability between three stable homogeneous states. This regime reflects a highly multivalued response of the cavity, arising from the combined effects of birefringence and nonlinear cross coupling. Region V represents tristability between two stable states and one modulationally unstable state, indicating partial multistability involving both stable and MI-unstable branches. Region VI characterizes tristability between one stable state and two modulationally unstable states. In this case, the system supports a single stable homogeneous branch coexisting with two distinct MI-unstable branches.

We briefly recall the fundamental concepts required to describe the polarization of light, following the classical framework presented in [245]. From a classical standpoint, an optical field propagates as a transverse electromagnetic wave composed of mutually orthogonal electric and magnetic field components, both lying in the plane perpendicular to the propagation direction. A defining property of such transverse waves is their polarization, which characterizes the temporal evolution of the electric field vector in this transverse plane. When the orientation of the electric-field vector varies randomly in time, with no persistent directional preference, the field is said to be unpolarized. In this situation, successive orientations of the electric field are uncorrelated and no dominant polarization state emerges. By contrast, polarization plays a central role in nonlinear optics and laser physics, where laser sources typically generate quasi-monochromatic fields that are at least partially polarized. To quantitatively characterize polarization, one may consider the transverse components of the electric field, and derive several useful quantities. Among these, the most widely used are the Stokes parameters, where defined as a set of four real quantities that provide a complete and experimentally accessible description of the polarization state of an electromagnetic field: $S_0 = |E_x|^2 + |E_y|^2$ is the total intensity. $S_1 = |E_x|^2 - |E_y|^2$ and $S_2 = |E_x^\star E_y + E_x E_y^\star|$ quantify the relative fluxes of linearly polarized light. Specifically, S_1 measures the

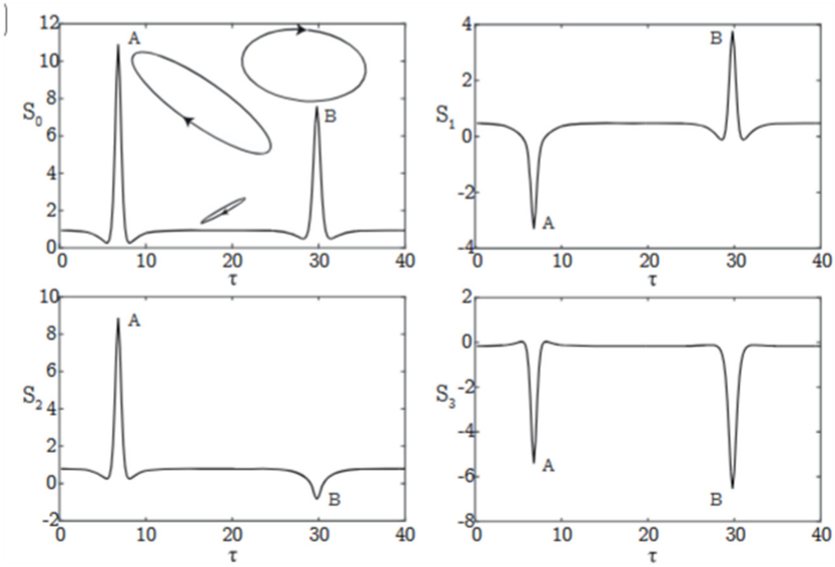

Fig. 24. Numerical simulation of Eq. (49) after 500 time units, represented in terms of the Stokes parameters of the output field. In the upper-left panel (S_0), both the dissipative Kerr soliton and the homogeneous background are annotated with their corresponding polarization ellipses. Parameters are : $E_i = 2.54$, $\theta_x = 2.75$, $\beta_2 = 1$, $\theta_y = 4.3$, and $\Psi = \pi/4$.
Source: Reproduced with permission from Ref. [228] @Copyright(2017) by the American Physical Society (APS).

intensity difference between horizontal and vertical linear polarizations, while S_2 corresponds to the intensity difference between light polarized at 45° ($P_{\pi/4}$) and 135° ($P_{3\pi/4}$) with respect to the x-axis. The circular polarization component is characterized by the parameter S_3, whose sign indicates the handedness of the polarization: $S_3 > 0$ corresponds to right-handed circular polarization, whereas $S_3 < 0$ denotes left-handed circular polarization.

6.2. Coexisting vector dissipative soliton families with different polarization states and peak powers

Polarization instabilities in isotropic, optically injected nonlinear cavities were examined in detail [246]. For linearly polarized injection, those authors demonstrated the occurrence of a pitchfork bifurcation leading to the emergence of two circularly polarized steady states of opposite handedness. They also identified MI regions in both normal and anomalous dispersion regimes. In contrast to that ideal isotropic scenario, the present system exhibits weak birefringence, which fundamentally modifies the structure of the polarization attractors. Instead of circular polarization branches, the cavity supports multiple steady states with distinct ellipticities, thus giving rise to polarization multistability. This behavior is illustrated in Fig. 24 and represents a key qualitative difference from the isotropic case. Spatial propagation is computed using a second-order finite-difference scheme, while time integration is performed with a fourth order Runge–Kutta method. Because the model is formulated in dimensionless variables, all axes in the figures are displayed without physical units. The distinct polarization states of the two dissipative solitons denoted respectively A and B become apparent upon inspection of their Stokes parameters. At its peak intensity, dissipative soliton A exhibits a negative S_1 together with a positive S_2, while soliton B shows the opposite behavior, with a positive S_1 and a negative S_2. Both solitons display a strongly negative S_3, with slightly differing magnitudes, indicating a dominant right-handed circular polarization component [228]. These clear differences in their polarization properties distinguish the present vector solitons from those reported in [247]. In that work, the observed tristability arises from a multivalued stationary state in the form of so called super cavity soliton solutions of the scalar Ikeda map [247]. However, such dynamics cannot occur in the scalar Lugiato–Lefever model, as it does not incorporate polarization degrees of freedom. To construct the bifurcation diagram associated with both types of dissipative solitons, we evaluate $N_0 = \int_{t_r}(|E|^2 - |E_0|^2)d\tau$ and plot this quantity as a function of the driving field amplitude E_i, where $|E_0|^2$, denotes the continuous wave (CW) intensity solutions of Eq. (49). The results is shown in Fig. 25. The two types of LSs coexist only within a finite parameter interval between E_{i1} and E_{i2}. Their profiles types A and B are shown in Eq. (49)(a,b). In the weakly birefringent configuration considered here, polarization multistability plays a crucial role in enabling the coexistence of multiple families of polarization vector locked solitons, each associated with a distinct elliptical polarization state. As we demonstrate below, such coexistence is directly rooted in the multibranch structure of the homogeneous steady state manifold. Related forms of multistability, arising from the coexistence of unstable modes associated with different transverse profiles, have been reported in whispering gallery mode resonators in the form of mixed-mode MI [248]. These results underscore the generality of multibranch and multimode instability mechanisms across a broad class of nonlinear optical resonators.

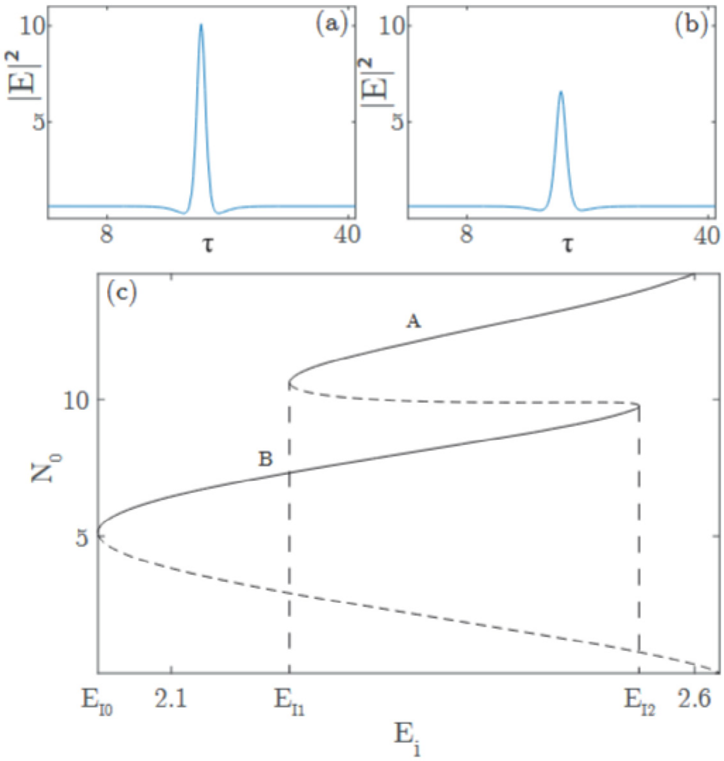

Fig. 25. Bifurcation diagram showing the evolution of the quantity N_0 as the system transitions from the homogeneous background state to a type-A dissipative Kerr soliton, passing through an intermediate type-B structure. Dashed lines represent unstable solutions, while solid lines represent stable ones. Numerical simulations are carried out using the same parameter set as in Fig. 24.
Source: Reproduced with permission from Ref. [228] @Copyright(2017) by the American Physical Society (APS).

6.3. Vector soliton families and domain walls

In this subsection, we investigate the normal dispersion regime by imposing $\beta_2 = -1$. The analysis is conducted within the bistable and tristable parameter regions, sufficiently far from any symmetry-breaking or modulational instabilities. In this parameter range, the system dynamics is primarily governed by the front connections linking the two or more CW's stable solutions.

Front interactions are determined by the nature of their tails. When the tails decay exponentially without oscillations, the interaction is purely attractive and decreases exponentially with the separation between fronts. In contrast, when the tails exhibit damped oscillations, the interaction alternates between attraction and repulsion, with an amplitude that also decays exponentially with distance. The profiles of the vectorial fronts shown in the insets of the $\tau - t$ map of Fig. 26 clearly reveal the presence of damped oscillatory tails on the lower CW state. Consequently, the interaction between fronts oscillates in sign and can lead to front locking, providing a mechanism for the stabilization of dissipative Kerr solitons [101,249–252]. Conversely, in the absence of oscillatory tails, only monotonic attraction occurs, preventing the formation of stable dissipative solitons. Thus, the stability properties are entirely dictated by the tail structure: two well separated vectorial fronts propagating in the cavity inevitably interact shown Fig. 26(a), as illustrated by the temporal evolution of the total intensity in the $\tau - t$ map of Fig. 26. Depending on the initial conditions, two distinct dark dissipative Kerr solitons can be generated, as illustrated in Fig. 26(b) and (c). The simplest solution, featuring a single intensity dip in the total field [see Fig. 26(b)]. In contrast, the vector dissipative shown in Fig. 26(b) exhibits a more complex profile, characterized by a small bump at the bottom of the dip. These two types of solutions can therefore coexist for the same parameter values [226]. We now turn to the tristable regime. The bifurcation diagram associated with these dark LSs corresponding to the configuration with two distinct hysteresis loops between the homogeneous steady states $CW1$, $CW2$, and $CW3$ shown in Fig. 27(a). The magnified views highlight two families of heteroclinic connections: one linking $CW1$ to $CW2$ (blue curve in Fig. 27(b)), and the other linking $CW2$ to $CW3$ (yellow curve in Fig. 27(c)). In this diagrams we plot the normalized L_2-norm $= \mathcal{N} = \int S_0/L \, d\tau$ with L the size of the system. This scenario corresponds to a collapsed heteroclinic snaking structure, a well-documented feature in far from equilibrium pattern forming systems [249,253,254]. In both cases, the branches of vectorial dissipative solitons exhibit oscillations of exponentially decreasing amplitude around the corresponding Maxwell point, ultimately terminating as they collapse onto it. In the scalar case, i.e., neglecting polarization effects, their collapse bifurcation diagram has been reported [252,255].

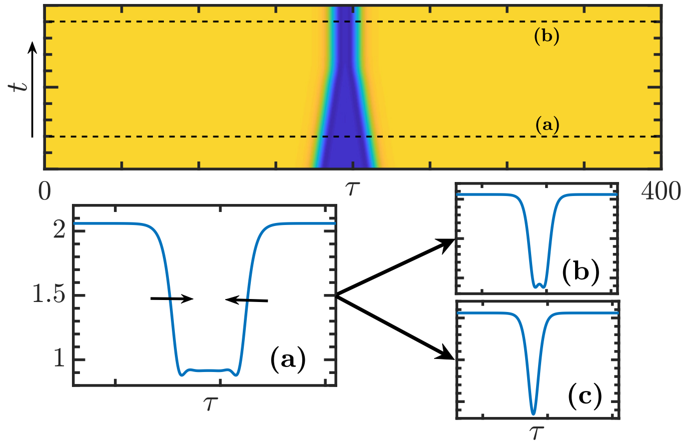

Fig. 26. Vectorial dark dissipative soliton resulting from fronts interaction. (a,b) Profiles of the two coexisting stable vectorial dark dissipative solitons, each exhibiting a different width, corresponding to the cross sections taken along the dashed lines indicated in the $\tau - t$ map. Numerical simulations of Eq. (49) are obtained for the parameters $E_i = 1.4675$, $\theta_x = 1.9$, and $\theta_y = 1.95$.
Source: Reproduced with permission from Ref. [226] @Copyright(2021) by Optica Publishing Group (Optica).

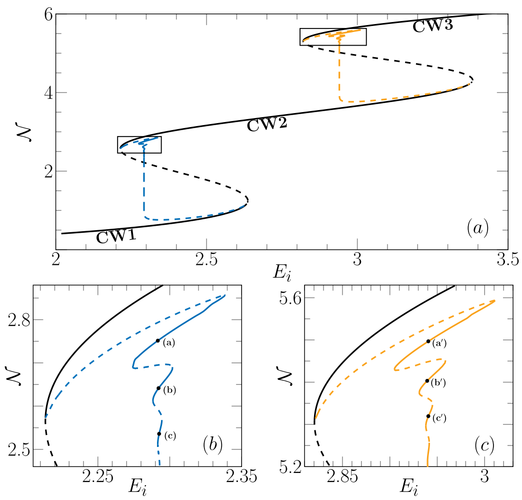

Fig. 27. Vectorial dark dissipative soliton resulting from fronts interaction. (a) Bifurcation diagram showing $\mathcal{N}$ as a function of the injected field intensity. (b,c) the magnified views highlight two families of heteroclinic connections shown in (a). Stable states are represented by solid lines, while unstable states are shown with dashed lines. Parameters are $\theta_x = 2.7$ and $\theta_y = 5$.
Source: Reproduced with permission from Ref. [227] @Copyright(2021) by the American Physical Society (APS).

The profiles of the Stokes parameters associated with points (a, b, c) and (a', b', c') indicated in Fig. 27(b,c) are shown in Fig. 28. Each turning point along the collapsed snaking branches marks a stability change, and each newly stabilized dissipative Kerr soliton acquires an additional bump at its edge, as illustrated by profiles (a, b, c) and (a', b', c'). Once the branch collapses onto the Maxwell point, the oscillatory behavior of the snaking structure disappears, and the internal shape of the solutions no longer evolves; only the width of the localized states continues to increase along the branch. This widening, clearly visible in the dissipative Kerr soliton profiles, reflects the progressive invasion of the system by the lower homogeneous state. At the end of the branch, the solution reconnects with the lower stable homogeneous steady states, corresponding to the complete invasion of the domain by the lower state. The bifurcation diagram corresponding to the tristable configuration with two overlapping hysteresis loops, shown in Fig. 29. In this regime, two distinct types of fronts may coexist for the same set of system parameters: those connecting $CW3$ to $CW3$, and those connecting $CW2$ to $CW1$. Consequently, the associated families of dark localized structures can also coexist. As in previous cases, each family forms a collapsed snaking bifurcation curve: the branch associated with the $CW3 \rightarrow CW2$ connection is shown in light orange, while the branch associated with the $CW2 \rightarrow CW1$ connection appears in blue. Unlike the previous tristable CW solutions, however, these two collapse snaking curves overlap over a finite interval of the injected field intensity, denoted by region C. The system can also sustain two distinct types of dissipative Kerr solitons, each characterized by its own collapsed snaking bifurcation. As before, these two families of LSs differ markedly in their peak intensities and

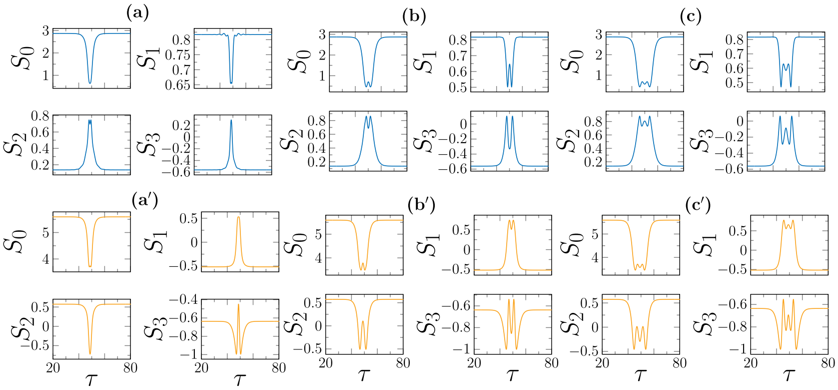

Fig. 28. Vectorial dark dissipative soliton resulting from fronts interaction. Profiles of the Stokes parameters as functions of the fast time τ for the stable LS solutions indicated in Fig. 27(b,c). Same parameters as in Fig. 27(b,c), and for the injected field amplitude (a) 2.2917 (b) 2.2922 (c) 2.2926 (a') 2.9394 (b') 2.9406 (c') 2.9406.
Source: Reproduced with permission from Ref. [227] @Copyright(2021) by the American Physical Society (APS).

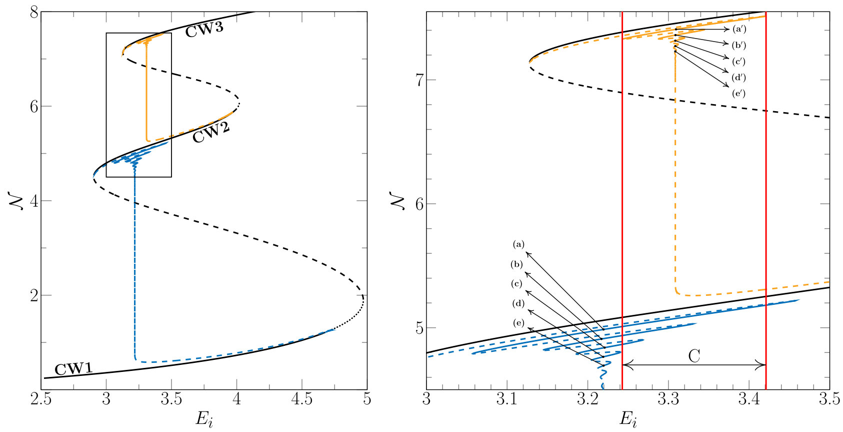

Fig. 29. Tristable heteroclinic snaking bifurcation diagram. Left panel: Bifurcation diagram showing the L_2-norm as a function of the injected field intensity E_i. Stable and unstable steady states are indicated by solid and dashed lines, respectively. The parameters are $\theta_x = 6.5$ and $\theta_y = 4.5$. Right panel: Enlarged view of the collapsed snaking branches associated with each bistability, highlighting the coexistence region C where the two families of solutions overlap.
Source: Reproduced with permission from Ref. [227] @Copyright(2021) by the American Physical Society (APS).

polarization properties. For appropriate values of the detuning parameters, the two collapse snaking branches of solutions exhibit an overlapping stability region, implying that both types of LSs may exist for the same set of system parameters, although not simultaneously within a single physical realization, since each LS type requires a different homogeneous background state [226].

These results provide new insights into the diversity and complexity of dissipative structures in driven resonators when polarization degrees of freedom are taken into account. More recently, vectorial solitons in Kerr Fabry-Pérot resonators with normal dispersion exhibit rich polarization dynamics enabled by nonlocal coupling [256]. This includes polarization symmetry breaking, self-organized dark soliton crystals, and the formation of stationary and dynamical vectorial dark-bright solitons. To achieve a more complete description, it is necessary to consider the influence of the group-velocity mismatch between the two polarization components. Although this effect was neglected in the present analysis, it can strongly modify the dynamics by inducing a drift of the LSs through the breaking of the $\tau \to -\tau$ reflection symmetry.

7. Spectral filtering effects on Kerr frequency combs

7.1. Spectral filtering in nonlinear Kerr resonators

We investigate the formation and dynamics of dissipative soliton Kerr frequency combs in the presence of temporal spectral filtering. The system under consideration is an optical resonator filled with a Kerr nonlinear medium and coherently driven by an external continuous wave field. In addition to the usual dispersion-nonlinearity balance, the

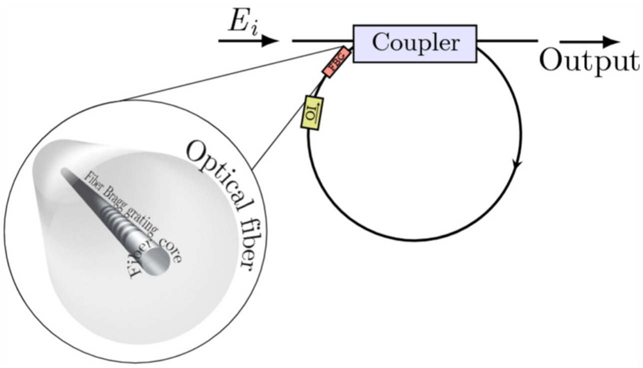

Fig. 30. Schematic representation of a driven ring resonator filled with Kerr media, equipped with a filter and excited by a coherent input field. BS denotes a beam splitter, and the arrows indicate the direction of light propagation.
Source: Reproduced with permission from Ref. [257] @Copyright(2025) by the American Physical Society (APS).

cavity incorporates a temporal filter acting on the intracavity field spectrum (see Fig. 30), thereby introducing a controlled frequency dependent loss mechanism. Starting from the infinite dimensional Ikeda map that describes the discrete round-trip evolution of the intracavity field, we derive an effective mean-field description that takes the form of a Lugiato–Lefever equation (LLE) modified to include spectral filtering effects. To further reduce the complexity of this generalized LLE, we employ a global perturbative approach based on multiple scale analysis. This asymptotic method enables the systematic elimination of higher-order contributions such as third-order dispersion and nonlinear convection terms under the assumption of smooth temporal variations and intensity based intracavity evolution. Within this regime of validity, the filtering operator not only modifies or renormalizes the coefficient of the second-order temporal derivative but also introduces a first-order derivative term with a purely imaginary coefficient, $i\alpha_1\partial_\tau$, with α_1 is real. This term represents a dissipative spectral shift mechanism imposed by the filter and plays a central role in soliton drift and spectral asymmetry. In the second part of the study, we analyze moving dissipative solitons emerging in the filtered Kerr cavity. These localized states possess broadband spectral signatures corresponding to frequency combs and exhibit nontrivial velocity dynamics induced by the interplay between dispersion, Kerr nonlinearity, and thereby inducing symmetry breaking.

7.2. Lugiato–Lefever model with spectral filtering

In the absence of diffraction, the nonlinear Schrödinger equation (Eq. (13)) describes light propagation along the optical fiber. Let us rewrite this equation as follows:

$$\frac{\partial F}{\partial z} = i\beta_2 \frac{\partial^2 F}{\partial \zeta^2} + i\gamma |F|^2 F, \tag{50}$$

where $F = F(z, \zeta)$ is the slowly varying electric field envelope, z is the longitudinal coordinate along the propagation light axis, and ζ is the time in a reference frame traveling at the group velocity of light within the Kerr material. This equation has to be supplemented by the following cavity boundary conditions:

$$F^{p+1}(0, \zeta) = \theta F_i + \rho \exp(i\phi) h(\zeta) \otimes F^p(l, \zeta), \tag{51}$$

where parameters ρ and θ are the amplitudes associated with the reflection and the transmission coefficients of the cavity beamsplitter, respectively. Eq. (51) establishes the iterative relation linking the intracavity field envelope F^{p+1}, evaluated at the cavity input after the $p+1$th round-trip, to the field $F^p(l, \zeta)$ at the cavity output after the pth pass, where l denotes the cavity length. The phase shift $\phi = 2\pi nl/\lambda_0$ accounts for the linear phase accumulated by the optical field during a single round-trip time t_r, with nnn the refractive index of the medium. Because this phase accumulation is large compared to the characteristic temporal variations of the envelope, the evolution of the intracavity field occurs on a timescale much slower than the round-trip time. In Eq. (51), the symbol $\otimes$ denotes the causal convolution between the impulse response function $h(\zeta)$ and the field F^p after p round-trips after. The convolution term $h(\zeta) \otimes F^p(t, \zeta)$ accounts for the spectral filtering induced by the Bragg reflector, with $h(\zeta)$ being a real valued impulse response characterizing the filter. This term therefore encapsulates the distributed frequency selective effects experienced by the intracavity field during each pass through the Bragg filter.

The nonlinear Schrödinger Eq. (50) supplemented by the cavity boundary conditions, Eq. (51), constitutes an infinite dimensional map. To make the theoretical treatment more manageable, the discrete round-trip map can be reformulated as a single integrodifferential equation. This simplification relies on considering high-finesse cavities, for which the transmission coefficient θ is assumed to be much smaller than one. In this case, the intracavity field experiences only minor changes during each round-trip of duration t_r. As a result, the field envelope may be viewed as evolving almost continuously on timescales much longer than t_r. This perspective allows the discrete index p to be replaced by a continuous slow time variable ttt when describing the field dynamics at the point $z = 0$. Following the same approach as in Section 3.2, we perform an averaging over a cavity length and by introducing continuous time and its derivative in the double limit of high finesse cavities $\theta \ll 1$ and small the linear phase shift $\phi \ll 1$, we obtain [257]

$$\begin{aligned} t_r\frac{\partial F}{\partial t} &= \theta F_i - F + \left(1-\frac{\theta^2}{2}-i\phi\right)\Big[h(\zeta)\otimes F \\ &+ \frac{i\beta_2 l}{2}h(\zeta)\otimes\frac{\partial^2 F}{\partial\zeta^2} + i\gamma l h(\zeta)\otimes|F|^2F\Big]. \end{aligned} \tag{52}$$

The last three terms in this integro-differential equation contains convolutions that requires to be evaluated. The first terms is $h(\zeta)\otimes F(t,\zeta) = \int_{-\infty}^{\zeta} h(\zeta')F(t,\zeta-\zeta')d\zeta'$. Then we extend in Taylor series $F(t,\zeta-\zeta')$ as

$$\begin{aligned} h(\zeta)\otimes F(t,\zeta) &= \int_{-\infty}^{\zeta} h(\zeta')\sum_{n=0}^{\infty}(-1)^n\frac{\zeta'^n}{n!}\frac{\partial^n F}{\partial\zeta^n}d\zeta', \\ &= \sum_{n=0}^{\infty} a_n\frac{\partial^n F}{\partial\zeta^n}, \end{aligned} \tag{53}$$

with

$$a_n(\zeta) = (-1)^n\int_{-\infty}^{\zeta} h_r(\zeta')\frac{\zeta'^n}{n!}d\zeta'. \tag{54}$$

These coefficient are well-defined for any function $h(\zeta)$ that decays faster than a polynomial. Under this approximation, we have

$$h(\zeta)\otimes F(t,\zeta) = a_0F + a_1\frac{\partial F}{\partial\zeta} + a_2\frac{\partial^2 F}{\partial\zeta^2} + \ldots \tag{55}$$

The two other contributions in the integro-differential Eq. (52) are evaluated similarly.

$$h(\zeta)\otimes\frac{\partial^2 F}{\partial\zeta^2} = c_0\frac{\partial^2 F}{\partial\zeta^2} + c_1\frac{\partial^3 F}{\partial\zeta^3} + \ldots, \tag{56}$$

$$h(\zeta)\otimes|F|^2F = d_0|F|^2F + d_1\frac{\partial|F|^2F}{\partial\zeta} + \ldots \tag{57}$$

We replace the three convolution terms Eqs. (55)–(57) in the integro-differential Eq. (52). We assume further that the filter bandwidth is large so that the coefficients $c_1 \ll 1$ and $d_1 \ll 1$. Under these approximations, we get [257]

$$\begin{aligned} t_r\frac{\partial F}{\partial t} &= \theta F_i - (1-a_0+\frac{\theta^2}{2}+i\phi a_0)F + i\gamma l d_0|F|^2F \\ &+ (1-\frac{\theta^2}{2}-i\phi)a_1\frac{\partial F}{\partial\zeta} + \left(a_2+\frac{i\beta_2 l c_0}{2}\right)\frac{\partial^2 F}{\partial\zeta^2} \end{aligned} \tag{58}$$

by using the following change of parameter and variables are and renormalization: $(E, E_i) = (F, \theta F_i)\gamma l d_0/(1-a_0)$, $t \equiv \kappa t/t_r$, $(\delta, \beta, \alpha_1, \alpha_2, v) = [2a_0\phi, \beta_2 l c_0, -2\phi a_1, a_2, 2(1-\theta^2/2)a_1/2\kappa]$, $\kappa = 1 - a_0 + \theta^2/2$, and $\tau = \zeta + vt$. Under these changes, the generalized LLE Eq. (58) takes its dimensionless form [257]

$$\begin{aligned} \partial_t E(t,\tau) &= E_i - (1+i\Delta)E + i|E|^2E \\ &+ i\alpha_1\frac{\partial E}{\partial\tau} + (\alpha_2+i\beta)\frac{\partial^2 E}{\partial\tau^2}, \end{aligned} \tag{59}$$

Incorporating the temporal or spatial filtering effects associated with gain dispersion and diffusion, respectively, into the modeling of a ring cavity filled with Kerr media requires going beyond the sole diffusive contribution $\alpha_2\partial_\tau$, as considered in Refs. [119,258–260]. In addition to this second-order term, one must also account for the first-order derivative $i\alpha_1\partial_\tau$, whose coefficient is purely imaginary. Note that the drift with the imaginary term cannot be trivially eliminated by changing the reference frame or renormalizing the wave number, particularly, as we will see, it plays a significant role in the dynamics of the system's dissipative solitons.

7.3. Drifting and breathing dissipative soliton combs

Before addressing the formation of dissipative Kerr solitons under the influence of spectral filtering, it is instructive to first examine the emergence of periodic patterns generated by modulational instability. We restrict our analysis to the monostable regime, in which the continuous-wave (CW) solution constitutes a single-valued response to the injected field.

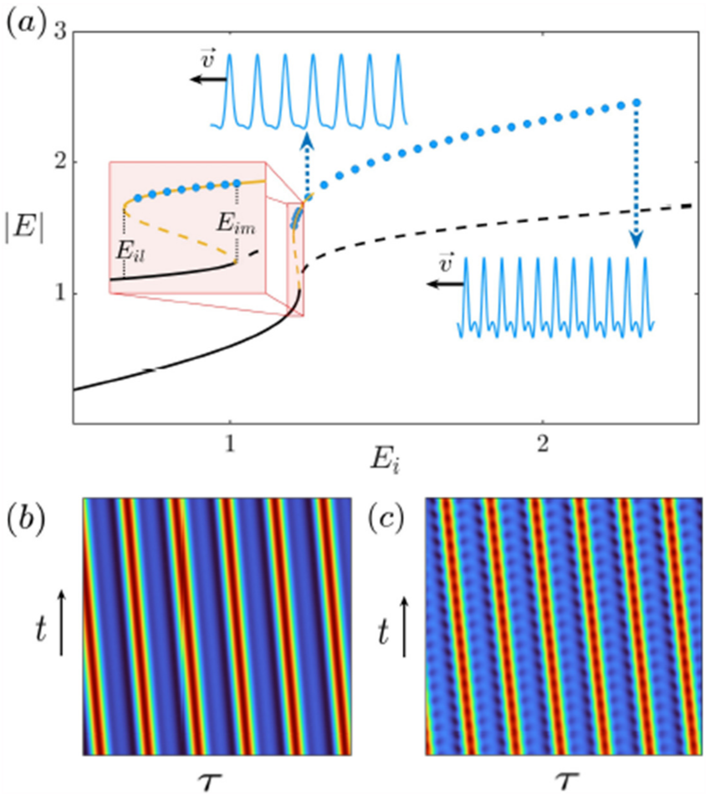

Fig. 31. Traveling periodic structures (a) Bifurcation diagram of the light intensity versus pumping.(a) Bifurcation diagram. The black curve shows the CW solutions, which become unstable for $E_i > E_{im}$ due to modulational instability. The blue dots indicate the maximum amplitude of the resulting moving periodic structures. The yellow branches, representing stable and unstable periodic solutions emerging from modulational instability, are obtained using the pseudo-arclength continuation method. (b) the $\tau - t$ map showing a traveling periodic solution obtained for $E_i = 2.3$. (c) Breathing traveling periodic solution obtained for $E_i = 2.39$. The temporal profiles of both solutions are shown in the inset of panel (a). Other parameters are $\Delta = 1.7$, $\beta = 1$, $\alpha_1 = 0.1$ and $\alpha_2 = 0.1$.
Source: Reproduced with permission from Ref. [257] @Copyright(2025) by the American Physical Society (APS).

This CW branch, represented by the black curve in Fig. 31, remains stable up to the threshold associated with the onset of modulational instability, denoted by E_{im}. Beyond this critical point, a standard linear stability analysis with respect to perturbations of finite frequency reveals that the CW state destabilizes and gives rise to moving periodic structures. A representative example of such a spatially extended pattern, which fills the entire optical cavity, is displayed in the $\tau - t$ map of Fig. 31(b). The numerical simulations are carried out by discretizing Eq. (59) on a grid of 512 points with a temporal resolution of $\Delta\tau = \Delta\tau = 0.1$. The temporal derivatives with respect to the retarded time τ are evaluated spectrally in order to ensure high accuracy, and the time evolution is computed using a fourth-order adaptive Runge–Kutta integration scheme. The temporal profile of the intracavity field corresponding to one of these solutions—propagating at a constant velocity $\mathbf{v}$ is shown above the map, illustrating the coherent drift of the pattern.

The dependence of the amplitude of these periodic traveling states on the injected field strength is presented in Fig. 31, highlighting their evolution as nonlinear solutions of Eq. (59). Importantly, these solutions cannot be stationary: they systematically exhibit a uniform translational motion. This drift is a direct consequence of the spectral filtering term $i\alpha_1\partial_\tau E$, which explicitly breaks the reflection symmetry $\tau \to -\tau$ of the governing equation. The symmetry breaking induced by this imaginary coefficient first-order derivative thus plays a central role in enabling and sustaining the propagation of periodic structures. Upon further increasing the injected field amplitude, the periodic solutions begin to exhibit breathing dynamics, as illustrated in Fig. 31(c). The results presented below describe the behaviors predicted from Eq. (59) within the strongly nonlinear regime where the modulational instability is subcritical and the CWs are monostable. As a consequence of the inversion (subcritical bifurcation) associated with MI, an hysteresis loop emerges in the range $E_{il} < E_i < E_{im}$, where stable CW state coexist with moving periodic structures. Beyond the periodic and continuous wave (CW) solutions that coexist in the interval $E_{il} < E_i < E_{im}$, an additional family of stable dissipative Kerr soliton emerges from the threshold associated with modulational instability. The maximum amplitudes of these dissipative solitons are shown for different values of the filter parameters α_1 and α_2. A pseudo-arclength continuation algorithm is used to compute the stable and unstable branches associated with modulational instability, while the blue dots correspond to direct numerical simulations of Eq. (59). The excellent agreement between the continuation results

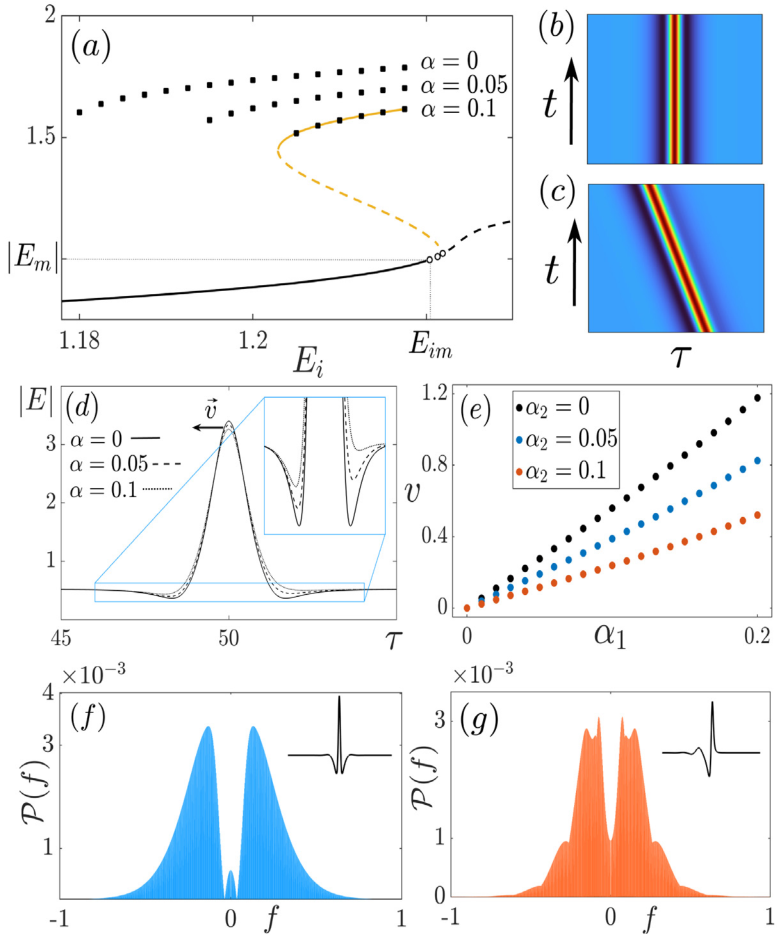

Fig. 32. Moving dissipative solitons obtained in the monostable case. (a) Their maximum amplitude as a function of the injected beam amplitude is shown by the three square marker curves, corresponding to different values of $\alpha = \alpha_1 = \alpha_2$. The black curve represents the CW solutions, with solid (dashed) lines indicating regions stable (unstable) with respect to modulational instability. The unstable and stable branches indicated by yellow color that emerge from the modulational instability of the periodic solutions are obtained using the pseudo-arclength continuation method. (b,c) (b), (c) $\tau - t$ maps associated with stationary and moving dissipative solitons obtained respectively for $\alpha_1 = 0$ and $\alpha_1 = 0.1$. Parameters are $E_i = 1.21$, and $\alpha_2 = 0.1$. (d) Magnified dissipative soliton profiles illustrating tail deformation induced by variations in the filter parameters. (e) Soliton velocity versus α 1 at a fixed injected field amplitude. (f,g) Combs corresponding to the stationary and moving dissipative solitons are shown in panels(b) and (c). Other parameters are $\delta = 1.7$, and $\beta = 1$.
Source: Reproduced with permission from Ref. [257] @Copyright(2025) by the American Physical Society (APS).

and the simulations confirms the accuracy of our approach for $\alpha = \alpha_1 = \alpha_2 = 0.1$. Examples of stationary and moving dissipative structures obtained from numerical simulations are illustrated in the $\tau - t$ maps in Fig. 32(b,c). In the absence of spectral filtering ($\alpha_1 = \alpha_2 = 0$), the dissipative solitons remain stationary and display symmetric profiles, as shown in Fig. 32(b). In contrast, when spectral filtering is introduced, the dissipative solitons begin to move with a constant velocity. Furthermore, the profile of the dissipative structures becomes asymmetric, as shown in Fig. 32(d). This deformation of the tail results from the drift induced by the purely imaginary coefficient $\alpha_1\, \partial_\tau E$, where α_1 is real. In contrast, a drift (or convection) associated with a real coefficient translates the dissipative structures without altering the shape of their tails, producing a pure translation rather than a deformation. To better characterize the soliton velocity, we evaluate the speed as a function of α_1 while varying α_2, as shown in Fig. 32(e). The spectral content of the dissipative solitons emerging from the resonator output forms an optical frequency comb, as illustrated in Eq. (59)(g) for $\alpha_1 = 0$ and in Eq. (59)(f) for $\alpha_1 \neq 0$. When the dissipative solitons remain stationary, the resulting combs are symmetric. In contrast, when the solitons exhibit motion, the corresponding combs become asymmetric. The comb lines remain evenly spaced in all cases, since the free spectral range set by the inverse of the cavity round-trip time has a fixed value.

To construct the bifurcation diagram associated with the formation of dissipative solitons, we use a pseudo-long arc continuation method that allows us to follow the branch of solutions through the fold points and also plot the unstable states without discontinuity [261]. The LLE model of Eq. (59) supports not only bound two peak states but also an infinite

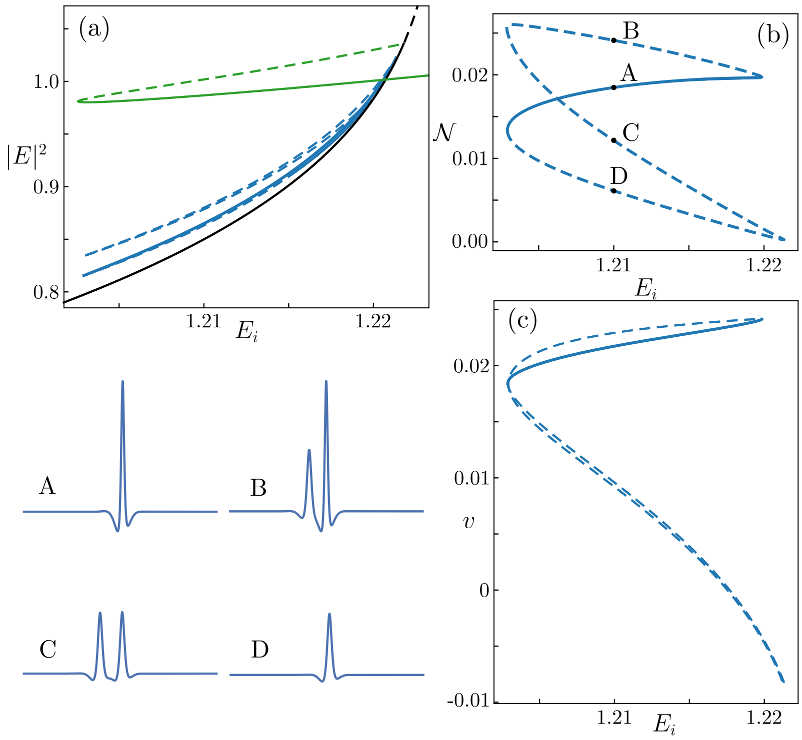

Fig. 33. Dissipative solitons isolas. (a) Bifurcation diagram showing the intensity of the intracavity field as a function of the injected field amplitude E_i. Black lines indicate the CWs, green lines indicate the intensity of moving periodic solutions, and blue lines indicate the one peak dissipative soliton. (b) L2-norm of the dissipative soliton branch as a function of the injected field amplitude. Insets A-D on the left show the profiles along the soliton branch. (c) Velocity of moving dissipative solitons isolas as a function of the injected field amplitude E_i. Full (dashed) lines correspond to stable (unstable) states, respectively. Parameters are $\delta = 1.7$, $\beta = 1$, and $\alpha_1 = \alpha_2 = \alpha = 0.1$.
Source: Reproduced with permission from Ref. [257] @Copyright(2025) by the American Physical Society (APS).

set of localized peaks [96,114]. For $\alpha_1 = 0$ and $\alpha_2 \neq 0$, Eq. (59) admits stationary solutions with odd and even numbers of localized peaks. In this regime, dissipative Kerr solitons undergo classical homoclinic snaking type of bifurcation. They correspond to the back-and-forth oscillations across the pinning region. This feature has been abundantly addressed for the Lugiato–Lefever model without spatial filtering [113,114]. Recently, it has been shown that when increasing the value of the coefficient α_2 of diffusive contribution, the stability domain associated with dissipative solitons shrinks and therefore reduces the size of the pinning region [257]. When $\alpha_1 \neq 0$, we construct the bifurcation diagram shown in Fig. 33(a), and we report the corresponding dissipative soliton speed in Fig. 33(b). The introduction of spectral filtering breaks the homoclinic snaking bifurcation structure, causing the system dynamics to organize instead into a sequence of isolas. An example of an isola associated with a single-peak dissipative soliton is presented in Fig. 33(c). On the left side of this figure, we show the soliton profile along the corresponding closed loop branch of dissipative soliton.

Similar closed loop branches of dissipative solitons, appearing in the form of isolas, have been reported when the stimulated Raman scattering is taken into account. This behavior arises because Raman scattering breaks the reflection symmetry of the system. The interplay between Raman scattering and Kerr nonlinearity is well established and has been documented across numerous experimental and theoretical studies [262–267]. Furthermore, a series of recent investigations has examined how stimulated Raman scattering, in conjunction with Kerr effects, shapes front dynamics and contributes to the stabilization of dissipative Kerr solitons in normal dispersion media [268–272]. This behavior is well established within dynamical systems theory and is formally designated as isolas [273–280]. In this configuration, the solutions connect only to four other asymmetric counterparts, forming a closed loop in the phase diagram typically resembling a Lissajous type curve (see Fig. 33).

In the bistable regime, $\delta > \sqrt{3}$, numerical simulations of Eq. (59) indicate that the introduction of spectral filtering substantially enlarges the stability domain of moving dissipative solitons. In particular, the onset of breathing dynamics is shifted to higher values of the injected field amplitude, demonstrating that spectral filtering stabilizes against oscillatory instabilities [257]. Moreover, the simulations reveal a wide variety of dynamical behaviors, including the emergence of moving bound states of dissipative solitons, in which two or more LSs propagate together while maintaining a fixed separation (see Fig. 34). Notably, we also observe moving breathing bound DSs, where the collective entity undergoes simultaneous translational motion and periodic oscillations in amplitude or width [257]. These findings highlight the

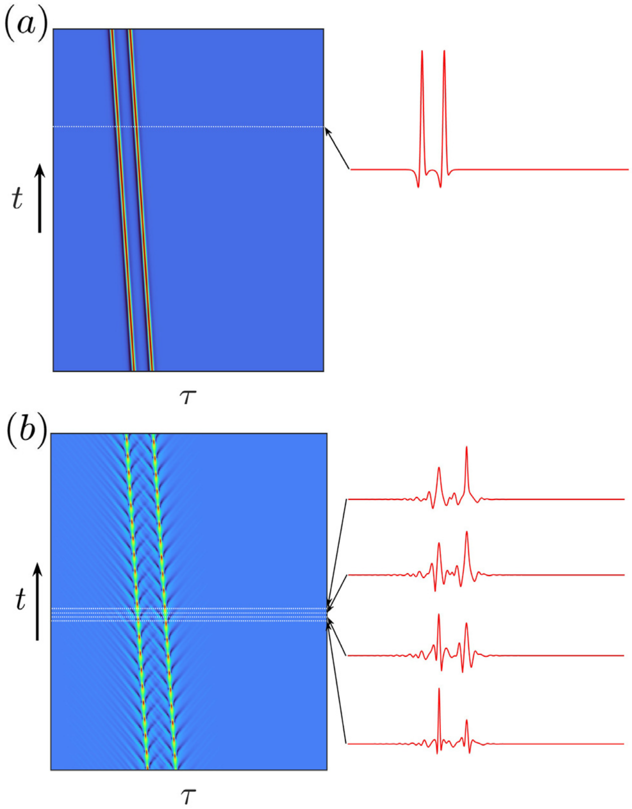

Fig. 34. Bounded dissipative solitons in the presence of spectral filtering. (a) Bounded moving dissipative solitons and (b) bounded moving and breathing dissipative solitons obtained for the same parameters.
Source: Reproduced with permission from Ref. [257] @Copyright(2025) by the American Physical Society (APS).

intricate interplay between spectral filtering, nonlinear interactions, and dispersion in shaping the stability and dynamical evolution of dissipative structures in the system.

Temporal spectral filtering introduces frequency-selective losses that damp high-frequency components of the intra-cavity field, thereby regularizing the waveform, delaying the onset of breathing or oscillatory instabilities, and enlarging the stability domain of stationary or steadily moving dissipative Kerr solitons. By reshaping the oscillatory tails of the solutions, filtering also alters soliton interactions enabling moving and moving breathing bound states and reorganizes the global bifurcation structure, notably breaking homoclinic snaking and giving rise to isolas when $\alpha_1 \neq 0$. In contrast, chromatic dispersion acts as a conservative phase mechanism, introducing frequency-dependent group delays that govern temporal pulse shaping. Taken together, dispersion determines how spectral components propagate, while spectral filtering selects which components persist, yielding a more controllable temporal profile and a tailored, often more symmetric, optical spectrum. Tail remodeling weakens (or strengthens) the effective forces between dissipative solitons, thereby allowing the formation of robust bound states that can be stationary, move uniformly, or be moving and breathing hybrids. Since the interaction is mediated by the overlap of oscillatory tails, even modest filtering can qualitatively alter the set of admissible bound separations and their stability, thereby enriching the observed multi-soliton configurations.

8. Raman-Kerr frequency combs in microresonators

8.1. Raman Kerr frequency combs in optical resonators

Macroscopic systems are commonly described using a reduced set of coarse-grained variables, an approach enabled by a separation of timescales between microscopic and macroscopic dynamics. In practice, this justifies a reduced description formulated in terms of slowly evolving macroscopic or coarse-grained variables [281]. When this separation is not well-defined, temporal correlations arise and give rise to delayed, nonlocal responses that can substantially alter the system's behavior. A classic example is the polarization or magnetization of a material under an external electric or magnetic field. In the linear regime, the polarization at time τ depends on the past history of the electric field according to $\mathbf{P}(\tau) = \int_{-\infty}^{\tau} \chi(\tau - \tau')\mathbf{E}(\tau')\,d\tau'$, where $\mathbf{E}$ is the electric field and $\chi(\tau)$ is the temporal susceptibility kernel encoding the delayed material response. When the characteristic frequency of the driving field is much smaller than the intrinsic charge dynamics, the delay can be neglected, and the response becomes effectively local and instantaneous.

It is instructive to contrast stimulated Raman scattering with the instantaneous Kerr nonlinearity, as both originate from the nonlinear response of matter to intense electromagnetic fields but have markedly different physical origins and dynamical consequences. The Kerr effect arises from the instantaneous electronic response of the medium to the applied optical field. On timescales relevant to optical propagation, the electronic polarization follows the field adiabatically, leading to an intensity-dependent refractive index. This response is effectively local in time and results in phenomena such as self-phase modulation and cross-phase modulation, without any intrinsic frequency preference or energy exchange between spectral components. As a consequence, Kerr nonlinearity is often regarded as conservative, preserving the symmetry of the optical spectrum. Stimulated Raman scattering, by contrast, stems from the interaction of light with vibrational (phononic) modes of the medium. These modes have finite response times, typically on the order of tens to hundreds of femtoseconds in amorphous materials such as silica. The Raman contribution, therefore, introduces a delayed nonlinear response, which crucially breaks the temporal reversibility of the Kerr dynamics. This delay enables a non-instantaneous transfer of energy from the optical field to the medium and back, favoring emission at lower (red-shifted) frequencies. From a physical perspective, while the Kerr effect modifies the optical phase through an intensity-dependent refractive index, SRS actively reshapes the optical spectrum by inducing a net frequency downshift. In driven-dissipative optical resonators, this distinction has profound implications. Whereas the Kerr nonlinearity alone supports stationary localized structures through a balance of dispersion, nonlinearity, driving, and loss, the presence of Raman scattering introduces an additional mechanism that continuously redistributes energy within the spectrum. This difference can be summarized as follows: the instantaneous Kerr effect preserves spectral symmetry and primarily affects the phase evolution of the intracavity field. Stimulated Raman scattering introduces a delayed, nonconservative response that breaks spectral symmetry and promotes energy transfer toward longer wavelengths.

The combined influence of Kerr and Raman scattering nonlinearities in both micro- and macro-resonators has attracted significant interest from both fundamental and applied perspectives. Numerous studies have explored soliton self-frequency shifts associated with frequency comb generation, as well as the formation of dissipative Kerr–Raman solitons in the anomalous dispersion regime [172,264,271,282–285]. More recently, theoretical and experimental studies investigate the impact of stimulated Raman scattering (SRS) on Kerr domain walls and dissipative Kerr solitons in all-fiber Kerr resonators under coherent optical injection [268–270,286–288].

8.2. Mean-field equation with spectral filtering

Prior to the advent of lasers, optical phenomena were almost entirely described within a linear theoretical framework, with only a few notable exceptions, such as Raman scattering. Consequently, nonlinear dynamical regimes were largely absent from conventional optical research. In this section, we analyze the formation of dissipative solitons resulting from the combined action of Kerr and Raman nonlinearities in a coherently driven micro-ring cavity, as schematically illustrated in Fig. 35. The dynamics of the intracavity electric field envelope are governed by the Lugiato–Lefever equation (LLE) [60], modified to account for the delayed nonlocal Raman response of the medium [282]

$$\begin{aligned}\frac{\partial E}{\partial \zeta} &= S-(1+i\Delta)E - ib_2\frac{\partial^2 E}{\partial T^2} + i\,(1-f_R)\,|E|^2\,E \\ &\quad + iaf_RE\int_{-\infty}^{T}\chi(T-T')|E(T')|^2dT'. \end{aligned} \tag{60}$$

Here $E = E(\zeta, T)$ is the normalized mean-field cavity electric field, Δ accounts for the normalized detuning parameter, and losses are normalized to unity. The time ζ is the slow time describing the evolution over successive round trips, and T is the fast time in the reference frame moving with the group velocity of the light within the cavity. S is the input field amplitude, and b_2 the second-order chromatic dispersion coefficient. The Raman is described by an integral whose strength is f_R and $a = \tau_0(\tau_1^2+\tau_2^2)/(\tau_1\tau_2^2)$. The delay kernel function $\chi(\tau)$ is

$$\chi(\tau) = \exp(-\tau_0\tau)/\tau_2\,\sin(\tau_0\tau/\tau_1), \tag{61}$$

with $\tau_0 = [|b_2L|/2\alpha_c]^{1/2}$, where α_c is the losses parameter. The choice of this Kernel, or influence function, has been proposed in [289,290], and shows an excellent agreement with experiments using standard fiber. In the absence of Raman effect, i.e., $f_R = 0$, fronts [165], motionless LS connecting HSS solutions, in which LSs move due to the third-order dispersion effect [117,280,291,292], have been reported.

8.3. Propagation of Kerr domain walls in the normal dispersion regime

In the normal dispersion regime, the effect of stimulated Raman scattering (SRS) on the dynamics of domain walls (DWs) and dissipative Kerr solitons has been extensively studied [268,269,271]. In particular, SRS has been shown to stabilize moving bright LSs that would otherwise be absent. Near the onset of bistability, DW interactions and the bifurcation structure of LSs can be described by a real order parameter equation [268,269]. However, this description

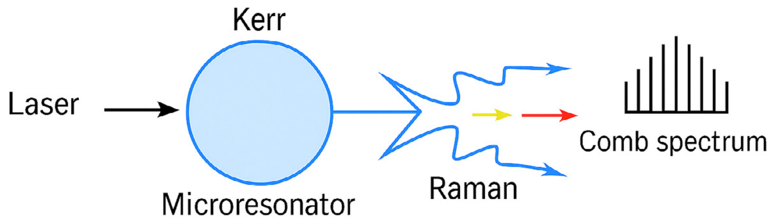

Fig. 35. Diagram showing the generation of a Raman–Kerr frequency comb in a microresonator driven by a continuous-wave (CW) laser. It highlights the Kerr and Raman nonlinear interactions within the cavity and the resulting comb spectrum.

is limited to that regime. To clarify the impact of SRS on the dynamics and bifurcation structure of DWs and DKSs over the full parameter space [270].

When the system operates close to the critical point associated with optical bistability. The coordinate of this point is given by (22). Starting from Eq. (60), the deviation $u \equiv E_r - E_{rc}$ of the electric field envelope from its value at the onset of bistability is shown to obey the generic bistable model [268]

$$\partial_t u = \eta + \mu u - u^3 + D\partial_{\tau\tau}u + \gamma\alpha \int_{-\infty}^{\tau} \chi(\tau - \tau')u(\tau')d\tau', \tag{62}$$

where $u = u(t, \tau)$ is a scalar order parameter, and the delay kernel function $\chi(\tau)$ is given by Eq. (61). In the limit of large τ_1 and τ, Eq. (61) can be approximated by an exponential $\chi(\tau) = e^{-\alpha(\tau-\tau')}$. The parameters $\alpha = \tau_0/\tau_2$ and $\gamma = 2\tau_1 f/(3\tau_2)$ account for the characteristic correlation time and the strength of the nonlocal delayed response, respectively. The above model corresponds to the universal model of bistability corresponding to the imperfect pitchfork bifurcation normal form, with a nonlocal coupling term that accounts for the Raman effect.

The homogeneous steady states solution u_0 of Eq. (62) satisfies $\eta = -(\mu + \gamma)u_0 + u_0^3$, which depends on the strength of time delayed nonlocal response, i.e., γ. In the bistable regime (i.e., for $\mu + \gamma > 0$) three solution branches u_b, u_m, and u_t coexist. The region of coexistence is limited by the folds or saddle–node bifurcations SN_b and SN_t occurring at $u_0^b = \sqrt{\mu + \gamma}/3$ and $u_0^t = -\sqrt{\mu + \gamma}/3$, respectively. In the absence of the Raman effect, Eq. (62) possesses a Lyapunov functional and at the Maxwell point, i.e., $\eta = 0$, Eq. (62) admits exact nonlinear front solutions

$$u_{\pm}(\tau) = \pm\sqrt{\mu}\tanh[\sqrt{\mu/2}(\tau - \tau_p)], \tag{63}$$

where

$$\tau_p \equiv \int_{-\infty}^{\infty} \tau\partial_\tau u_{\pm}(\tau)d\tau / \int_{-\infty}^{\infty} \partial_\tau u_{\pm}(\tau)d\tau \tag{64}$$

Owing to the Raman effect, well-separated fronts interact via the overlap of their tails. The Raman response profoundly alters this interaction, enabling the stabilization of traveling dissipative Kerr solitons such as those shown in Fig. 36, which are otherwise forbidden [268,269]. To analyze this interaction, we consider the regime close to the Maxwell point and assume that the fronts are sufficiently separated, that is,

$$u(t, \tau) = u_+(\tau - \Lambda + d/2) + u_-(\tau - \Lambda - d/2) - \sqrt{\mu} + w, \tag{65}$$

where $d = d(t)$ and $\Lambda = \Lambda(t)$ account for the width and centroid between well separated fronts ($d(t)\sqrt{\mu} \gg 1$) as indicated in Fig. 36.

To derive analytically the equation describing the interaction of fronts, we use the methods of bifurcation theory (see [268,269] for detailed calculations). We obtained first the equation describing the speed, often called the pulse centroid, given by

$$\dot{\Lambda} = v \equiv \frac{2\gamma\sqrt{\mu}}{\|T\|^2} \int_{-\infty}^{\infty} \partial_z u_+ e^{-\alpha|\tau|}d\tau, \tag{66}$$

where $\|T\|^2 \equiv \langle T|T\rangle$, with $|T\rangle \equiv \partial_z u_+ + \partial_z u_-$ is a translational mode (The Goldstein mode) associated with the linear ad self-adjoint operator $\mathcal{L} \equiv \mu - 3(u_+ + u_- - \sqrt{\mu})^2 + \partial_{zz}$. The integral in Eq. (66) does not depend on Λ, and therefore the pulse centroid moves with constant speed v. Numerical simulations show that the pulse spreads with constant speed, and confirm the validity of Eq. (66). Fig. 37(a) shows a comparison between the above formula and the numerical evolution of the pulse solution of model Eq. (62). Hence, we can conclude that the moving LS speed is well described by the expression (66).

Second, applying the solvability condition leads to the interaction law between fronts, given by

$$\dot{d} = a - be^{-2\sqrt{2\mu}d} + ce^{-\alpha d}, \tag{67}$$

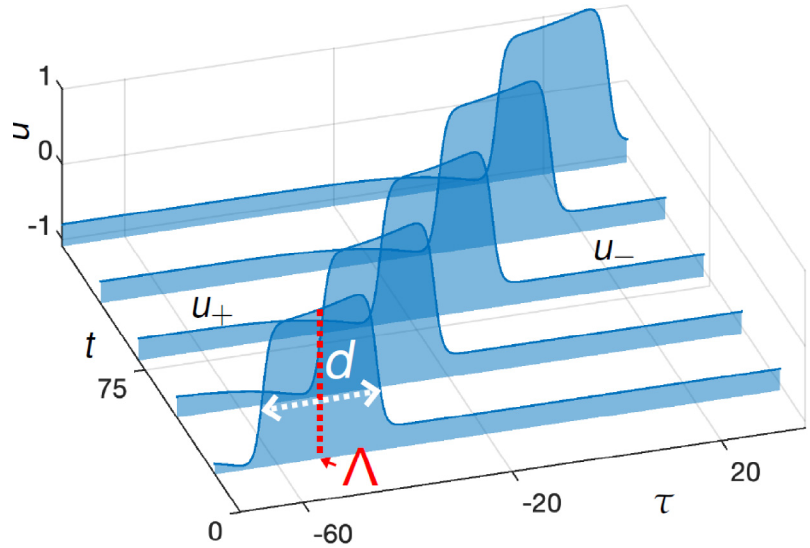

Fig. 36. Spatiotemporal evolution of the optical field envelope arising from nonlinear interaction between counter-propagating (or coexisting) fronts, illustrating the resulting pulse formation and propagation dynamics. Parameters are with $\gamma = -0.4$, $\alpha = 0.1$, $\mu = 1$, and $\eta = -0.03$.
Source: Reproduced with permission Ref. [257] @Copyright(2025) by the American Physical Society (APS).

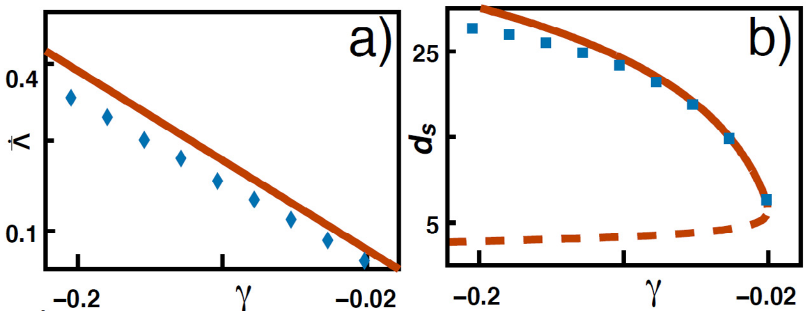

Fig. 37. Speed and the width of traveling dissipative Kerr solitons or domain-walls in the bistable system with Raman scattering, as described by Eq. (62). Dependence of the velocity and width of moving dissipative Kerr solitons on the nonlocal coupling strength ggg. The propagation speed (a) is shown by diamonds and a solid line corresponding to numerical results and analytical predictions from Eq. (66), respectively. The width (b) is indicated by square symbols and curves obtained from numerical simulations of Eq. (62) and from analytical formula Eq. (66). The parameters are $\alpha = 0.1$, $\mu = 1$, $D = 1$ and $\eta = -0.03$.
Source: Reproduced with permission from Ref. [268] @Copyright(2020) by the American Institute of Physics (AIP).

The explicit expressions of the coefficients a, b, and c are cumbersome and are therefore reported in Ref. [269]. The coefficients b and c are always positive, reflecting the system's intrinsic tendency toward equilibrium homogenization and the properties of the delayed nonlinear susceptibility. This kinetic Eq. (67) describing the evolution of the LS width d contains three contributions. The first term is a constant proportional to η, representing the energy difference between the two states. The second term accounts for the interaction between fronts through their tails and is always attractive since $b > 0$. The last term arises from the Raman effect and is always repulsive because $c > 0$.

Numerically, we characterized the pulse width and propagation speed, as summarized in Fig. 37. We find that the system admits two solutions, one stable and one unstable, created via a saddle–node bifurcation. To elucidate the origin of this instability, we numerically computed $\dot{d}$ as a function of the width d for fixed values of either η as shown in Fig. 38(a). The profiles of unstable and stable LSs, corresponding to large d_s and small d_u widths, are shown in Fig. 38(b) and (c), respectively. Fig. 38(a) were obtained both from direct simulations of the nonlocal bistable model (62) and from the reduced Eq. (67). The excellent agreement between these results supports the validity of the reduced description. From this viewpoint, moving LSs emerge through a saddle–node bifurcation. Despite the complexity of the nonlocal bistable model Eq. (62), the dynamics of moving LSs can be effectively captured by a simple set of coupled equations, Eqs. (66)

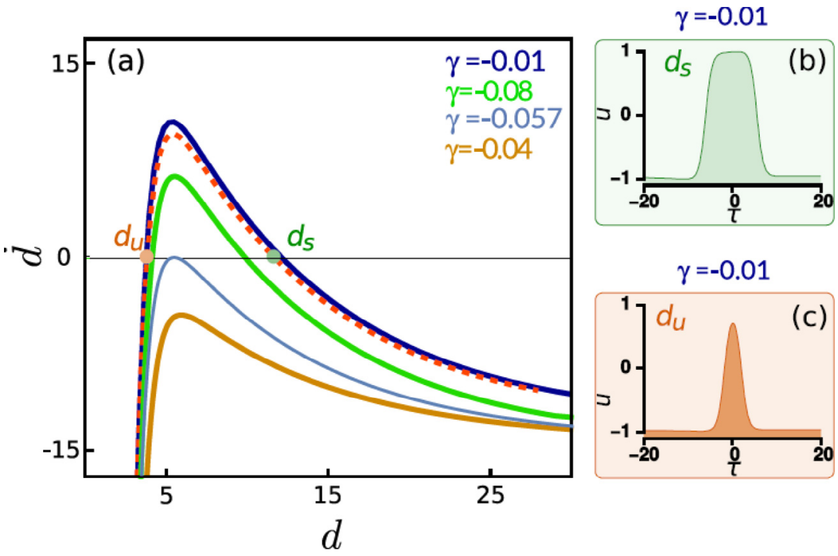

Fig. 38. Front interaction and stationary domain walls. (a) Dependence of the front interaction law given by Eq. (66) on the distance d between the cores of the two fronts for different values of γ. Stationary domain walls consist of unstable dissipative Kerr solitons with large width and stable dissipative Kerr solitons with small width, as illustrated in (b) and (c), respectively. The parameters are $\alpha = 0.1$, $\mu = D = 1.$, and $\eta = -0.03$.
Source: Reproduced with permission from Ref. [268] @Copyright(2020) by the American Institute of Physics (AIP).

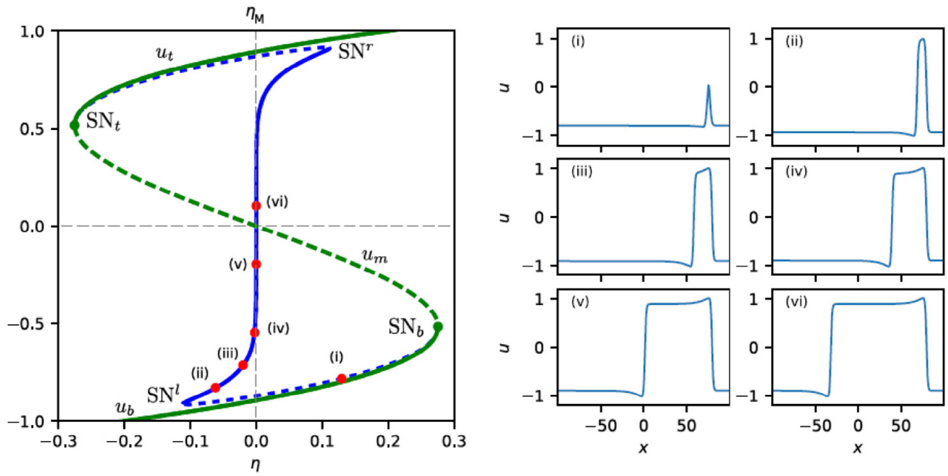

Fig. 39. Collapsed snaking bifurcation diagram. Green curves represent the homogeneous steady-state (HSS) solutions, while blue curves correspond to dissipative Kerr solitons or domain wall solutions of the generic bistable model with Raman scattering described by Eq. (62). Representative profiles of the domain wall solutions are indicated by labels (i)-(vi). Stable and unstable branches are shown with solid and dashed lines, respectively. $SN_{b,t}$ denotes the fold bifurcation of the HSS, whereas $SN^{l,r}$ indicates the saddle–node bifurcation of the LSs. The Maxwell point μ_M is marked by a dashed gray vertical line. Parameters are $\gamma = 0.2$, $\alpha = 0.1$, $mu = D = 1$, and $L = 100$.
Source: Reproduced with permission from Ref. [268] @Copyright(2020) by the American Institute of Physics (AIP).

and (67). We note that the front interaction description applies to coarse LSs and requires the condition $d(t)\sqrt{\mu} \gg d(t)$. The bifurcation diagram consists of a collapse snaking type of bifurcation discussed in Section 6.3.

The bifurcation diagram is constructed by introducing a reference frame moving at the velocity v of the dissipative Kerr solitons (DKS). Specifically, we apply the coordinate transformation $\tau \to x = \tau$ and impose the stationarity condition $\partial_t u = 0$ in Eq. (62). In this comoving frame, the dissipative Kerr soliton becomes stationary, which allows us to track its solutions numerically as a function of a chosen control parameter. The numerical continuation is performed using a predictor–corrector algorithm [293,294]. The results are shown in Fig. 39. We plot $\frac{1}{L}\int_{-L/2}^{L/2} u(x)dx$, where L denotes the system size, as a function of the control parameter η. The green curves denote the homogeneous steady states (HSSs) u_t, u_m, and u_b, with the stable and unstable branches shown as solid and dashed lines, respectively. The blue curves represent localized states, whose spatial profiles along the bifurcation diagram are shown in panels (i)-(vi).

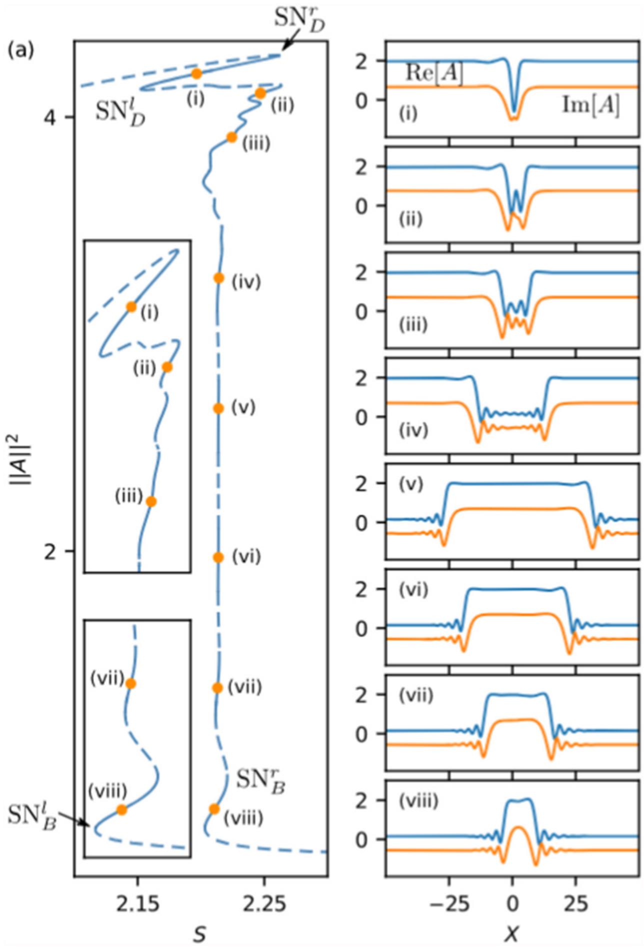

Fig. 40. Collapsed snaking bifurcation diagram. Temporal profiles associated with solution branches along the snaking curve are obtained for $\Delta = 4$. Labels (i)-(viii) denote the corresponding localized structures depicted on the right. Stable and unstable branches are represented by solid and dashed lines, respectively.
Source: Reproduced with permission from Ref. [270] @Copyright(2021) by the American Physical Society (APS).

The symmetry of the bifurcation diagram displayed in Fig. 39 arises from the invariance of Eq. (62) under the transformation $(\eta, u) \to -(\eta, u)$. A small-amplitude unstable localized state, arising from front interaction, emerges at the saddle–node bifurcation SN_b. As η decreases, its amplitude increases, and it becomes stable after crossing SN_l. Further increasing the control parameter η leads to the formation of a plateau corresponding to u_t. Beyond this point, the solution branch collapses near the Maxwell point η_M, where the localized state broadens and eventually fills the domain. The same scenario is then repeated for the inverted state $u \to -u$. This behavior, leading to the formation of localized states, is known as collapsed snaking and has been discussed in connection with vectorial localized states (see Section 6.3). This bifurcation scenario exhibits similarities with the collapsed snaking behavior reported in previous studies [252,252,295] where localized states possess damped oscillatory tails.

Having characterized the localized states arising from the interaction of fronts connecting two stable branches of the bistable response, we now employ a numerical continuation algorithm to construct the bifurcation diagram of the generalized Lugiato–Lefever equation (LLE), Eq. (60). This allows us to recover the collapsed snaking structure described above and previously obtained for the reduced generic bistable model, Eq. (62). We consider a detuning parameter $\Delta > \sqrt{3}$, ensuring that the system operates within the bistable regime and sufficiently far from any modulational instability. Continuation methods are then used to track the solution branches and determine their stability. The resulting bifurcation diagram is presented in Fig. 40 where we plot $\frac{1}{L}\int_{-L/2}^{L/2} |E(x)^2| dx$ where L denotes the system size and $x = \tau$, as a function of the injected field amplitude. We present only magnified views of the upper and lower regions of the bifurcation diagram, enabling clearer visualization of the organization of the solution branches. The upper portion of the diagram corresponds to branches associated with the dark dissipative Kerr solitons discussed in the previous subsection. These states develop asymmetric profiles, as illustrated in Fig. 40(i)–(iv). The irregular structure observed in this region suggests a more intricate front-locking mechanism than that described in the previous section.

9. Complex spatiotemporal behavior in passive resonators

9.1. Spatiotemporal chaos and turbulence-like behaviors

Out-of-equilibrium systems subjected to a permanent external driving are well known to undergo transitions toward self-organized stationary spatially periodic or localized patterns through symmetry-breaking instabilities [45,46,49]. As the control parameters are varied, these patterns undergo a series of transitions, evolving from simple stationary states to more complex dynamical regimes, including breathing localized structures, quasiperiodic states, and disordered structures [296–298]. Upon further increasing the driving strength, these systems may enter regimes of spatiotemporal complexity characterized by irregular dynamics and broadband spatial and temporal spectra [299–301]. The characterization of these complex dynamical states often relies on diagnostic tools such as power spectral analysis, filtered spatiotemporal visualizations, phase-space reconstruction techniques, embedding-dimension estimators, and time-series analysis. Although these methods provide valuable information about the underlying dynamics, they are often unable to unambiguously discriminate among different forms of complex behavior, such as spatiotemporal chaos [299–301]. A more rigorous classification requires considering the spectral properties of Lyapunov exponents and the statistical features of the dynamics [301].

Low dimension or temporal chaos occurs in systems whose state variables depend only on time and can be described by a finite number of degrees of freedom. In such systems, chaos manifests itself through irregular temporal oscillations and unpredictable trajectories in phase space. Despite their complexity, the dynamics remain spatially uniform, and the analysis focuses primarily on the evolution of a small set of interacting variables. Temporal chaos has been extensively studied in nonlinear oscillators, electronic circuits, and population dynamics, providing fundamental insights into the mechanisms responsible for deterministic unpredictability [302,303].

Many natural and engineered systems, however, are spatially extended and cannot be adequately described solely through temporal dynamics. Their state depends on both space and time, leading to the emergence of complex patterns that evolve continuously throughout the system. Such systems are often modeled by partial differential equations, coupled map lattices [302,303], or networks of interacting units [304]. Examples include fluid turbulence, reaction–diffusion systems, plasmas, nonlinear optical resonators, ecosystems, and neural tissues. The interaction of nonlinear processes with spatial and temporal coupling mechanisms, such as diffraction, diffusion, and convection, generates a rich diversity of spatiotemporal dynamics, encompassing coherent structures, traveling waves, pattern formation, and complex states.

In particular, spatiotemporal chaos is typically characterized by an extensive set of positive Lyapunov exponents, yielding a continuous Lyapunov spectrum that reflects the high-dimensional nature of the underlying instability. In contrast, low-dimensional chaos is associated with only a finite number of positive Lyapunov exponents. Turbulence and weak turbulence, however, are fundamentally different phenomena, being governed by cascade mechanisms that often manifest through power-law scaling of conserved quantities, such as energy or optical intensity.

Such complex dynamical behaviors, including turbulence-like states, are encountered in a wide range of driven dissipative systems across physics, chemistry, biology, and active matter. Such spatiotemporal dynamics have been observed in a wide variety of physical, biological, and environmental systems, including fluid convection [305], atmospheric, oceanic, and biological processes [306–309]. Similar phenomena have subsequently been reported in numerous other contexts, such as fiber lasers [310–312], nonlinear optical systems [313,314], active matter [315,316], chemical reaction systems [317], and Bose–Einstein condensates [318]. These studies highlight the ubiquitous nature of complex spatiotemporal behavior across diverse disciplines.

Turbulence-like behavior refers to complex, irregular, and multiscale dynamics that occur in a wide range of nonlinear spatially extended systems, not only in fluids. Although these systems can display features reminiscent of fluid turbulence, such as chaotic fluctuations and broad spectral distributions, their underlying mechanisms are fundamentally different. While classical fluid turbulence arises from the nonlinear advection term of the Navier–Stokes equations and involves an energy cascade across scales, turbulence-like spatiotemporal chaos generally emerges from nonlinear local interactions combined with diffusion, dispersion, or coupling between neighboring elements. As a result, a direct analog of the fluid energy cascade may not exist in these systems.

An intriguing manifestation of complex spatiotemporal dynamics in nonlinear photonic systems is the emergence of chimera states. The emergence of chimera states, characterized by the coexistence of spatially synchronized and desynchronized regions. In arrays of coupled waveguide resonators driven by coherent optical injection, the interplay between Kerr nonlinearity, diffraction, dissipation, and discrete coupling can lead to the formation of localized chaotic structures embedded in a coherent background [319]. These optical chimeras constitute a striking example of partial synchronization, where order and disorder coexist in a self-organized manner. Remarkably, the discrete nature of coupled resonator arrays stabilizes chimera-like states that are absent or unstable in their continuous counterparts. The concept has been extended to two-dimensional lattices of coupled waveguide resonators, where a rich variety of spatiotemporally chaotic, localized states and their interactions have been predicted [320].

In the field of nonlinear optics, such complex behaviors have recently attracted significant attention, particularly in optical frequency comb microresonators and coherently driven fiber cavities with Kerr nonlinearities. Experimental studies, supported by numerical simulations, have revealed the emergence of rich dynamical regimes in systems such as whispering-gallery-mode microresonators and all-fiber cavities [146,321–324]. These regimes encompass a wide variety of phenomena, ranging from stable dissipative structures to strongly irregular spatiotemporal dynamics.

9.2. Spatiotemporal chaos

Chaos theory studies deterministic dynamical systems whose long-term behavior is highly sensitive to initial conditions. Although the governing equations are deterministic, meaning that the future evolution of the system is fully determined by its current state, even infinitesimally small differences in initial conditions can lead to drastically different outcomes over time. This phenomenon describes how small, seemingly insignificant changes in initial conditions can lead to drastic, unpredictable consequences in a complex system. Classic examples of chaotic systems include the Lorenz model and Rössler oscillator, whose dynamics evolve on strange attractors in finite-dimensional phase spaces. The characterization of chaos relies on concepts such as Lyapunov exponents, fractal dimensions, and attractor theory, which quantify the degree of unpredictability and complexity of the underlying dynamics.

The study of spatio-temporal chaos combines methods from nonlinear dynamics, statistical physics, and pattern formation theory to understand the mechanisms governing the emergence and evolution of complex patterns. Important tools include Lyapunov spectra, entropy measures, correlation functions, spectral analysis, and fractal dimension estimators such as the Kaplan–Yorke dimension. These approaches provide quantitative measures of complexity, predictability, and the number of active degrees of freedom involved in the dynamics. Understanding spatio-temporal chaos is essential for describing and controlling a wide range of phenomena in nature and technology, where disorder and coherence coexist across multiple spatial and temporal scales.

Lyapunov exponents are fundamental tools for characterizing the stability and predictability of dynamical systems. They quantify how rapidly two trajectories that start from infinitesimally close initial conditions diverge or converge as time evolves. Consider a small perturbation $\delta\psi$ applied to an initial state. Its evolution can be approximated as $\approx \delta\psi e^{\lambda t}$, where λ is the Lyapunov exponent. The sign of λ determines the nature of the dynamics. If $\lambda > 0$, perturbations grow exponentially, revealing exponential sensitivity to initial conditions and the presence of chaos. For systems with many degrees of freedom, there exists a Lyapunov spectrum $\lambda_1 \geq \lambda_2 \geq \cdots \geq \lambda_N$, which contains all Lyapunov exponents of the system. The largest exponent, λ_1, is particularly important because a positive largest Lyapunov exponent is a signature of chaotic behavior. In spatially extended systems exhibiting spatiotemporal chaos, the complete Lyapunov spectrum provides more information than the largest exponent alone. It allows us to estimate the dimension of the strange attractor through the Kaplan–Yorke dimension (D_{KY}). One of the key properties of the Lyapunov spectrum is its extensivity, meaning that it scales linearly with the physical size of the system. As a result, the Kaplan–Yorke dimension, which represents an upper bound for the dimension of the strange attractor in spatiotemporal chaotic systems, is itself an extensive quantity that increases with system size [325]. Since the D_{KY} quantifies the complexity of the strange attractor, it is commonly used as a measure of the system's dynamical complexity. The Kaplan–Yorke dimension is defined as [326]

$$D_{KY} = p + \frac{\sum_{i=1}^{p} \lambda_i}{\left|\lambda_{p+1}\right|}, \tag{68}$$

The integer p denotes the largest number of Lyapunov exponents whose cumulative sum remains positive, i.e., $\sum_{i=1}^{p} \lambda_i > 0$. Physically, p represents the number of phase-space directions that contribute to a net expansion of nearby trajectories. The Kaplan–Yorke dimension is obtained by interpolating between the pth and $(p+1)$th dimensions, where the cumulative Lyapunov sum changes sign, thereby providing an estimate of the fractal dimension of the strange attractor.

We consider the LLE in the form of $\partial\psi_t = S - (\alpha + i\delta)\psi + i/2\partial_\tau^2\psi + i|\psi|^2\psi$ where ψ represents the normalized slowly varying envelope of the field circulating within the cavity, while S is the real-valued constant driving amplitude. The parameters δ and α correspond to the cavity detuning and losses, respectively. The only difference with respect to the LLE (Eq. (8)) is that the cavity losses are not normalized to unity. This distinction does not affect the results when $\alpha \leq 1$. The temporal evolution of the intracavity intensity, plotted as a function of the fast time t, is shown in Fig. 41(a). The dynamics consist of randomly distributed localized peaks with large amplitudes, revealing a complex and seemingly chaotic behavior. This complexity is quantified through the calculation of the Lyapunov exponents, whose spectrum is presented in Fig. 41(b). Fig. 41(c) shows the dependence of the Kaplan–Yorke dimension, D_{KY}, on the number of discretization points. The results reveal a clear linear increase of D_{KY} with system size, demonstrating the extensive nature of the chaotic dynamics. This scaling indicates that the dimension of the strange attractor grows proportionally to the system size, implying that the complexity of the underlying spatiotemporal chaos increases extensively as the spatial extent of the system is enlarged.

Fig. 41(c) was obtained for a fixed value of the injected field intensity. To further characterize the spatiotemporal chaotic regime, we present the Kaplan–Yorke dimension as a function of the injected field intensity as shown in Fig. 42. The insets display the Lyapunov spectra corresponding to four representative values of the pumping intensity, denoted by Γ_j with $j = (1, 2, 3, 4)$. The system is discretized using 512 grid points, and each spectrum consists of $N = 496$ Lyapunov exponents. As the pump intensity is increased, the homogeneous steady state (HSS) remains stable, with a Yorke–Kaplan dimension $D_{KY} = 0$, up to the critical value S_2^+. Beyond this threshold ($S_2 > S_2^+$), the system undergoes a transition to a spatiotemporal chaotic regime, characterized by a positive Kaplan–Yorke dimension ($D_{KY} > 0$). This behavior persists over a broad range of pump intensities. Conversely, when S is decreased, the spatiotemporal chaotic state remains stable down to a lower threshold, S_2^-, as illustrated in Fig. 42. The resulting hysteresis loop reveals the coexistence of three distinct dynamical states, namely spatiotemporal chaos, pulsating localized structures, and the homogeneous steady state, within the interval $S_2^- < S_2 < S_2^+$. The inset in Fig. 42 presents the Lyapunov spectra for several values of the pump

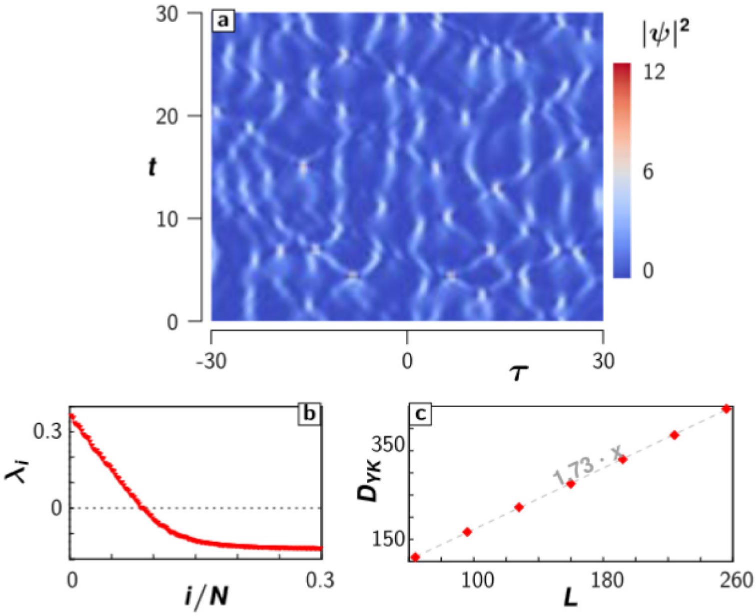

Fig. 41. Characterization of Spatiotemporal Chaos (a) $t-\tau$ map showing complex spatiotemporal dynamics obtained from numerical simulations of the LLE (b) Lyapunov spectrum. (c) Dependence of the Kaplan–Yorke dimension D_{KY} on the system size L. The parameter are $\delta = 1$, $\alpha = 0.16$, and $S = 0.4$.
Source: Reproduced with permission Ref. [221] @Copyright(2017) by Optica Publishing Group (Optica).

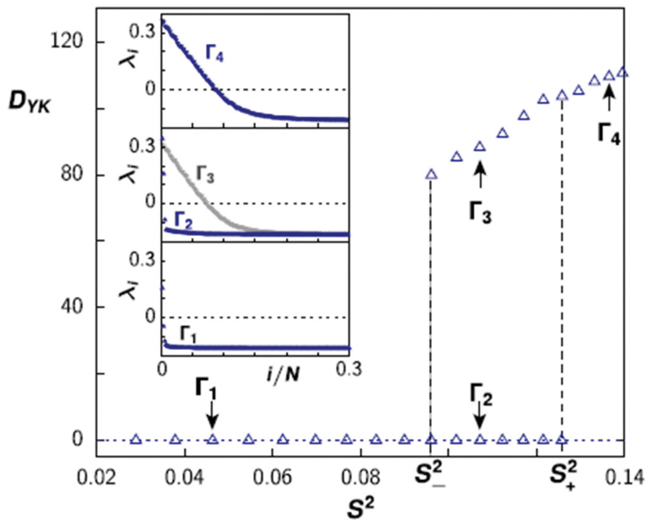

Fig. 42. Diagram showing the Kaplan–Yorke dimension as a function of the injected field intensity. The parameter are $\delta = 1$ and $\alpha = 0.16$.
Source: Reproduced with permission Ref. [221] @Copyright(2017) by Optica Publishing Group (Optica).

intensity. Notably, the middle panel displays two distinct spectra, corresponding to Γ_2 and Γ_3, obtained for identical parameter values. This clearly demonstrates the coexistence of two qualitatively different dynamical regimes under the same operating conditions.

Although the terms turbulence-like behavior and classical turbulence are often used interchangeably, they describe phenomena that share many qualitative features yet differ in their physical origins, governing equations, and interpretations. Classical turbulence is a specific physical phenomenon that occurs in fluid flows at sufficiently high Reynolds numbers. It is governed by the Navier–Stokes equations and is characterized by irregular velocity fluctuations, vortex stretching, energy cascades, and a broad spectrum of interacting spatial and temporal scales. In fluid turbulence, kinetic energy is typically injected at large scales, transferred through an inertial range to progressively smaller scales, and ultimately dissipated by viscosity at the smallest scales. In contrast, turbulence-like behavior is a more general concept used to describe irregular, disordered, and multiscale dynamics observed in nonlinear spatially extended systems that are not necessarily fluids. Examples include reaction–diffusion systems, chemical oscillators, nonlinear optical media, plasmas, and neural networks. These systems may exhibit complex dynamics that resemble fluid turbulence, such as chaotic fluctuations, defect proliferation, and broad-band spectra even though they are governed by fundamentally different equations and physical mechanisms.

10. Conclusions and perspectives

Light confinement and nonlinear photonics together form the physical basis of modern frequency comb technologies. Over the past two decades, advances in artificial photonic structures (high-Q microresonators, dispersion-matched waveguides, and compatible integrated platforms) have transformed nonlinear processes previously confined to the laboratory into compact, energy-efficient, and scalable devices. This study has highlighted how these developments enable efficient four-wave mixing, parametric oscillation, and, most importantly, the formation of dissipative Kerr solitons. The latter have emerged as a unifying mechanism linking light confinement, nonlinear cavity dynamics, and the generation of coherent optical frequency combs.

The Lugiato–Lefever equation and its extensions provide a powerful theoretical framework for understanding the rich nonlinear dynamics of passive optical resonators and the formation of optical frequency combs. This mean-field description captures a broad hierarchy of dynamical regimes, ranging from modulation instability and Turing patterns to dissipative solitons, multi-soliton states, front propagation, and complex spatiotemporal behaviors. Beyond the standard Kerr cavity model, we have reviewed the influence of several important physical effects, including polarization degrees of freedom leading to vector dissipative solitons, Raman scattering and Raman–Kerr comb generation, spectral filtering, spatially inhomogeneous pumping, and delayed-feedback control. These mechanisms enrich the landscape of localized and extended structures, providing new routes for controlling soliton formation, stability, motion, and interactions. We have also highlighted the emergence of complex dynamics, including breathing states, drifting solitons, and spatiotemporal chaos, revealing deep connections between nonlinear dynamics, symmetry breaking, self-organization, and front propagation in driven-dissipative optical systems. The resulting frequency combs combine high coherence, low timing jitter, and broad spectral coverage, paving the way for applications in precision metrology, spectroscopy, coherent communications, microwave photonics, and emerging quantum technologies. As advances in material platforms, dispersion engineering, and integrated photonics continue to accelerate, dissipative solitons and Kerr frequency combs are expected to remain at the forefront of both fundamental research and next-generation photonic technologies.

Using rigorous tools from dynamical systems theory, particularly Lyapunov spectra, we demonstrate that the complex dynamics observed in driven optical systems are manifestations of spatiotemporal chaos. The Kaplan–Yorke dimension is shown to be an effective order parameter for characterizing the bifurcation structure associated with this chaotic regime. Our analysis also reveals the coexistence of spatiotemporal chaos, self-pulsating dissipative Kerr solitons, and homogeneous steady states. These complex states exhibit strong sensitivity to initial conditions, high-dimensional chaotic dynamics, and exponential power spectra, distinguishing them from turbulence-like regimes. These findings provide a useful framework for the identification and classification of complex spatiotemporal behaviors in dissipative systems.

While Kerr microcombs have matured rapidly, mode-locked lasers continue to provide a complementary and indispensable platform, offering high pulse energies, broad tunability, and a wide variety of soliton states. The interaction between propagation-based and cavity-based soliton physics enriches our understanding of nonlinear wave dynamics and broadens the design space for next-generation comb sources. Looking ahead, several challenges and opportunities remain. Improving the robustness of soliton initiation, long-term stabilization under realistic operating conditions, and extending spectral coverage through hybrid and dispersion-controlled material platforms are active areas of research. Equally promising are enhanced quantum microcombs, chip-scale self-referenced systems, and architectures that couple resonators, waveguides, and heterogeneous materials to push frequency combs further into integrated photonics. In summary, the convergence between powerful light confinement and nonlinear optical physics has redefined the landscape of frequency comb generation. The synergy between theory, materials, and device engineering continues to drive rapid progress, bringing us closer to fully integrated, low-power, and widely deployable frequency comb sources. As these technologies evolve, they are poised to play a central role not only in precision measurements, but also in emerging fields such as quantum information, neuromorphic photonics, biomedical sensing, and next-generation communication systems.

CRediT authorship contribution statement

Mustapha Tlidi: Conceptualization, Formal analysis, Investigation, Supervision, Writing – original draft, Writing – review & editing. **Marcel G. Clerc:** Conceptualization, Formal analysis, Writing – review & editing. **Stefano Boccaletti:** Conceptualization, Funding acquisition, Writing – review & editing.

Compliance with ethics requirements

This article does not contain any studies with human or animal subjects.

Declaration of competing interest

The authors declare that they have no known competing financial interests or personal relationships that could have appeared to influence the work reported in this paper.

Acknowledgments

M.T. is a Research Director at the Fonds National de la Recherche Scientifique (FNRS, Belgium). M.C. gratefully acknowledges financial support from the ANID Millennium Science Initiative Program, Grant ICN17-012 (MIRO) and FONDECYT project 1260307. S.B. acknowledges support from the Italian PRIN Project No. 2022FHHHPC, entitled "The Structure, Dynamics and Control of Network Systems with Higher-Order Interactions".

References

[1] Robert W. Boyd, Nonlinear Optics, fourth ed., Academic Press, 2020.
[2] Govind P. Agrawal, Nonlinear Fiber Optics, sixth ed., Academic Press, 2019.
[3] Kerry J. Vahala, Optical microcavities, Nature 424 (2003) 839–846.
[4] David R. Carlson, Daniel D. Hickstein, et al., Self-referenced frequency combs using high-efficiency silicon-nitride waveguides, Opt. Lett. 42 (12) (2017) 2314–2317.
[5] Tobias J. Kippenberg, Alexander L. Gaeta, Michal Lipson, Michael L. Gorodetsky, Dissipative Kerr solitons in optical microresonators, Science 361 (2018) eaan8083.
[6] Thomas Udem, Ronald Holzwarth, Theodor W. Hänsch, Optical frequency metrology, Nature 416 (2002) 233–237.
[7] Philippe Grelu, Nail Akhmediev, Dissipative solitons for mode-locked lasers, Nat. Photon. 6 (2) (2012) 84–92.
[8] Pascal Del'Haye, Albert Schliesser, Olivier Arcizet, Tobias Wilken, Ronald Holzwarth, Tobias J. Kippenberg, Optical frequency comb generation from a monolithic microresonator, Nature 450 (2007) 1214–1217.
[9] Pablo Marin-Palomo, et al., Microresonator-based solitons for massively parallel coherent optical communications, Nature 546 (2017) 274–279.
[10] Tobias Herr, Victor Brasch, et al., Temporal solitons in optical microresonators, Nat. Photon. 8 (2014) 145–152.
[11] David T. Spencer, et al., An optical-frequency synthesizer using integrated photonics, Nature 557 (2018) 81–85.
[12] Myoung-Gyun Suh, Kerry J. Vahala, Soliton microcomb range measurement, Science 359 (2018) 884–887.
[13] P. Del'Haye, T. Herr, E. Gavartin, M.L. Gorodetsky, R. Holzwarth, T.J. Kippenberg, Octave spanning tunable frequency comb from a microresonator, Phys. Rev. Lett. 107 (2011) 063901.
[14] L.A. Lugiato, F. Castelli, Quantum noise reduction in a spatial dissipative structure, Phys. Rev. Lett. 68 (22) (1992) 3284.
[15] Avik Dutt, Kevin Luke, Sasikanth Manipatruni, Alexander L Gaeta, Paulo Nussenzveig, Michal Lipson, On-chip optical squeezing, Phys. Rev. Appl. 3 (4) (2015) 044005.
[16] J. Ye, H. Schnatz, L.W. Hollberg, Optical frequency combs: From frequency metrology to optical phase control, IEEE J. Sel. Top. Quantum Electron. 9 (4) (2003) 1041–1058.
[17] J.L. Hall, Nobel lecture: Defining and measuring optical frequencies, Rev. Modern Phys. 78 (2006) 1279–1295.
[18] P.J. Delfyett, S. Gee, M.-T. Choi, H. Izadpanah, W. Lee, S. Ozharar, F. Quinlan, T. Yilmaz, Optical frequency combs from semiconductor lasers and applications in ultrawideband signal processing and communications, J. Lightwave Technol. 24 (2006) 2701.
[19] T. Herr, V. Brasch, J.D. Jost, C.Y. Wang, N.M. Kondratiev, M.L. Gorodetsky, T.J. Kippenberg, Temporal solitons in optical microresonators, Nat. Photon. 8 (2014) 145.
[20] T. Hansson, S. Wabnitz, Dynamics of microresonator frequency comb generation: Models and stability, Nanophotonics 5 (2016) 231.
[21] Y.K. Chembo, Kerr optical frequency combs: Theory, applications and perspectives, Nanophotonics 5 (2016) 214.
[22] T. Fortier, E. Baumann, 20 years of developments in optical frequency comb technology and applications, Commun. Phys. 2 (2019) 153.
[23] A. Pasquazi, M. Peccianti, L. Razzari, D.J. Moss, S. Coen, M. Erkintalo, Y.K. Chembo, T. Hansson, S. Wabnitz, P. Del'Haye, X. Xue, A.M. Weiner, R. Morandotti, Micro-combs: A novel generation of optical sources, Phys. Rep. 729 (2018) 1.
[24] N. Picqué, T.W. Hänsch, Frequency comb spectroscopy, Nat. Photon. 13 (2019) 146.
[25] S.A. Diddams, T. Udem, J.C. Bergquist, E.A. Curtis, R.E. Drullinger, L. Hollberg, W.M. Itano, W.D. Lee, C.W. Oates, K.R. Vogel, D.J. Wineland, An optical clock based on a single trapped $^{199}Hg^{+}$ ion, Science 293 (2001) 825–828.
[26] T.W. Hänsch, Nobel lecture: Passion for precision, Rev. Modern Phys. 78 (2006) 1297–1309.
[27] L.A. Lugiato, F. Prati, M.L. Gorodetsky, T.J. Kippenberg, From the Lugiato–Lefever equation to microresonator-based soliton Kerr frequency combs, Philos. Trans. R. Soc. A 376 (2135) (2018) 20180113.
[28] A.B. Matsko, A.A. Savchenkov, W. Liang, V.S. Ilchenko, D. Seidel, L. Maleki, Mode-locked Kerr frequency combs, Opt. Lett. 36 (2011) 2845–2847.
[29] S. Coen, H.G. Randle, T. Sylvestre, M. Erkintalo, Modeling of octave-spanning Kerr frequency combs using a generalized mean-field Lugiato–Lefever model, Opt. Lett. 38 (2013) 37–39.
[30] Philippe Grelu, Nonlinear Optical Cavity Dynamics: From Microresonators to Fiber Lasers, John Wiley & Sons, 2015.
[31] W. Liang, A.A. Savchenkov, Z. Xie, J.F. McMillan, J. Burkhart, V.S. Ilchenko, C.W. Wong, A.B. Matsko, L. Maleki, Miniature multi-octave light source based on a monolithic microcavity, Optica 2 (2015) 40–47.
[32] A.A. Savchenkov, A.B. Matsko, W. Liang, V.S. Ilchenko, D. Seidel, L. Maleki, Kerr combs with selectable central frequency, Nat. Photon. 5 (2011) 293–296.
[33] Y.K. Chembo, N. Yu, Modal expansion approach to optical-frequency-comb generation with monolithic whispering-gallery-mode resonators, Phys. Rev. A 82 (2010) 033801.
[34] M. Lipson, J.S. Levy, A. Gondarenko, M.A. Foster, A.C. Turner-Foster, A.L. Gaeta, CMOS-compatible multiple-wavelength oscillator for on-chip optical interconnects, Nat. Photon. 4 (2010) 37–40.
[35] A. Rizzo, A. Novick, V. Gopal, B. Kim, X. Ji, S. Daudlin, Y. Okawachi, Q. Cheng, M. Lipson, A. Gaeta, K. Bergman, Massively scalable Kerr comb-driven silicon photonic link, Nat. Photon. 17 (2023) 1–10.
[36] T.J. Kippenberg, S.M. Spillane, K.J. Vahala, Kerr-nonlinearity optical parametric oscillation in an ultrahigh-Q toroid microcavity, Phys. Rev. Lett. 93 (2004) 083904.
[37] S.B. Papp, K. Beha, P. Del'Haye, F. Quinlan, H. Lee, K.J. Vahala, S.A. Diddams, Microresonator frequency comb optical clock, Optica 1 (2014) 10–14.
[38] M.-G. Suh, K.J. Vahala, Soliton microcomb range measurement, Science 359 (2018) 884–887.

[39] D.T. Spencer, T. Drake, T.C. Briles, J. Stone, L.C. Sinclair, C. Fredrick, Q. Li, D. Westly, B.R. Ilic, A. Bluestone, N. Volet, T. Komljenovic, L. Chang, S.H. Lee, D.Y. Oh, M.-G. Suh, K.Y. Yang, M.H. P. Pfeiffer, T.J. Kippenberg, E. Norberg, L. Theogarajan, K. Vahala, N.R. Newbury, K. Srinivasan, J.E. Bowers, S.A. Diddams, S.B. Papp, An optical-frequency synthesizer using integrated photonics, Nature 557 (2018) 81–85.
[40] ZQ Wang, K Nithyanandan, A Coillet, P Tchofo-Dinda, Ph Grelu, Optical soliton molecular complexes in a passively mode-locked fibre laser, Nat. Commun. 10 (1) (2019) 830.
[41] Xiaoxiao Xue, Yi Xuan, Yang Liu, Pei-Hsun Wang, Steven Chen, Jian Wang, Dan E Leaird, Minghao Qi, Andrew M Weiner, Mode-locked dark pulse Kerr combs in normal-dispersion microresonators, Nat. Photon. 9 (9) (2015) 594–600.
[42] T. Fortier, V. Torres-Company, Optical frequency combs: Driving precision across the fundamental and applied research domains, APL Photon. 9 (6) (2024) 060401.
[43] I. Prigogine, R. Lefever, Symmetry breaking instabilities in dissipative systems. II, J. Chem. Phys. 48 (1968) 1695–1700.
[44] P. Glansdorff, I. Prigogine, Thermodynamic Theory of Structure, Stability and Fluctuations, Wiley, London, UK, 1971.
[45] Ilya Prigogine, Gregoire Nicolis, Self-organization, Non-Equilib. Syst. (1977).
[46] M.C. Cross, p.c. Hohenberg, Pattern formation outside of equilibrium, Rev. Modern Phys. 65 (3) (1993) 851, 85.
[47] Yuri S. Kivshar, Boris A. Malomed, Dynamics of solitons in nearly integrable systems, Rev. Modern Phys. 61 (4) (1989) 763.
[48] Nikolay N. Rosanov, Spatial Hysteresis and Optical Patterns, Springer Science & Business Media, 2002.
[49] Len M. Pismen, Patterns and interfaces in dissipative dynamics, in: Encyclopedia of Complexity and Systems Science, Springer, 2009, pp. 6459–6476.
[50] F. Tito Arecchi, Stefano Boccaletti, PierLuigi Ramazza, Pattern formation and competition in nonlinear optics, Phys. Rep. 318 (1–2) (1999) 1–83.
[51] Jerry P. Gollub, James S. Langer, Pattern formation in nonequilibrium physics, Rev. Modern Phys. 71 (2) (1999) S396.
[52] Daniel Walgraef, Spatio-Temporal Pattern Formation: with Examples from Physics, Chemistry, and Materials Science, Springer Science & Business Media, 2012.
[53] A.M. Turing, The chemical basis of morphogenesis, Philos. Trans. R. Soc. Lond. Ser. B 237 (1952) 37–72.
[54] H. Bénard, Les Tourbillons Cellulaires dans une Nappe Liquide Propageant de la Chaleur Par Convection, en Régime Permanent (Ph.D. thesis), Université de Paris, Paris, France, 1901.
[55] Lord Rayleigh, LIX. On convection currents in a horizontal layer of fluid, when the higher temperature is on the under side, Lond. Edinb. Dublin Philos. Mag. J. Sci. 32 (192) (1916) 529–546.
[56] V. Castets, E. Dulos, J. Boissonade, P. De Kepper, Experimental evidence of a sustained standing Turing-type nonequilibrium chemical pattern, Phys. Rev. Lett. 64 (1990) 2953–2956.
[57] Q. Ouyang, H.L. Swinney, Transition from a uniform state to hexagonal and striped Turing patterns, Nature 352 (1991) 610–612.
[58] B.P. Belousov, A periodic reaction and its mechanism, Compil. Abstr. Radiat. Med. 147 (1959) 1.
[59] A.N. Zaikin, A.M. Zhabotinsky, Concentration wave propagation in two-dimensional liquid-phase self-oscillating system, Nature 225 (1970) 535–537.
[60] Luigi A. Lugiato, René Lefever, Spatial dissipative structures in passive optical systems, Phys. Rev. Lett. 58 (21) (1987) 2209.
[61] Marc Haelterman, Stefano Trillo, Stefan Wabnitz, Dissipative modulation instability in a nonlinear dispersive ring cavity, Opt. Commun. 91 (5–6) (1992) 401–407.
[62] P Kockaert, P Tassin, G Van der Sande, I Veretennicoff, M Tlidi, Negative diffraction pattern dynamics in nonlinear cavities with left-handed materials, Phys. Rev. A—At. Mol. Opt. Phys. 74 (3) (2006) 033822.
[63] Yanne K. Chembo, Curtis R. Menyuk, Spatiotemporal Lugiato–Lefever formalism for Kerr-comb generation in whispering-gallery-mode resonators, Phys. Rev. A 87 (2013) 053852.
[64] J. Kippenberg, R. Holzwarth, S. Diddams, Microresonator-Based optical frequency combs, Science 332 (2011) 555–559.
[65] F. Ferdous, H. Miao, D.E. Leaird, K. Srinivasan, J. Wang, L. Chen, L.T. Varghese, A.M. Weiner, Spectral Line-by-Line pulse shaping of an optical frequency comb generated by a microring resonator, Nat. Photon. 5 (2011) 770–776.
[66] G.J. Morales, Y.C. Lee, Ponderomotive-force effects in a nonuniform plasma, Phys. Rev. Lett. 33 (17) (1974) 1016.
[67] K. Nozaki, N. Bekki, Solitons as attractors of a forced dissipative nonlinear Schrödinger equation, Phys. Lett. A 102 (9) (1984) 383–386.
[68] David James Kaup, Alan C. Newell, Theory of nonlinear oscillating dipolar excitations in one-dimensional condensates, Phys. Rev. B 18 (10) (1978) 5162.
[69] D.W. Mc Laughlin, Jerome V. Moloney, Alan C. Newell, Solitary waves as fixed points of infinite-dimensional maps in an optical bistable ring cavity, Phys. Rev. Lett. 51 (2) (1983) 75.
[70] D.W. McLaughlin, J.V. Moloney, A.C. Newell, New class of instabilities in passive optical cavities, Phys. Rev. Lett. 54 (7) (1985) 681.
[71] L.A. Lugiato, Transverse nonlinear optics: Introduction and review, Chaos Solitons Fractals 4 (8–9) (1994) 1251–1258.
[72] Paul Mandel, Mustapha Tlidi, Transverse dynamics in cavity nonlinear optics (2000–2003), J. Opt. B: Quantum Semiclassical Opt. 6 (9) (2004) R60.
[73] M. Tlidi, M. Taki, T. Kolokolnikov, Introduction: dissipative localized structures in extended systems, Chaos 17 (3) (2007).
[74] Orazio Descalzi, Marcel Clerc, Stefania Residori, Gaetano Assanto, Localized States in Physics: Solitons and Patterns, Springer Science & Business Media, 2011.
[75] Y.K. Chembo, D. Gomila, M. Tlidi, C.R. Menyuk, Theory and applications of the Lugiato-Lefever equation, Eur. Phys. J. D 71 (11) (2017) 299.
[76] L.D. Landau, E.M. Lifshitz, Mechanics, in: Course of Theoretical Physics, Vol. 1, Pergamon Press, 1976.
[77] A. Frova, M. Marenzana, Thus Spoke Galileo: The Great Scientist's Ideas and Their Relevance to the Present Day, Oxford University Press, 2006.
[78] Jesús Cuevas-Maraver, Panayotis G. Kevrekidis, Floyd Williams (Eds.), The Sine-Gordon Model and its Applications: From Pendula and Josephson Junctions to Gravity and High-Energy Physics, in: Nonlinear Systems and Complexity, Vol. 10, Springer, Cham, 2014.
[79] M.A. Ferré, M.G. Clerc, S. Coulibally, R.G. Rojas, M Tlidi, Localized structures and spatiotemporal chaos: comparison between the driven damped sine-Gordon and the Lugiato-Lefever model, Eur. Phys. J. D 71 (6) (2017) 172.
[80] I.V. Barashenkov, Y.S. Smirnov, Title not provided, Phys. Rev. E 54 (1996) 5707–5714.
[81] K. Nozaki, N. Bekki, Chaotic solitons in a plasma driven by a RF field, J. Phys. Soc. Japan 54 (1985) 2363–2366.
[82] K. Nozaki, N. Bekki, Low-Dimensional chaos in a driven damped nonlinear Schrödinger equation, Phys. D 21 (1986) 381–393.
[83] Boris A. Malomed, Bound states of envelope solitons, Phys. Rev. E 47 (4) (1993) 2874.
[84] S. Wabnitz, Suppression of interactions in a phase-locked soliton optical memory, Opt. Lett. 18 (1993) 601–603.
[85] F. Arecchi, R. Bonifacio, Theory of optical maser amplifiers, IEEE J. Quantum Electron. 1 (4) (1965) 169–178.
[86] Paul Mandel, Nonlinear Optics: An Analytical Approach, Wiley-VCH, 2010.
[87] Hermann Haken, Optical resonators, in: Laser Theory, Springer, 1984, pp. 9–24.
[88] Leslie Allen, Joseph H. Eberly, Optical Resonance and Two-Level Atoms, Courier Corporation, 2012.
[89] Marlan O. Scully, M. Suhail Zubairy, Quantum Optics, Cambridge University Press, 1997.
[90] A.C. Newell, J.V. Moloney, Nonlinear Optics, Addison-Wesley Publishing Company, New York, 1992.

[91] M. Tlidi, M. Taki, Rogue waves in nonlinear optics, Adv. Opt. Photon. 14 (1) (2022) 87–147.
[92] M. Tlidi, M. Haelterman, P. Mandel, 3D patterns and pattern selection in optical bistability, Europhys. Lett. 42 (5) (1998) 505.
[93] M. Tlidi, M. Haelterman, P. Mandel, Three-dimensional structures in diffractive and dispersive nonlinear ring cavities, Quantum Semiclassical Opt.: J. Eur. Opt. Soc. B 10 (6) (1998) 869.
[94] P Tassin, Guy Van der Sande, N Veretenov, P Kockaert, I Veretennicoff, M Tlidi, Three-dimensional structures in nonlinear cavities containing left-handed materials, Opt. Express 14 (20) (2006) 9338–9343.
[95] Bilal Kostet, Dynamics of localized structures in Kerr resonators (Ph.D. thesis), Université libre de Bruxelles, Brussels, Belgium, 2024.
[96] A.J. Scorggie, W.J. Firth, G.S. McDonald, M. Tlidi, R. Lefever, L.A. Lugiato, Pattern formation in a passive Kerr cavity, Chaos Solitons Fractals 4 (1994) 1323–1334.
[97] Hannes Uecker, Daniel Wetzel, Jens D.M. Rademacher, Pde2path-A Matlab package for continuation and bifurcation in 2D elliptic systems, Numer. Math. Theory Methods Appl. 7 (1) (2014) 58–106.
[98] P.D. Woods, A.R. Champneys, Heteroclinic tangles and homoclinic snaking in the unfolding of a degenerate reversible Hamiltonian–Hopf bifurcation, Phys. D 129 (3–4) (1999) 147–170.
[99] Pierre Coullet, C. Riera, Charles Tresser, Stable static localized structures in one dimension, Phys. Rev. Lett. 84 (14) (2000) 3069.
[100] John Burke, Edgar Knobloch, Snakes and ladders: localized states in the Swift–Hohenberg equation, Phys. Lett. A 360 (6) (2007) 681–688.
[101] Marcel G. Clerc, Claudio Falcon, Localized patterns and hole solutions in one-dimensional extended systems, Phys. A 356 (1) (2005) 48–53.
[102] F Haudin, RG Rojas, U Bortolozzo, Stefania Residori, MG Clerc, Homoclinic snaking of localized patterns in a spatially forced system, Phys. Rev. Lett. 107 (26) (2011) 264101.
[103] Alain Bergeon, J. Burke, E. Knobloch, I. Mercader, Eckhaus instability and homoclinic snaking, Phys. Rev. E 78 (4) (2008) 046201.
[104] Nicolas Périnet, Nicolas Verschueren, Saliya Coulibaly, Eckhaus instability in the Lugiato-Lefever model, Eur. Phys. J. D 71 (9) (2017) 243.
[105] F. Tabbert, S.V. Gurevich, K. Panajotov, M. Tlidi, Space-Time dynamics of high-q optical resonators, in: Nonequilibrium Thermodynamics and Fluctuation Kinetics: Modern Trends and Open Questions, Springer, 2022, pp. 247–269.
[106] M. Tlidi, P. Mandel, R. Lefever, Localized structures and localized patterns in optical bistability, Phys. Rev. Lett. 73 (5) (1994) 640.
[107] Mustapha Tlidi, Paul Mandel, Spatial patterns in nascent optical bistability, Chaos Solitons Fractals 4 (8–9) (1994) 1475–1486.
[108] François Leo, Stéphane Coen, Pascal Kockaert, Simon-Pierre Gorza, Philippe Emplit, Marc Haelterman, Temporal cavity solitons in one-dimensional Kerr media as bits in an all-optical buffer, Nat. Photon. 4 (7) (2010) 471–476.
[109] V. Odent, M. Taki, E. Louvergneaux, Experimental evidence of dissipative spatial solitons in an optical passive Kerr cavity, New J. Phys. 13 (11) (2011) 113026.
[110] Yves Pomeau, Front motion, metastability and subcritical bifurcations in hydrodynamics, Phys. D 23 (1–3) (1986) 3–11.
[111] Giles W. Hunt, Gabriel James Lord, A.R. Champneys, Homoclinic and heteroclinic orbits underlying the post-buckling of axially-compressed cylindrical shells, Comput. Methods Appl. Mech. Engrg. 170 (3–4) (1999) 239–251.
[112] Damia Gomila, Andrew J. Scroggie, William J. Firth, Bifurcation structure of dissipative solitons, Phys. D 227 (1) (2007) 70–77.
[113] Mustapha Tlidi, Lendert Gelens, High-order dispersion stabilizes dark dissipative solitons in all-fiber cavities, Opt. Lett. 35 (3) (2010) 306–308.
[114] Pedro Parra-Rivas, Damià Gomila, Manuel A Matías, Stéphane Coen, Lendert Gelens, Dynamics of localized and patterned structures in the Lugiato-Lefever equation determine the stability and shape of optical frequency combs, Phys. Rev. A 89 (4) (2014) 043813.
[115] A.G. Vladimirov, J.M. McSloy, D.V. Skryabin, J. Firth, Two-dimensional clusters of solitary structures in driven optical cavities, Phys. Rev. E 65 (4) (2002) 046606.
[116] M. Tlidi, A.G. Vladimirov, P. Mandel, Interaction and stability of periodic and localized structures in optical bistable systems, IEEE J. Quantum Electron. 39 (2) (2003) 216–226.
[117] A.G. Vladimirov, S.V. Gurevich, M. Tlidi, Effect of Cherenkov radiation on localized-state interaction, Phys. Rev. A 97 (1) (2018) 013816.
[118] Andrei G. Vladimirov, Mustapha Tlidi, Majid Taki, Dissipative soliton interaction in Kerr resonators with high-order dispersion, Phys. Rev. A 103 (6) (2021) 063505.
[119] D. Turaev, A.G. Vladimirov, S. Zelik, Long-Range interaction and synchronization of oscillating dissipative solitons, Phys. Rev. Lett. 108 (2012) 263906.
[120] D.A. Dolinina, D.V. Turaev, A.G. Vladimirov, Soliton interaction and bound-state formation in coupled Kerr resonators, Phys. Rev. A 113 (2026) 053507.
[121] A.G. Vladimirov, R. Lefever, M. Tlidi, Relative stability of multipeak localized patterns of cavity solitons, Phys. Rev. A—At. Mol. Opt. Phys. 84 (4) (2011) 043848.
[122] N. Verschueren, E. Knobloch, H. Uecker, Localized and extended patterns in the cubic-quintic Swift-Hohenberg equation on a disk, Phys. Rev. E 104 (1) (2021) 014208.
[123] Boris A Malomed, Dumitru Mihalache, Frank Wise, Lluis Torner, Spatiotemporal optical solitons, J. Opt. B: Quantum Semiclassical Opt. 7 (5) (2005) R53.
[124] Boris A. Malomed, Multidimensional solitons: Well-established results and novel findings, Eur. Phys. J. Spec. Top. 225 (13) (2016) 2507–2532.
[125] Dumitru Mihalache, Multidimensional localized structures in optical and matter-wave media: a topical survey of recent literature, Rom. Rep. Phys. 69 (1) (2017) 403.
[126] Mustapha Tlidi, Paul Mandel, Three-dimensional optical crystals and localized structures in cavity second harmonic generation, Phys. Rev. Lett. 83 (24) (1999) 4995.
[127] M. Tlidi, Three-dimensional crystals and localized structures indiffractive and dispersive nonlinear ring cavities, J. Opt. B: Quantum Semiclassical Opt. 2 (3) (2000) 438.
[128] Nikolay Veretenov, Mustapha Tlidi, Dissipative light bullets in an optical parametric oscillator, Phys. Rev. A—At. Mol. Opt. Phys. 80 (2) (2009) 023822.
[129] Sergey V Fedorov, Nikolay N Rosanov, Anatoly N Shatsev, Nikolay A Veretenov, Andrei G Vladimirov, Topologically multicharged and multihumped rotating solitons in wide-aperture lasers with a saturable absorber, IEEE J. Quantum Electron. 39 (2) (2003) 197–205.
[130] N.A. Veretenov, N.N. Rozanov, S.V. Fedorov, Clusters of three-dimensional laser solitons and their collisions, Opt. Spectrosc. 104 (4) (2008) 563–566.
[131] N.A. Veretenov, N.N. Rosanov, S.V. Fedorov, Motion of complexes of 3D-laser solitons, Opt. Quantum Electron. 40 (2) (2008) 253–262.
[132] D Mihalache, D Mazilu, L-C Crasovan, BA Malomed, F Lederer, Three-dimensional spinning solitons in the cubic-quintic nonlinear medium, Phys. Rev. E 61 (6) (2000) 7142.
[133] B.A. Malomed, L.-C. Crasovan, D. Mihalache, Stability of vortex solitons in the cubic-quintic model, Phys. D 161 (3–4) (2002) 187–201.
[134] Dumitru Mihalache, D Mazilu, F Lederer, Hervé Leblond, Boris A Malomed, Collisions between counter-rotating solitary vortices in the three-dimensional Ginzburg-Landau equation, Phys. Rev. E 78 (5) (2008) 056601.
[135] Dumitru Mihalache, Multidimensional localized structures in optics and Bose-Einstein condensates: A selection of recent studies, Romanian J. Phys. 59 (3–4) (2014) 295–312.
[136] M. Brambilla, T. Maggipinto, G. Patera, L. Columbo, Cavity light bullets: Three-dimensional localized structures in a nonlinear optical resonator, Phys. Rev. Lett. 93 (20) (2004) 203901.

[137] L. Columbo, I.M. Perrini, Tommaso Maggipinto, M. Brambilla, 3D self-organized patterns in the field profile of a semiconductor resonator, New J. Phys. 8 (12) (2006) 312.
[138] Yaron Silberberg, Collapse of optical pulses, Opt. Lett. 15 (22) (1990) 1282–1284.
[139] V. Boucher, Hervé Leblond, X. Nguyen Phu, Multiscale theory of nonlinear wavepacket propagation in a planar optical waveguide, J. Opt. A: Pure Appl. Opt. 4 (5) (2002) 514.
[140] S.S. Gopalakrishnan, K. Panajotov, M. Taki, M. Tlidi, Dissipative light bullets in Kerr cavities: multistability, clustering, and rogue waves, Phys. Rev. Lett. 126 (15) (2021) 153902.
[141] M. Tlidi, S.S. Gopalakrishnan, M. Taki, K. Panajotov, Optical crystals and light-bullets in Kerr resonators, Chaos Solitons Fractals 152 (2021) 111364.
[142] A. Zakery, Stephen Richard Elliott, Optical Nonlinearities in Chalcogenide Glasses and their Applications, Springer, 2007.
[143] GE Snopatin, VS Shiryaev, VG Plotnichenko, EM Dianov, MF Churbanov, High-purity chalcogenide glasses for fiber optics, Inorg. Mater. 45 (13) (2009) 1439–1460.
[144] Ian Hendry, Wei Chen, Yadong Wang, Bruno Garbin, Julien Javaloyes, Gian-Luca Oppo, Stéphane Coen, Stuart G Murdoch, Miro Erkintalo, Spontaneous symmetry breaking and trapping of temporal Kerr cavity solitons by pulsed or amplitude-modulated driving fields, Phys. Rev. A 97 (5) (2018) 053834.
[145] Daniel C Cole, Jordan R Stone, Miro Erkintalo, Ki Youl Yang, Xu Yi, Kerry J Vahala, Scott B Papp, Kerr-microresonator solitons from a chirped background, Optica 5 (10) (2018) 1304–1310.
[146] Alexander U. Nielsen, Yiqing Xu, Caleb Todd, Michel Ferré, Marcel G Clerc, Stéphane Coen, Stuart G Murdoch, Miro Erkintalo, Nonlinear localization of dissipative modulation instability, Phys. Rev. Lett. 127 (12) (2021) 123901.
[147] Felix Tabbert, Tobias Frohoff-Hülsmann, Krassimir Panajotov, Mustapha Tlidi, Svetlana V Gurevich, Stabilization of localized structures by inhomogeneous injection in Kerr resonators, Phys. Rev. A 100 (1) (2019) 013818.
[148] Wen-Rong Sun, Wei-Chao Ma, Boris A. Malomed, Dissipative structures in one-and two-dimensional Kerr cavities with a spatially periodic pump, Phys. Rev. A 112 (1) (2025) 013501.
[149] Raymond E Goldstein, Gemunu H Gunaratne, L Gil, P Coullet, Hydrodynamic and interfacial patterns with broken space-time symmetry, Phys. Rev. A 43 (12) (1991) 6700.
[150] Vincent Odent, M Tlidi, MG Clerc, P Glorieux, Eric Louvergneaux, Experimental observation of front propagation in a negatively diffractive inhomogeneous Kerr cavity, Phys. Rev. A 90 (1) (2014) 011806.
[151] D.N. Christodoulides, R.I. Joseph, Discrete Self-Focusing in nonlinear arrays of coupled waveguides, Opt. Lett. 13 (9) (1988) 794–796.
[152] AB Aceves, Costantino De Angelis, T Peschel, R Muschall, F Lederer, Stefano Trillo, Stefan Wabnitz, Discrete self-trapping, soliton interactions, and beam steering in nonlinear waveguide arrays, Phys. Rev. E 53 (1) (1996) 1172.
[153] Yuri S. Kivshar, Tristram J. Alexander, Sergey K. Turitsyn, Nonlinear modes of a macroscopic quantum oscillator, Phys. Lett. A 278 (4) (2001) 225–230.
[154] Masaya Notomi, Theory of light propagation in strongly modulated photonic crystals: Refractionlike behavior in the vicinity of the photonic band gap, Phys. Rev. B 62 (16) (2000) 10696.
[155] Kestutis Staliunas, Midband dissipative spatial solitons, Phys. Rev. Lett. 91 (5) (2003) 053901.
[156] B Eiermann, P Treutlein, Th Anker, M Albiez, M Taglieber, K-P Marzlin, MK Oberthaler, Dispersion management for atomic matter waves, Phys. Rev. Lett. 91 (6) (2003) 060402.
[157] Dragomir N. Neshev, Tristram J. Alexander, Elena A. Ostrovskaya, Yuri S. Kivshar, Hector Martin, Igor Makasyuk, Zhigang Chen, Observation of discrete vortex solitons in optically induced photonic lattices, Phys. Rev. Lett. 92 (12) (2004) 123903.
[158] Claudio Conti, Stefano Trillo, Nonspreading wave packets in three dimensions formed by an ultracold bose gas in an optical lattice, Phys. Rev. Lett. 92 (12) (2004) 120404.
[159] Kestutis Staliunas, Ramon Herrero, Nondiffractive propagation of light in photonic crystals, Phys. Rev. E 73 (1) (2006) 016601.
[160] Damiá Gomila, Gian-Luca Oppo, Subcritical patterns and dissipative solitons due to intracavity photonic crystals, Phys. Rev. A 76 (4) (2007) 043823.
[161] J.A. Arnaud, Degenerate optical cavities, Appl. Opt. 8 (1) (1969) 189–196.
[162] P Tassin, L Gelens, J Danckaert, I Veretennicoff, G Van der Sande, P Kockaert, M Tlidi, Dissipative structures in left-handed material cavity optics, Chaos 17 (3) (2007).
[163] Allan Boardman, Mark Brongersma, Mark Stockman, Martin Wegener, Plasmonics and metamaterials: Introduction, J. Opt. Soc. Am. B 26 (12) (2009) PM1.
[164] Stefania Residori, A Petrossian, Tomoyuki Nagaya, CS Riera, MG Clerc, Fronts and localized structures in a liquid-crystal-light-valve with optical feedback, Phys. D 199 (1–2) (2004) 149–165.
[165] S. Coen, M. Tlidi, Ph Emplit, M. Haelterman, Convection versus dispersion in optical bistability, Phys. Rev. Lett. 83 (12) (1999) 2328.
[166] Bruno Garbin, Yadong Wang, Stuart G Murdoch, Gian-Luca Oppo, Stéphane Coen, Miro Erkintalo, Experimental and numerical investigations of switching wave dynamics in a normally dispersive fibre ring resonator, Eur. Phys. J. D 71 (9) (2017) 240.
[167] Pedro Parra-Rivas, Damià Gomila, Manuel A Matías, Pere Colet, Dissipative soliton excitability induced by spatial inhomogeneities and drift, Phys. Rev. Lett. 110 (6) (2013) 064103.
[168] Pedro Parra-Rivas, Damià Gomila, Manuel A Matías, Pere Colet, Lendert Gelens, Effects of inhomogeneities and drift on the dynamics of temporal solitons in fiber cavities and microresonators, Opt. Express 22 (25) (2014) 30943–30954.
[169] Yiqing Xu, Stéphane Coen, Experimental observation of the spontaneous breaking of the time-reversal symmetry in a synchronously pumped passive Kerr resonator, Opt. Lett. 39 (12) (2014) 3492–3495.
[170] Jae K Jang, Miro Erkintalo, Stephane Coen, Stuart G Murdoch, Temporal tweezing of light through the trapping and manipulation of temporal cavity solitons, Nat. Commun. 6 (1) (2015) 7370.
[171] Hossein Taheri, Ali A Eftekhar, Kurt Wiesenfeld, Ali Adibi, Soliton formation in whispering-gallery-mode resonators via input phase modulation, IEEE Photon. J. 7 (2) (2015) 1–9.
[172] V.E. Lobanov, G. Lihachev, T.J. Kippenberg, M.L. Gorodetsky, Frequency combs and platicons in optical microresonators with normal GVD, Opt. Express 23 (6) (2015) 7713.
[173] Hossein Taheri, Andrey B. Matsko, Lute Maleki, Optical lattice trap for Kerr solitons, Eur. Phys. J. D 71 (6) (2017) 153.
[174] Ewelina Obrzud, Steve Lecomte, Tobias Herr, Temporal solitons in microresonators driven by optical pulses, Nat. Photon. 11 (9) (2017) 600–607.
[175] W.J. Firth, A.J. Scroggie, Optical bullet holes: robust controllable localized states of a nonlinear cavity, Phys. Rev. Lett. 76 (10) (1996) 1623.
[176] Tommaso Maggipinto, M. Brambilla, G.K. Harkness, W.J. Firth, Cavity solitons in semiconductor microresonators: Existence, stability, and dynamical properties, Phys. Rev. E 62 (6) (2000) 8726.
[177] S Fedorov, D Michaelis, Ulf Peschel, C Etrich, DV Skryabin, N Rosanov, F Lederer, Effects of spatial inhomogeneities on the dynamics of cavity solitons in quadratically nonlinear media, Phys. Rev. E 64 (3) (2001) 036610.
[178] F Pedaci, P Genevet, S Barland, M Giudici, JR Tredicce, Positioning cavity solitons with a phase mask, Appl. Phys. Lett. 89 (22) (2006).

[179] AG Vladimirov, DV Skryabin, G Kozyreff, P Mandel, M Tlidi, Bragg localized structures in a passive cavity with transverse modulation of the refractive index and the pump, Opt. Express 14 (1) (2006) 1–6.
[180] C. Fernandez-Oto, M.G. Clerc, D. Escaff, M. Tlidi, Strong nonlocal coupling stabilizes localized structures: an analysis based on front dynamics, Phys. Rev. Lett. 110 (17) (2013) 174101.
[181] D. Escaff, C. Fernandez-Oto, M.G. Clerc, M. Tlidi, Localized vegetation patterns, fairy circles, and localized patches in arid landscapes, Phys. Rev. E 91 (2) (2015) 022924.
[182] M Tlidi, C Fernandez-Oto, MG Clerc, D Escaff, P Kockaert, Localized plateau beam resulting from strong nonlocal coupling in a cavity filled by metamaterials and liquid-crystal cells, Phys. Rev. A 92 (5) (2015) 053838.
[183] Klaus Petermann, External optical feedback phenomena in semiconductor lasers, IEEE J. Sel. Top. Quantum Electron. 1 (2) (1995) 480–489.
[184] Rifat Sipahi, Silviu-Iulian Niculescu, Chaouki T Abdallah, Wim Michiels, Keqin Gu, Stability and stabilization of systems with time delay, IEEE Control Syst. Mag. 31 (1) (2011) 38–65.
[185] Tamás Insperger, Gábor Stépán, Semi-Discretization for Time-Delay Systems: Stability and Engineering Applications, vol. 178, Springer Science & Business Media, 2011.
[186] C Otto, K Lüdge, AG Vladimirov, M Wolfrum, Eckehard Schöll, Delay-induced dynamics and jitter reduction of passively mode-locked semiconductor lasers subject to optical feedback, New J. Phys. 14 (11) (2012) 113033.
[187] Thomas Erneux, Julien Javaloyes, Matthias Wolfrum, Serhiy Yanchuk, Introduction to focus issue: time-delay dynamics, Chaos 27 (11) (2017).
[188] Guy Van der Sande, Daniel Brunner, Miguel C. Soriano, Advances in photonic reservoir computing, Nanophotonics 6 (3) (2017) 561–576.
[189] Yanne K Chembo, Daniel Brunner, Maxime Jacquot, Laurent Larger, Optoelectronic oscillators with time-delayed feedback, Rev. Modern Phys. 91 (3) (2019) 035006.
[190] Thomas Erneux, Applied Delay Differential Equations, Springer, 2009.
[191] Lennert Appeltant, Miguel Cornelles Soriano, Guy Van der Sande, Jan Danckaert, Serge Massar, Joni Dambre, Benjamin Schrauwen, Claudio R Mirasso, Ingo Fischer, Information processing using a single dynamical node as complex system, Nat. Commun. 2 (1) (2011) 468.
[192] Yvan Paquot, Francois Duport, Antoneo Smerieri, Joni Dambre, Benjamin Schrauwen, Marc Haelterman, Serge Massar, Optoelectronic reservoir computing, Sci. Rep. 2 (1) (2012) 287.
[193] Romain Modeste Nguimdo, Guy Verschaffelt, Jan Danckaert, Guy Van der Sande, Fast photonic information processing using semiconductor lasers with delayed optical feedback: Role of phase dynamics, Opt. Express 22 (7) (2014) 8672–8686.
[194] Lennert Appeltant, Guy Van der Sande, Jan Danckaert, Ingo Fischer, Constructing optimized binary masks for reservoir computing with delay systems, Sci. Rep. 4 (1) (2014) 3629.
[195] Laurent Larger, Antonio Baylón-Fuentes, Romain Martinenghi, Vladimir S Udaltsov, Yanne K Chembo, Maxime Jacquot, High-speed photonic reservoir computing using a time-delay-based architecture: Million words per second classification, Phys. Rev. X 7 (1) (2017) 011015.
[196] Changdi Zhou, Penghua Mu, Yu Huang, Yigong Yang, Pei Zhou, Kuenyao Lau, Nianqiang Li, Deep photonic reservoir computing based on a distributed feedback laser array, APL Photon. 10 (2) (2025) 026103.
[197] L. Goldmann, M. Richter, S. Höfling, Speedup of Delay-Based photonic reservoir computing using integrated feedback loops, Opt. Express 33 (4) (2025) 5123–5141.
[198] M. Tlidi, E. Averlant, A.G. Vladimirov, K. Panajotov, Delay feedback induces a spontaneous motion of two-dimensional cavity solitons in driven semiconductor microcavities, Phys. Rev. A—At. Mol. Opt. Phys. 86 (3) (2012) 033822.
[199] Krassimir Panajotov, Mustapha Tlidi, Spontaneous motion of cavity solitons in vertical-cavity lasers subject to optical injection and to delayed feedback, Eur. Phys. J. D 59 (1) (2010) 67–72.
[200] A Pimenov, AG Vladimirov, SV Gurevich, K Panajotov, G Huyet, M Tlidi, Delayed feedback control of self-mobile cavity solitons, Phys. Rev. A—At. Mol. Opt. Phys. 88 (5) (2013) 053830.
[201] AG Vladimirov, A Pimenov, SV Gurevich, K Panajotov, E Averlant, M Tlidi, Cavity solitons in vertical-cavity surface-emitting lasers, Philos. Trans. R. Soc. A 372 (2027) (2014) 20140013.
[202] Morten Bache, Franco Prati, Giovanna Tissoni, Reza Kheradmand, LA Lugiato, I Protsenko, Massimo Brambilla, Cavity soliton laser based on VCSEL with saturable absorber, Appl. Phys. B 81 (7) (2005) 913–920.
[203] Krassimir Panajotov, Mustapha Tlidi, Chaotic behavior of cavity solitons induced by time delay feedback, Opt. Lett. 39 (16) (2014) 4739–4742.
[204] F Selmi, Saliya Coulibaly, Z Loghmari, Isabelle Sagnes, Gregoire Beaudoin, Marcel G Clerc, Sylvain Barbay, Spatiotemporal chaos induces extreme events in an extended microcavity laser, Phys. Rev. Lett. 116 (1) (2016) 013901.
[205] Mathias Marconi, Julien Javaloyes, Stéphane Barland, Salvador Balle, Massimo Giudici, Vectorial dissipative solitons in vertical-cavity surface-emitting lasers with delays, Nat. Photon. 9 (7) (2015) 450.
[206] Roy Lang, Kohroh Kobayashi, External optical feedback effects on semiconductor injection laser properties, IEEE J. Quantum Electron. 16 (3) (1980) 347–355.
[207] Lorenzo Spinelli, G Tissoni, M Brambilla, Franco Prati, LA Lugiato, Spatial solitons in semiconductor microcavities, Phys. Rev. A 58 (3) (1998) 2542.
[208] S Barland, JR Tredicce, M Brambilla, LA Lugiato, S Balle, M Giudici, T Maggipinto, L Spinelli, G Tissoni, T Knoedl, et al., Cavity solitons as pixels in semiconductor microcavities, Nature 419 (6908) (2002) 699–702.
[209] Patrice Genevet, Stéphane Barland, Massimo Giudici, Jorge R Tredicce, Cavity soliton laser based on mutually coupled semiconductor microresonators, Phys. Rev. Lett. 101 (12) (2008) 123905.
[210] Mathias Marconi, Julien Javaloyes, Salvador Balle, Massimo Giudici, How lasing localized structures evolve out of passive mode locking, Phys. Rev. Lett. 112 (22) (2014) 223901.
[211] Adrian Bartolo, Nathan Vigne, Mathias Marconi, Grégoire Beaudoin, Luc Le Gratiet, Konstantinos Pantzas, Isabelle Sagnes, Arnaud Garnache, Massimo Giudici, Spatiotemporally reconfigurable light in degenerate laser cavities, Photon. Res. 11 (10) (2023) 1751–1756.
[212] D. Lenstra, G. Vemuri, M. Yousefi, Generalized optical feedback, in: D. Kane, A. Shore (Eds.), Unlocking Dynamical Diversity: Optical Feedback Effects on Semiconductor Lasers, John Wiley & Sons Ltd, Chichester, UK, 2005, pp. 55–80.
[213] Eric Lacot, Richard Day, J Pinel, Frédéric Stoeckel, Laser relaxation-oscillation frequency imaging, Opt. Lett. 26 (19) (2001) 1483–1485.
[214] M. Tlidi, A.G. Vladimirov, D. Pieroux, D. Turaev, Spontaneous motion of cavity solitons induced by a delayed feedback, Phys. Rev. Lett. 103 (10) (2009) 103904.
[215] M. Tlidi, M. Georgiou, P. Mandel, Transverse patterns in nascent optical bistability, Phys. Rev. A 48 (6) (1993) 4605.
[216] Paul Mandel, Miltos Georgiou, Thomas Erneux, Transverse effects in coherently driven nonlinear cavities, Phys. Rev. A 47 (5) (1993) 4277.
[217] M Tlidi, AG Vladimirov, D Turaev, G Kozyreff, D Pieroux, T Erneux, Spontaneous motion of localized structures and localized patterns induced by delayed feedback, Eur. Phys. J. D 59 (1) (2010) 59–65.
[218] Mark Kness, Laurette S. Tuckerman, Dwight Barkley, Symmetry-breaking bifurcations in one-dimensional excitable media, Phys. Rev. A 46 (8) (1992) 5054.
[219] K Panajotov, D Puzyrev, AG Vladimirov, SV Gurevich, M Tlidi, Impact of time-delayed feedback on spatiotemporal dynamics in the Lugiato-Lefever model, Phys. Rev. A 93 (4) (2016) 043835.

[220] Mustapha Tlidi, Krassimir Panajotov, Two-dimensional dissipative rogue waves due to time-delayed feedback in cavity nonlinear optics, Chaos 27 (1) (2017).
[221] Z Liu, M Ouali, S Coulibaly, MG Clerc, M Taki, M Tlidi, Characterization of spatiotemporal chaos in a Kerr optical frequency comb and in all fiber cavities, Opt. Lett. 42 (6) (2017) 1063–1066.
[222] Nail Akhmediev, Bertrand Kibler, Fabio Baronio, Milivoj Belić, Wei-Ping Zhong, Yiqi Zhang, Wonkeun Chang, Jose M Soto-Crespo, Peter Vouzas, Philippe Grelu, et al., Roadmap on optical rogue waves and extreme events, J. Opt. 18 (6) (2016) 063001.
[223] E. Lobanov, A.E. Shitikov, R.R. Galiev, K.N. Min'kov, O.V. Borovkova, N.M. Kondratiev, Generation of vector flat-top solitons and hybrid bright–flat-top soliton complexes in optical microresonators via modulated pump, Phys. Rev. A 104 (6) (2021) 063511.
[224] S.T. Cundiff, B.C. Collings, N.N. Akhmediev, J.M. Soto-Crespo, K. Bergman, W.H. Knox, Observation of polarization-locked vector solitons in an optical fiber, Phys. Rev. Lett. 82 (20) (1999) 3988–3991.
[225] Sergey V Sergeyev, Chengbo Mou, Elena G Turitsyna, Alexey Rozhin, Sergei K Turitsyn, Keith Blow, Spiral attractor created by vector solitons, Light.: Sci. Appl. 3 (1) (2014) e131.
[226] B Kostet, SS Gopalakrishnan, E Averlant, Y Soupart, K Panajotov, M Tlidi, Vectorial dark dissipative solitons in Kerr resonators, OSA Contin. 4 (5) (2021) 1564–1570.
[227] B. Kostet, Y. Soupart, K. Panajotov, M. Tlidi, Coexistence of dark vector soliton Kerr combs in normal dispersion resonators, Phys. Rev. A 104 (5) (2021) 053530.
[228] E. Averlant, M. Tlidi, K. Panajotov, L. Weicker, Coexistence of cavity solitons with different polarization states and different power peaks in all-fiber resonators, Opt. Lett. 42 (2017) 2750–2753.
[229] F. Copie, M.T. M. Woodley, L. Del Bino, J.M. Silver, S. Zhang, P. Del'Haye, Interplay of polarization and time-reversal symmetry breaking in synchronously pumped ring resonators, Phys. Rev. Lett. 122 (2019) 013905.
[230] R. Suzuki, S. Fujii, A. Hori, T. Tanabe, Theoretical study on dual-comb generation and soliton trapping in a single microresonator with orthogonally polarized dual pumping, IEEE Photon. J. 11 (2019) 1.
[231] M. Saha, S. Roy, S.K. Varshney, Polarization dynamics of a vector cavity soliton in a birefringent fiber resonator, Phys. Rev. A 101 (2020) 033826.
[232] Bruno Garbin, Julien Fatome, Gian-Luca Oppo, Miro Erkintalo, Stuart G Murdoch, Stéphane Coen, Dissipative polarization domain walls in a passive coherently driven Kerr resonator, Phys. Rev. Lett. 126 (2) (2021) 023904.
[233] Alexander U Nielsen, Bruno Garbin, Stéphane Coen, Stuart G Murdoch, Miro Erkintalo, Coexistence and interactions between nonlinear states with different polarizations in a monochromatically driven passive Kerr resonator, Phys. Rev. Lett. 123 (1) (2019) 013902.
[234] Nail Akhmediev, J.M. Soto-Crespo, Dynamics of solitonlike pulse propagation in birefringent optical fibers, Phys. Rev. E 49 (6) (1994) 5742.
[235] Xavier Hachair, Giovanna Tissoni, Hugo Thienpont, Krassimir Panajotov, Linearly polarized bistable localized structure in medium-size vertical-cavity surface-emitting lasers, Phys. Rev. A—At. Mol. Opt. Phys. 79 (1) (2009) 011801.
[236] E Averlant, M Tlidi, H Thienpont, T Ackemann, K Panajotov, Vector cavity solitons in broad area vertical-cavity surface-emitting lasers, Sci. Rep. 6 (1) (2016) 20428.
[237] Marc Haelterman, A.P. Sheppard, A.W. Snyder, Bound-vector solitary waves in isotropic nonlinear dispersive media, Opt. Lett. 18 (17) (1993) 1406–1408.
[238] T. Hansson, M. Bernard, S. Wabnitz, Modulational instability of nonlinear polarization mode coupling in microresonators, J. Opt. Soc. Am. B 35 (4) (2018) 835–841.
[239] C. Mou, S. Sergeyev, A. Rozhin, S. Turitsyn, All-fiber polarization-locked vector soliton laser using carbon nanotubes, Opt. Lett. 36 (19) (2011) 3831–3833.
[240] D.Y. Tang, Y.F. Song, J. Guo, Y.J. Xiang, D.Y. Shen, Polarization domain formation and domain dynamics in a quasi-isotropic cavity fiber laser, IEEE J. Sel. Top. Quantum Electron. 20 (5) (2014) 42–50.
[241] Nikita Tarasov, Auro M Perego, Dmitry V Churkin, Kestutis Staliunas, Sergei K Turitsyn, Mode-locking via dissipative faraday instability, Nat. Commun. 7 (1) (2016) 12441.
[242] A.M. Perego, N. Tarasov, D.V. Churkin, S.K. Turitsyn, K. Staliunas, Title missing, Phys. Rev. Lett. 116 (2016) 028701.
[243] Gang Xu, Alexander U Nielsen, Bruno Garbin, Lewis Hill, Gian-Luca Oppo, Julien Fatome, Stuart G Murdoch, Stéphane Coen, Miro Erkintalo, Spontaneous symmetry breaking of dissipative optical solitons in a two-component Kerr resonator, Nat. Commun. 12 (1) (2021) 4023.
[244] S.V. Sergeyev, H. Kbashi, N. Tarasov, Y. Loiko, S.A. Kolpakov, Title missing, Phys. Rev. Lett. 118 (2017) 033904.
[245] Russell Chipman, Wai Sze Tiffany Lam, Garam Young, Polarized Light and Optical Systems, CRC Press, 2018.
[246] Marc Haelterman, A.P. Sheppard, Polarization domain walls in diffractive or dispersive Kerr media, Opt. Lett. 19 (2) (1994) 96–98.
[247] Tobias Hansson, Stefan Wabnitz, Frequency comb generation beyond the Lugiato–Lefever equation: multi-stability and super cavity solitons, J. Opt. Soc. Am. B 32 (7) (2015) 1259–1266.
[248] Giuseppe D'Aguanno, Curtis R. Menyuk, Nonlinear mode coupling in whispering-gallery-mode resonators, Phys. Rev. A 93 (4) (2016) 043820.
[249] P. Coullet, L. Gil, D. Repaux, Defects and subcritical bifurcations, Phys. Rev. Lett. 62 (25) (1989) 2957.
[250] Wim van Saarloos, Pierre C. Hohenberg, Fronts, pulses, sources and sinks in generalized complex Ginzburg-Landau equations, Phys. D 56 (4) (1992) 303–367.
[251] M.G. Clerc, D. Escaff, V.M. Kenkre, Patterns and localized structures in population dynamics, Phys. Rev. E 72 (5) (2005) 056217.
[252] Pedro Parra-Rivas, Edgar Knobloch, Damià Gomila, Lendert Gelens, Dark solitons in the Lugiato-Lefever equation with normal dispersion, Phys. Rev. A 93 (6) (2016) 063839.
[253] J. Knobloch, T. Wagenknecht, Homoclinic snaking near a heteroclinic cycle in reversible systems, Phys. D 206 (1–2) (2005) 82–93.
[254] Nikolay N. Rosanov, I transverse patternsin wide-aperture nonlinear optical systems, in: Progress in Optics, Vol. 35, Elsevier, 1996, pp. 1–60.
[255] P Parra-Rivas, Edgar Knobloch, Lendert Gelens, Damià Gomila, Origin, bifurcation structure and stability of localized states in Kerr dispersive optical cavities, IMA J. Appl. Math. 86 (5) (2021) 856–895.
[256] Graeme N Campbell, Lewis Hill, Pascal Del'Haye, Gian-Luca Oppo, Vectorial light in Fabry-Pérot resonators in the normal-dispersion regime, Phys. Rev. A 113 (4) (2026) 043505.
[257] M Bataille-Gonzalez, MG Clerc, B Kostet, Y Soupart, M Tlidi, Dissipative soliton combs with spectral filtering, Phys. Rev. A 112 (2) (2025) 023504.
[258] Xue Dong, Christopher Spiess, Victor G Bucklew, William H Renninger, Chirped-pulsed Kerr solitons in the Lugiato-Lefever equation with spectral filtering, Phys. Rev. Res. 3 (3) (2021) 033252.
[259] S-W Huang, H Zhou, J Yang, JF McMillan, A Matsko, M Yu, D-L Kwong, L Maleki, CW Wong, Mode-locked ultrashort pulse generation from on-chip normal dispersion microresonators, Phys. Rev. Lett. 114 (5) (2015) 053901.
[260] Alexander Pimenov, Andrei G. Vladimirov, Temporal solitons in an optically injected Kerr cavity with two spectral filters, Optics 3 (4) (2022) 364–383.
[261] Herbert B. Keller, Numerical solution of bifurcation and nonlinear eigenvalue problems, Appl. Bifurc. Theory (1977).
[262] W Liang, VS Ilchenko, AA Savchenkov, AB Matsko, D Seidel, L Maleki, Passively mode-locked Raman laser, Phys. Rev. Lett. 105 (14) (2010) 143903.

[263] Maxim Karpov, Hairun Guo, Arne Kordts, Victor Brasch, Martin HP Pfeiffer, Michail Zervas, Michael Geiselmann, Tobias J Kippenberg, Raman self-frequency shift of dissipative Kerr solitons in an optical microresonator, Phys. Rev. Lett. 116 (10) (2016) 103902.
[264] AV Cherenkov, NM Kondratiev, VE Lobanov, AE Shitikov, DV Skryabin, ML Gorodetsky, Raman-Kerr frequency combs in microresonators with normal dispersion, Opt. Express 25 (25) (2017) 31148–31158.
[265] Xianwen Liu, Changzheng Sun, Bing Xiong, Lai Wang, Jian Wang, Yanjun Han, Zhibiao Hao, Hongtao Li, Yi Luo, Jianchang Yan, et al., Integrated high-Q crystalline AlN microresonators for broadband Kerr and Raman frequency combs, ACS Photon. 5 (5) (2018) 1943–1950.
[266] Akitoshi Chen-Jinnai, Takumi Kato, Shun Fujii, Takuma Nagano, Tomoya Kobatake, Takasumi Tanabe, Broad bandwidth third-harmonic generation via four-wave mixing and stimulated Raman scattering in a microcavity, Opt. Express 24 (23) (2016) 26322–26331.
[267] Song Zhu, Lei Shi, Linhao Ren, Yanjing Zhao, Bo Jiang, Bowen Xiao, Xinliang Zhang, Controllable Kerr and Raman-Kerr frequency combs in functionalized microsphere resonators, Nanophotonics 8 (12) (2019) 2321–2329.
[268] M.G. Clerc, S. Coulibaly, P. Parra-Rivas, M. Tlidi, Nonlocal Raman response in Kerr resonators: Moving temporal localized structures and bifurcation structure, Chaos 30 (8) (2020).
[269] M.G. Clerc, S. Coulibaly, M. Tlidi, Time-delayed nonlocal response inducing traveling temporal localized structures, Phys. Rev. Res. 2 (1) (2020) 013024.
[270] P. Parra-Rivas, S. Coulibaly, M.G. Clerc, M. Tlidi, Influence of stimulated Raman scattering on Kerr domain walls and localized structures, Phys. Rev. A 103 (1) (2021) 013507.
[271] Shunyu Yao, Chengying Bao, Pan Wang, Changxi Yang, Generation of stable and breathing flat-top solitons via Raman assisted four wave mixing in microresonators, Phys. Rev. A 101 (2) (2020) 023833.
[272] Yunxiang Song, Zongda Li, Xinrui Zhu, Norman Lippok, Miro Erkintalo, Marko Lončar, High-efficiency and broadband Kerr comb generation in normal-dispersion x-cut lithium niobate microresonators, Sci. Adv. 12 (7) (2026) eaeb5758.
[273] H. Fujii, Mo Mimura, Y. Nishiura, A picture of the global bifurcation diagram in ecological interacting and diffusing systems, Phys. D 5 (1) (1982) 1–42.
[274] John Burke, Edgar Knobloch, Multipulse states in the Swift–Hohenberg equation, in: X. Hou, X. Lu, A. Miranville, J. Su, J. Zhu (Eds.), Dynamical Systems and Differential Equations, in: Discr. Contin. Dynam. Syst. Suppl, 2009, pp. 109–117.
[275] Mariana Haragus, Gérard Iooss, Local Bifurcations, Center Manifolds, and Normal Forms in Infinite-Dimensional Dynamical Systems, Springer Science & Business Media, 2010.
[276] Jürgen Knobloch, David JB Lloyd, Björn Sandstede, Thomas Wagenknecht, Isolas of 2-pulse solutions in homoclinic snaking scenarios, J. Dynam. Differential Equations 23 (1) (2011) 93–114.
[277] Elizabeth Makrides, Björn Sandstede, Predicting the bifurcation structure of localized snaking patterns, Phys. D 268 (2014) 59–78.
[278] Yasumasa Nishiura, Takeshi Watanabe, Traveling pulses with oscillatory tails, figure-eight-like stack of isolas, and dynamics in heterogeneous media, Phys. D 440 (2022) 133448.
[279] John Burke, S.M. Houghton, Edgar Knobloch, Swift-Hohenberg equation with broken reflection symmetry, Phys. Rev. E 80 (3) (2009) 036202.
[280] Pedro Parra-Rivas, Damià Gomila, François Leo, Stéphane Coen, Lendert Gelens, Third-order chromatic dispersion stabilizes Kerr frequency combs, Opt. Lett. 39 (10) (2014) 2971–2974.
[281] Alexander N Gorban, Nikolaos K Kazantzis, Ioannis G Kevrekidis, Hans Christian Öttinger, Constantinos Theodoropoulos, Model Reduction and Coarse-Graining Approaches for Multiscale Phenomena, Springer, 2006.
[282] Yanne K. Chembo, Ivan S. Grudinin, Nan Yu, Spatiotemporal dynamics of Kerr-Raman optical frequency combs, Phys. Rev. A 92 (4) (2015) 043818.
[283] Xu Yi, Qi-Fan Yang, Ki Youl Yang, Kerry Vahala, Theory and measurement of the soliton self-frequency shift and efficiency in optical microcavities, Opt. Lett. 41 (15) (2016) 3419–3422.
[284] Yadong Wang, Miles Anderson, Stéphane Coen, Stuart G Murdoch, Miro Erkintalo, Stimulated Raman scattering imposes fundamental limits to the duration and bandwidth of temporal cavity solitons, Phys. Rev. Lett. 120 (5) (2018) 053902.
[285] Wei Chen, Bruno Garbin, Alexander U Nielsen, Stéphane Coen, Stuart G Murdoch, Miro Erkintalo, Experimental observations of breathing Kerr temporal cavity solitons at large detunings, Opt. Lett. 43 (15) (2018) 3674–3677.
[286] Guoping Lin, Qinghai Song, Kerr frequency comb interaction with Raman, Brillouin, and second order nonlinear effects, Laser Photon. Rev. 16 (1) (2022) 2100184.
[287] Gwangho Choi, Judith Su, Impact of stimulated Raman scattering on dark soliton generation in a silica microresonator, J. Phys.: Photon. 5 (1) (2023) 014001.
[288] Zongda Li, Yiqing Xu, Sophie Shamailov, Xiaoxiao Wen, Wenlong Wang, Xiaoming Wei, Zhongmin Yang, Stéphane Coen, Stuart G Murdoch, Miro Erkintalo, Ultrashort dissipative Raman solitons in Kerr resonators driven with phase-coherent optical pulses, Nat. Photon. 18 (1) (2024) 46–53.
[289] Keith J. Blow, David Wood, Theoretical description of transient stimulated Raman scattering in optical fibers, IEEE J. Quantum Electron. 25 (12) (1989) 2665–2673.
[290] Q. Lin, Govind P. Agrawal, Raman response function for silica fibers, Opt. Lett. 31 (21) (2006) 3086–3088.
[291] M Tlidi, L Bahloul, L Cherbi, A Hariz, Saliya Coulibaly, Drift of dark cavity solitons in a photonic-crystal fiber resonator, Phys. Rev. A—At. Mol. Opt. Phys. 88 (3) (2013) 035802.
[292] A Hariz, L Bahloul, L Cherbi, K Panajotov, Marcel Clerc, MA Ferré, B Kostet, E Averlant, M Tlidi, Swift-Hohenberg equation with third-order dispersion for optical fiber resonators, Phys. Rev. A 100 (2) (2019) 023816.
[293] Eusebius Doedel, Herbert B. Keller, Jean Pierre Kernevez, Numerical analysis and control of bifurcation problems (I): Bifurcation in finite dimensions, Int. J. Bifurc. Chaos 1 (03) (1991) 493–520.
[294] Eusebius Doedel, Herbert B. Keller, Jean Pierre Kernevez, Numerical analysis and control of bifurcation problems (II): Bifurcation in infinite dimensions, Int. J. Bifurc. Chaos 1 (04) (1991) 745–772.
[295] Arik Yochelis, John Burke, Edgar Knobloch, Reciprocal oscillons and nonmonotonic fronts in forced nonequilibrium systems, Phys. Rev. Lett. 97 (25) (2006) 254501.
[296] A.C. Newell, Y. Pomeau, Turbulent crystals in macroscopic systems, J. Phys. A: Math. Gen. 26 (8) (1993) L429–L434.
[297] M Le Berre, E Ressayre, A Tallet, Y Pomeau, L Di Menza, Example of a chaotic crystal: The labyrinth, Phys. Rev. E 66 (2) (2002) 026203.
[298] S. Echeverría-Alar, M.G. Clerc, Labyrinthine patterns transitions, Phys. Rev. Res. 2 (4) (2020) 042036.
[299] Paul Manneville, Dissipative structures and weak turbulence, in: Chaos—the Interplay Between Stochastic and Deterministic Behaviour: Proceedings of the XXXIst Winter School of Theoretical Physics Held in Karpacz, Poland 13–24 February 1995, Springer, 2005, pp. 257–272.
[300] Andrei Nikolaevich Kolmogorov, Turbulence: The Legacy of AN Kolmogorov, Cambridge University Press, 1995.
[301] Arkady Pikovsky, Antonio Politi, Lyapunov Exponents: A Tool to Explore Complex Dynamics, Cambridge University Press, 2016.
[302] Steven H. Strogatz, Nonlinear Dynamics and Chaos: with Applications to Physics, Biology, Chemistry, and Engineering, Chapman and Hall/CRC, 2024.
[303] Stefanos Boccaletti, Celso Grebogi, Y-C Lai, Hector Mancini, Diego Maza, The control of chaos: theory and applications, Phys. Rep. 329 (3) (2000) 103–197.

[304] Stefano Boccaletti, Vito Latora, Yamir Moreno, Martin Chavez, D-U Hwang, Complex networks: Structure and dynamics, Phys. Rep. 424 (4–5) (2006) 175–308.
[305] J.P. Gollub, A.R. McCarriar, J.F. Steinman, Convective pattern evolution and secondary instabilities, J. Fluid Mech. 125 (1982) 259–281.
[306] Marcel Lesieur, Turbulence in Fluids: Stochastic and Numerical Modelling, vol. 488, Nijhoff Boston, MA, 1987.
[307] J.M. Schmitt, G. Kumar, Turbulent nature of refractive-index variations in biological tissue, Opt. Lett. 21 (16) (1996) 1310–1312.
[308] Hideharu Sasaki, Patrice Klein, Bo Qiu, Yoshikazu Sasai, Impact of oceanic-scale interactions on the seasonal modulation of ocean dynamics by the atmosphere, Nat. Commun. 5 (1) (2014) 5636.
[309] Jörn Callies, Raffaele Ferrari, Jody M Klymak, Jonathan Gula, Seasonality in submesoscale turbulence, Nat. Commun. 6 (1) (2015) 6862.
[310] EG Turitsyna, SV Smirnov, S Sugavanam, N Tarasov, X Shu, SA Babin, EV Podivilov, DV Churkin, Gregory Falkovich, SK Turitsyn, The laminar–turbulent transition in a fibre laser, Nat. Photon. 7 (10) (2013) 783–786.
[311] Stefan Wabnitz, Optical turbulence in fiber lasers, Opt. Lett. 39 (6) (2014) 1362–1365.
[312] Ivan R Roa Gonzalez, Bismarck C Lima, Pablo IR Pincheira, Arthur A Brum, Antônio MS Macêdo, Giovani L Vasconcelos, Leonardo de S. Menezes, Ernesto P Raposo, Anderson SL Gomes, Raman Kashyap, Turbulence hierarchy in a random fibre laser, Nat. Commun. 8 (1) (2017) 15731.
[313] G Xu, D Vocke, D Faccio, J Garnier, T. Roger, S. Trillo, A Picozzi, From coherent shocklets to giant collective incoherent shock waves in nonlocal turbulent flows, Nat. Commun. 6 (1) (2015) 8131.
[314] PJ Aguilera-Rojas, MG Clerc, S Echeverria-Alar, Y Soupart, M Tlidi, Fingerprint pattern bi-turbulence in a driven dissipative optical system, Chaos Solitons Fractals 182 (2024) 114851.
[315] Berta Martínez-Prat, Ricard Alert, Fanlong Meng, Jordi Ignés-Mullol, Jean-François Joanny, Jaume Casademunt, Ramin Golestanian, Francesc Sagués, Scaling regimes of active turbulence with external dissipation, Phys. Rev. X 11 (3) (2021) 031065.
[316] Ricard Alert, Jaume Casademunt, Jean-François Joanny, Active turbulence, Annu. Rev. Condens. Matter Phys. 13 (1) (2022) 143–170.
[317] Qi Ouyang, Harry L. Swinney, Transition to chemical turbulence, Chaos 1 (4) (1991) 411–420.
[318] Emanuel Alves de Lima Henn, Jorge Amin Seman, Giacomo Roati, Kilvia Mayre Farias Magalhaes, Vanderlei Salvador Bagnato, Emergence of turbulence in an oscillating Bose-Einstein condensate, Phys. Rev. Lett. 103 (4) (2009) 045301.
[319] M.G. Clerc, M.A. Ferré, S. Coulibaly, R.G. Rojas, Mustapha Tlidi, Chimera-like states in an array of coupled-waveguide resonators, Opt. Lett. 42 (15) (2017) 2906–2909.
[320] Marcel Gabriel Clerc, Saliya Coulibaly, M.A. Ferré, Mustapha Tlidi, Two-dimensional optical chimera states in an array of coupled waveguide resonators, Chaos 30 (4) (2020).
[321] Faraz Monifi, Jing Zhang, Şahin Kaya Özdemir, Bo Peng, Yu-xi Liu, Fang Bo, Franco Nori, Lan Yang, Optomechanically induced stochastic resonance and chaos transfer between optical fields, Nat. Photon. 10 (6) (2016) 399–405.
[322] Miles Anderson, François Leo, Stéphane Coen, Miro Erkintalo, Stuart G Murdoch, Observations of spatiotemporal instabilities of temporal cavity solitons, Optica 3 (10) (2016) 1071–1074.
[323] François Leo, Lendert Gelens, Philippe Emplit, Marc Haelterman, Stéphane Coen, Dynamics of one-dimensional Kerr cavity solitons, Opt. Express 21 (7) (2013) 9180–9191.
[324] Ze Wang, Kaixuan Zhu, Fangxing Zhang, Qihuang Gong, Qi-Fan Yang, Collision-induced rogue waves and universal transport dynamics in chaotic Kerr microresonators, Sci. Adv. 11 (21) (2025) eadv9422.
[325] David Ruelle, Large volume limit of the distribution of characteristic exponents in turbulence, Comm. Math. Phys. 87 (2) (1982) 287–302.
[326] Edward Ott, Chaos in Dynamical Systems, Cambridge University Press, 2002.